Chemical Science

ROYAL SOCIETY OF CHEMISTRY

PERSPECTIVE

View Article Online
View Journal | View Issue

Cite this: *Chem. Sci.*, 2025, **16**, 21174

All publication charges for this article have been paid for by the Royal Society of Chemistry

Chemical probes for enzyme imaging: challenges in design, synthesis and biomedical applications

Julia Nguyen, †[a] Maksymilian Zabijak †[a] and Marcin Poręba *[ab]

Enzymes play central roles in cellular regulation, disease progression, and therapeutic response, making them ideal targets for diagnostic and therapeutic chemical probes. Among them, proteases and kinases are particularly valuable due to their dysregulation in cancer, immune disorders, and infectious diseases. In this Perspective, we highlight recent advances in chemical probe development aimed at these enzyme families, with a focus on imaging modalities and translational potential. Kinase-targeted probes are frequently derived from clinically approved inhibitors, facilitating their repurposing for diagnostic applications. In contrast, protease-responsive probes rely on detailed substrate specificity profiling, where the incorporation of unnatural amino acids serves as a key strategy for achieving selectivity and stability in biological systems. We explore the broad landscape of probe modalities, including activatable fluorescent substrates, PET tracers, and mass cytometry-compatible metal-tagged reagents, that collectively enable sensitive, real-time, and multiplexed analysis of enzyme function in cells and tissues. Notably, enzyme-activated theranostic systems are emerging that couple imaging with targeted drug release, expanding the functional scope of chemical probes beyond detection. We also discuss how artificial intelligence is beginning to support the design process, from structure prediction and binding affinity modeling to the generation of novel chemical scaffolds with favorable pharmacological properties. With several enzyme-targeted probes now in clinical trials or approved for human use, this field exemplifies the success of translational chemical biology and the potential of chemical tools to directly impact patient care.

Received 29th July 2025
Accepted 29th October 2025

DOI: 10.1039/d5sc05683g

rsc.li/chemical-science

1. Introduction

Enzymes are fundamental regulators of nearly every biological process, and their activity often reflects dynamic physiological or pathological states more accurately than their abundance.[1] Among them, proteases and kinases stand out as particularly important in biomedicine. Proteases, through their roles in tissue remodeling, inflammation, apoptosis, and metastasis, are deeply implicated in cancer, cardiovascular disease, and immune disorders.[2,3] Likewise, kinases orchestrate complex signal transduction cascades governing cell growth, differentiation, and survival, with dysregulated kinase activity being a hallmark of many malignancies and inflammatory diseases.[4,5] Beyond these, other enzyme classes, including glycosidases, phosphatases, and oxidoreductases, are increasingly recognized as critical players in metabolism, infection, neurodegeneration, and immune modulation.[1] As such, enzymes serve not only as biomarkers of disease but also as direct therapeutic targets.[6,7] The ability to image their activity in living systems provides a window into biochemical processes with unparalleled specificity and spatiotemporal resolution, with vast implications for early diagnosis, disease monitoring, and precision medicine.[8]

Historically, the study of enzyme function relied on *in vitro* methods such as spectrophotometric assays, zymography, or immunoblotting, which are powerful but fundamentally limited to fixed or lysed samples.[9–11] These approaches lack the capacity to capture enzyme activity in its native context, that is, within intact, dynamic biological systems. In contrast, the development of chemical probes designed for enzyme imaging has enabled a transformative shift from static to dynamic analyses, allowing real-time visualization of enzyme activity within living organisms.[12–15] This evolution has been driven by advances in organic synthesis, imaging technology, and a deeper understanding of enzyme–substrate interactions. Modern enzyme-targeted chemical probes are typically composed of three elements: (i) a targeting moiety (such as a substrate or inhibitor), (ii) a linker, and (iii) a reporter group that produces a measurable signal upon enzymatic interaction. When administered systemically, these probes circulate through the body and become activated or accumulate at sites where the target enzyme is functionally active.[8,16] The resulting signal, whether optical, radioactive, magnetic, or elemental, can then

[a]*Faculty of Chemistry, Wroclaw University of Science and Technology, Wyb. Wyspianskiego 27, 50-370, Wroclaw, Poland. E-mail: marcin.poreba@pwr.edu.pl*

[b]*Faculty of Medicine, Wroclaw University of Science and Technology, Wyb. Wyspianskiego 27, 50-370, Wroclaw, Poland*

† These authors contributed equally.

be detected by an appropriate imaging modality. Critically, such probes enable activity-based rather than abundance-based imaging, thus distinguishing between active and inactive enzyme populations. This is particularly relevant in disease settings where overexpression of an enzyme does not necessarily correlate with catalytic function. Fluorescence imaging remains the most widely used modality for enzyme probe development, favored for its high sensitivity, versatility, and real-time readouts. Many probes utilize a "turn-on" mechanism, wherein fluorescence is quenched until enzymatic cleavage of a substrate releases the active fluorophore.[17] The introduction of near-infrared (NIR) and NIR-II fluorophores has further enhanced *in vivo* applicability by improving tissue penetration and reducing background autofluorescence.[18] Meanwhile, positron emission tomography (PET) and single-photon emission computed tomography (SPECT) allow highly sensitive, quantitative imaging of radiolabeled enzyme probes at the whole-body level.[19] These modalities are particularly useful for longitudinal studies and clinical translation but impose strict requirements on probe stability and radiochemical synthesis. Magnetic resonance imaging (MRI) offers superior anatomical resolution and is increasingly employed using enzyme-activated contrast agents that alter relaxivity upon cleavage or binding.[20,21] More recently, mass cytometry techniques, such as cytometry by time-of-flight (CyTOF) and imaging mass cytometry (IMC), have opened the door to highly multiplexed, *ex vivo* analysis of enzyme activity.[22,23] Here, lanthanide-tagged probes can simultaneously profile dozens of enzymes or biomarkers in single cells or tissue sections, without spectral overlap.

The design of enzyme-targeted probes typically follows one of three general strategies. Substrate-based probes incorporate a recognition sequence that undergoes enzymatic transformation, such as cleavage (*e.g.*, hydrolases), modification (*e.g.*, oxidoreductases), or group transfer (*e.g.*, protein kinases, glycosyltransferases), leading to signal generation. These are conceptually simple and often amplify signal, since one enzyme can process multiple probe molecules.[24] Inhibitor-based probes, by contrast, contain reactive groups that covalently and irreversibly bind to the active site of the enzyme. This allows a direct and stoichiometric readout of catalytic function, particularly useful for profiling proteases and kinases in complex biological environments.[10] A third strategy employs affinity-based probes, often derived from known inhibitors, that bind non-covalently or *via* photo-crosslinking. These are especially valuable for kinases, where binding selectivity can be finely tuned, and for target engagement studies.[25] Despite rapid progress, the field faces persistent challenges. One of the most formidable is achieving high selectivity for individual enzyme isoforms, particularly within large and conserved families such as caspases or tyrosine kinases.[26,27] Minor variations in active site topology or substrate preference can be difficult to exploit without extensive synthetic optimization. Furthermore, enzyme-targeted probes must demonstrate sufficient stability in biological fluids, resist off-target activation, and exhibit favorable pharmacokinetics to accumulate selectively at the site of interest.[8,28] The design of the reporter group must also be compatible with the chosen imaging modality: for example, PET probes require isotopes such as ^{18}F or ^{64}Cu that necessitate short synthetic timelines and specialized facilities, while MRI probes often require multimeric assemblies or enzymatically triggered self-assembly to generate adequate contrast.[29] Additionally, probe synthesis must be scalable and robust, especially for applications in preclinical or clinical settings. For complex probes, such as those incorporating peptides, fluorophores, and radiolabels, multi-step synthesis, purification, and functional testing pose logistical barriers to widespread use. Another emerging frontier lies in minimizing background signal from non-specific activation or accumulation. This issue is especially pertinent for *in vivo* optical imaging, where autofluorescence and probe diffusion can obscure true enzymatic activity. Similarly, non-enzymatic degradation of probes in circulation can release the signal prematurely, reducing contrast and limiting diagnostic value.[30]

1.1. What makes a good probe for *in vivo* imaging

For *in vivo* imaging applications, the selectivity of protease chemical probes is paramount. A major challenge lies in ensuring that the probe resists cleavage by off-target enzymes with similar substrate specificities. Lack of selectivity remains a significant limitation, as many probes are activated by proteases expressed in both pathological and healthy tissues. This non-specific activation reduces imaging contrast and diminishes diagnostic precision, particularly in applications such as.[8,31] One of the defining weaknesses of poorly designed fluorescent probes, especially conventional "always-on" variants, is their inability to provide sufficient contrast between malignant and normal tissues. These probes emit continuous fluorescence regardless of their biological environment, resulting in low tumor-to-background ratios and impeding accurate delineation of tumor margins. This problem is exacerbated by tissue autofluorescence, nonspecific accumulation, and light scattering, all of which lower the signal-to-noise ratio and hinder the detection of small or early-stage lesions.[31,32] Traditional imaging modalities such as MRI, CT, and ultrasound often lack the spatial resolution necessary to detect microscopic cancerous deposits, particularly those under 5 mm in size. Given that many metastatic lesions are smaller than 2–3 mm, an effective imaging probe must offer not only high specificity, but also exceptional sensitivity.[33] It should generate a robust signal in response to pathological enzyme activity, while remaining silent in the presence of physiological background levels. This is especially important for enzymes that are upregulated in tumors but still present at low levels in healthy tissues.[16,34] Without this level of discrimination, there is a risk of false-positive signals and unnecessary tissue excision. In the context of surgical imaging, the speed of probe activation is also critical. The probe should generate a detectable signal within minutes, to align with the surgical workflow and provide real-time feedback to the operating team. Many existing probes require prolonged incubation to reach peak fluorescence, which limits their usefulness in intraoperative settings.[8,35] Beyond selectivity and activation kinetics, other essential properties of a good *in vivo* probe include stability in circulation, minimal

toxicity, and favorable pharmacokinetics to ensure efficient delivery to the tumor site. Optical properties also matter: the fluorophore should ideally emit in the near-infrared range to minimize background interference, reduce photobleaching, and allow deeper tissue penetration.[35] Furthermore, the probe should be designed to avoid nonspecific uptake by the reticuloendothelial system and ensure rapid clearance from non-target tissues. In summary, an ideal *in vivo* protease probe must combine high target selectivity, fast and specific activation, robust optical contrast, and suitable pharmacological behavior to function effectively in the complex physiological environment of a living organism. These combined features are essential for clinical translation, particularly in applications such as early diagnosis, real-time tumor margin visualization, and intraoperative decision-making.

Against this backdrop, the present Perspective aims to provide a comprehensive yet critical overview of recent advances in the design, synthesis, and application of enzyme-targeted chemical probes for imaging. Particular emphasis is placed on proteases and kinases, not only due to their established medical relevance but also because they exemplify the chemical and biological challenges associated with probe development. We also highlight recent progress in imaging probes for other enzyme classes, including glycosidases and phosphatases, which are rapidly gaining recognition as valuable diagnostic targets. Across diverse imaging modalities, ranging from fluorescence and PET to mass cytometry, we examine how probe structure, stability, and functional performance determine imaging efficacy. Finally, we explore how artificial intelligence and modular chemistry are poised to accelerate probe discovery and translation. By integrating examples from chemical biology, medicinal chemistry, and biomedical imaging, we aim to illuminate the evolving landscape of enzyme imaging and define key priorities for future innovation.

2. Fluorescent probes for proteases

2.1. The general structure of protease chemical probes

Proteases are enzymes that catalyze the hydrolysis of peptide bonds.[36] Accordingly, chemical probes designed to monitor their activity typically consist of at least two fundamental components: a peptide recognition sequence selective for a specific protease, and a reporter tag that enables detection of enzymatic activity.[14,37] Protease-targeted probes can be broadly categorized into two classes: inhibitor-based probes, commonly referred to as activity-based probes (ABPs), and substrate-based probes (SBPs). Although 'ABP' is often used for inhibitor-based probes, both inhibitor- and substrate-based probes detect enzymes in their catalytically active state (Fig. 1). ABPs covalently bind to the enzyme's active site *via* an electrophilic warhead, such as an (acyloxy)methyl ketone (AOMK), a phosphonate group [typically $-O^{P}(OPh)_2$], or a vinyl sulfone (VS), which are commonly used for targeting cysteine, serine, and threonine proteases, respectively.[14] In most cases, these probes contain a constitutively active ("always-on") reporter tag, although quenched activity-based probes (qABPs) and environment-sensitive probes have also been developed.[38,39] The latter include quenching moieties that suppress the fluorescence of the tag until the probe reacts with the enzyme, thereby reducing background signal. Due to their covalent and irreversible mode of action, ABPs are particularly well-suited for applications such as western blot analysis and fluorescence microscopy, where stable labeling is required. In contrast, SBPs are non-covalent and rely on enzymatic cleavage of a specific peptide sequence to activate a signal, typically through the release or unquenching of a fluorophore.[39,40] Because the fluorescent signal is generated only upon proteolytic cleavage, SBPs generally offer a higher signal-to-noise ratio, which is advantageous for dynamic, live-cell applications. Techniques such as fluorescence microscopy and flow cytometry are commonly used to visualize enzymatic activity with SBPs. While ABPs provide stronger target retention and increased intracellular stability, their stoichiometric (1 : 1) interaction with the enzyme limits the potential for signal amplification. In contrast, SBPs allow multiple turnover events by a single protease molecule, enabling amplification of the signal.[24] Reporter tags used in protease probes are most commonly fluorophores, although metal-based reporters, such as those used in PET imaging or time-of-flight (TOF) mass cytometry, are also employed in specialized applications.[41,42] Fluorescence activation can be achieved through various mechanisms, including the restoration of functional groups, the disruption of Förster resonance energy transfer (FRET), charge transfer (CT), or photoinduced electron transfer (PET) in quenched probes, as well as aggregation-induced emission (AIE) and bioorthogonal *in situ* fluorophore synthesis.[24] Since metal-tagged probes for mass cytometry (so called TOF-probes) are discussed in a separate chapter, the focus here will be on selected examples of fluorogenic, peptide-based protease probes. Given the highly active and competitive nature of research in this area, only a subset of probes with demonstrated or promising relevance for clinical applications is presented, with particular emphasis on selectivity and translational potential.

2.2. Protease chemical probes for biomedical applications

The clinical success of protease-targeted imaging agents hinges on their ability to combine biochemical selectivity with functional performance in complex biological environments. One of such example was provided by Liu *et al.* who developed **Bio-DEVD-HCy**, a dual-modal fluorescent and photoacoustic imaging probe for detecting caspase-3 activity during tumor apoptosis (Fig. 2A).[43] The probe integrates three functional units: a biotin targeting group for tumor-specific accumulation, a DEVD peptide sequence as a caspase-3 recognition site, and a hemicyanine (HCy) dye as the NIR reporter. In its intact state, the probe's fluorescence and photoacoustic signals are quenched due to inhibited intramolecular charge transfer (ICT). Upon caspase-3 cleavage at the DEVD site, the dye is released, restoring ICT and producing strong NIR fluorescence and photoacoustic responses. The biotin modification enhances selective tumor uptake through receptor-mediated targeting, as confirmed by competition experiments with free biotin. In cellular studies, **Bio-DEVD-HCy** showed significant signal

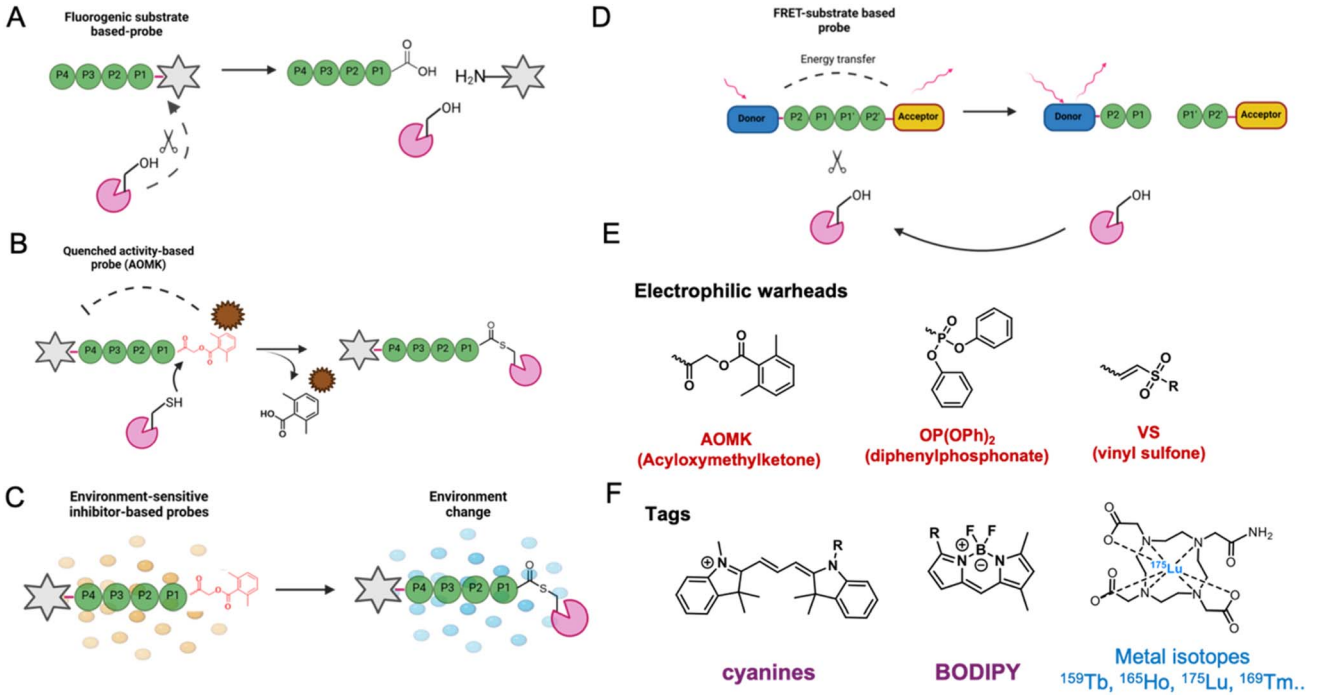

Fig. 1 Chemical probes for proteases. (A) Fluorogenic substrate based probe. (B) Quenched activity-based probe. (C) Environment-sensitive inhibitor-based probe. (D) FRET-based substrate probe. (E and F) Examples of probe elements – electrophilic warheads (E) and detection tags (F).

increases in doxorubicin-treated apoptotic 4T1 breast cancer cells, outperforming a non-targeted control probe. *In vivo* imaging in tumor-bearing mice demonstrated clear visualization of apoptosis, with 2.5-fold fluorescence and 4.1-fold photoacoustic enhancement in treated tumors. The probe displayed favorable pharmacokinetics and an optimal imaging

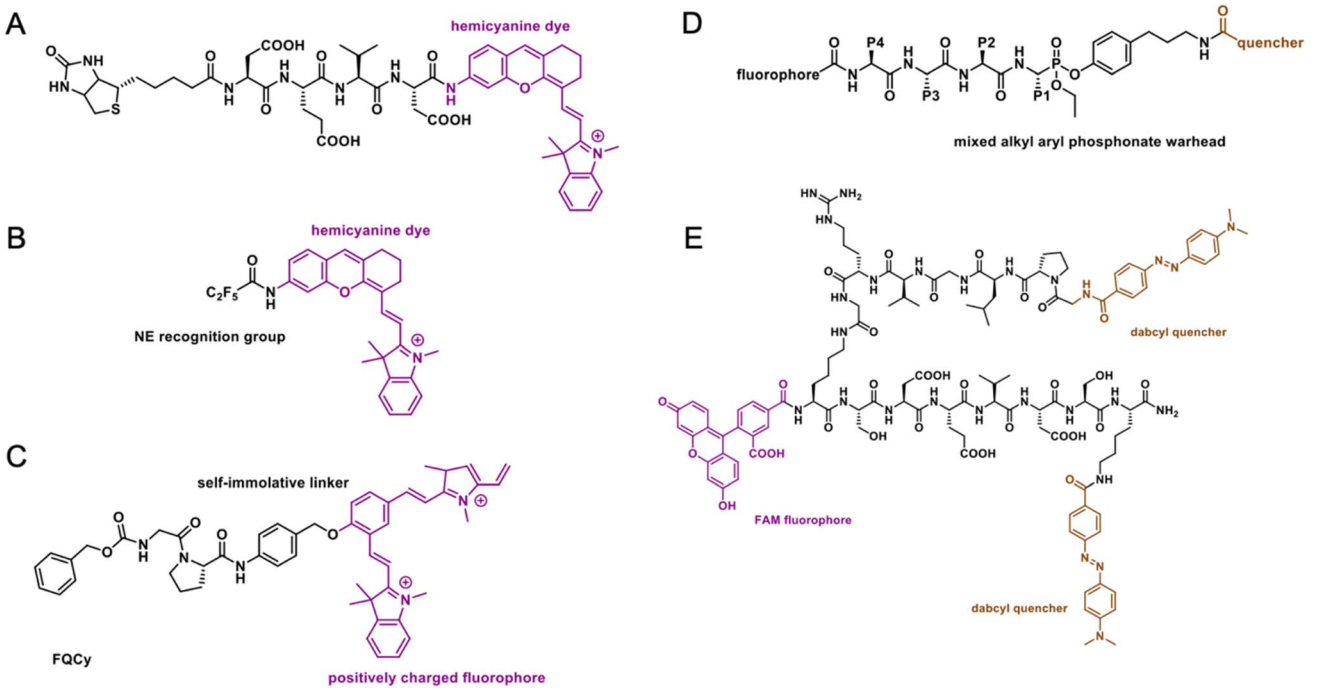

Fig. 2 The structure of selected activity-based probes. (A) **Bio-DEVD-HCy**, a dual-modal fluorescent for detecting caspase-3 activity. (B) **NEP** hemicyanine-based probe for imaging of neutrophil elastase (NE). (C) FQCy7 – a dicationic cyanine-based probe for fibroblast activation protein α (FAPα) (D) **BODIPY-BHQ-1** alkyl aryl phosphonate probe. (E) FAM-K(GRVGLPG-Dabcyl)SDEVDSK(Dabcyl), a dual-FRET-based fluorescence probe for MMP-2 and caspase-3.

window around four hours post-injection. Its NIR optical properties enable deep-tissue imaging with reduced scattering and absorption, making it suitable for noninvasive monitoring of therapeutic efficacy. Overall, **Bio-DEVD-HCy** represents a promising platform for targeted, enzyme-responsive molecular imaging in cancer diagnosis and therapy assessment.

Recently, Yang *et al.* developed **NEP**, a hemicyanine-based chemical probe, and its nanoformulated counterpart **NanoNEP** for multimodal imaging of neutrophil elastase (NE) activity in diabetic complications (Fig. 2B).[44] The core probe design employs a pentafluoropropanoic acid-protected amino group that suppresses intramolecular charge transfer until enzymatic cleavage by NE restores near-infrared fluorescence and photoacoustic signals. This activation mechanism allows **NEP** to report NE activity through triple-modality readouts, including fluorescence, photoacoustic, and absorption spectroscopy, offering both high sensitivity and spatial resolution. To overcome the probe's poor solubility, the researchers engineered **NanoNEP** by self-assembling **NEP** with bovine serum albumin, forming biocompatible nanoparticles with enhanced aqueous stability and preserved optical performance. **NanoNEP** demonstrated low detection limits for both fluorescence and photoacoustic modes, along with strong linear correlations with NE concentration, high selectivity, and excellent stability under physiological conditions. In a streptozotocin-induced diabetic mouse model, **NanoNEP** successfully visualized elevated NE activity in liver tissue, wounds, and serum, correlating with inflammatory damage and poor wound healing. Treatment with metformin partially reduced NE-associated signals, highlighting the probe's capability to monitor therapeutic efficacy and reveal NE's contribution to diabetic inflammation. Human validation studies confirmed increased fluorescence in diabetic foot lesions and patient serum, demonstrating the translational potential of **NanoNEP** for clinical diagnostics. Cytotoxicity and histopathological analyses indicated excellent biocompatibility, with the albumin nanoformulation markedly reducing toxicity compared to free **NEP**. Collectively, this study establishes **NanoNEP** as a powerful and clinically viable imaging platform for detecting and quantifying neutrophil elastase activity, enabling noninvasive monitoring of inflammation and therapeutic response in diabetic complications.

Feng *et al.* introduced a charge-based strategy for designing highly sensitive fluorescent probes targeting fibroblast activation protein α (FAPα), a key biomarker associated with tumor invasion and metastasis (Fig. 2C).[45] Unlike conventional FAPα probes that rely solely on modifying recognition sequences, this approach enhances probe–enzyme interactions by introducing positive charges into the fluorophore skeleton, exploiting electrostatic complementarity with FAPα′s negatively charged catalytic pocket. Through systematic structural optimization, the researchers developed a library of probes and identified **FQCy7**, a dicationic cyanine-based probe, as the lead candidate due to its superior optical and enzymatic performance. The probe operates through a caged amino group mechanism in which the Cbz-Gly-Pro substrate blocks intramolecular charge transfer until enzymatic cleavage by FAPα restores strong near-infrared fluorescence. The introduction of positive charges significantly improved enzyme binding affinity, catalytic efficiency, and detection sensitivity. Comparative studies and molecular docking confirmed that charged variants displayed stronger binding and faster activation kinetics than their neutral counterparts. In cellular imaging, **FQCy7** successfully differentiated highly invasive MDA-MB-231 breast cancer cells from less invasive MCF-7 cells and tracked FAPα activity modulation following inhibitor or drug treatment. In clinical tissue analyses, the probe clearly distinguished invasive carcinomas from benign lesions and revealed residual tumor regions in surgical margins, correlating with histopathology and FAPα immunofluorescence. Animal model studies demonstrated its capability for real-time intraoperative guidance, enabling precise tumor resection and assessment of surgical completeness. Overall, **FQCy7** exemplifies a powerful new design paradigm in enzyme-responsive imaging, establishing a versatile and clinically translatable platform for sensitive cancer detection, image-guided surgery, and therapeutic monitoring.

In 2025, Kahler *et al.* introduced the first quenched activity-based probes for real-time imaging of neutrophil serine proteases (NSPs), representing an advance in activity-based probe design for this family of proteases (Fig. 2D).[46] The researchers developed a series of mixed alkyl aryl phosphonate probes that combine selective peptide recognition sequences, electrophilic warheads, and fluorophore-quencher pairs to achieve enzyme-activated fluorescence. These mixed phosphonate electrophiles, unlike traditional diphenyl phosphonates, create a chiral phosphorus center that allows efficient quencher release upon covalent reaction with active serine proteases. The probes remain non-fluorescent in their quenched state but produce a strong fluorescence signal upon enzyme-mediated cleavage, enabling visualization of protease activity with high spatial and temporal precision. Among the designs tested, **BODIPY-BHQ-1** probe variants exhibited over 400-fold quenching efficiency and superior activation kinetics. Biochemical assays confirmed high selectivity for neutrophil elastase, proteinase 3, and cathepsin G, with minimal cross-reactivity or off-target labeling in complex proteomes. In cellular studies, the probes enabled live imaging of NETosis, showing time-dependent increases in fluorescence that correlated with neutrophil activation and release of granule-stored proteases. Their membrane-impermeable nature proved advantageous, ensuring selective detection of extracellular protease activity associated with cellular rupture during immune responses. Confocal microscopy validated probe colocalization with neutrophil elastase and confirmed activity-dependent labeling inhibited by known NSP inhibitors. Overall, these phosphonate-based qABPs provide a powerful and selective platform for real-time imaging of serine protease activity in living cells, with broad potential applications in studying inflammation, immune responses, and the development of anti-inflammatory therapeutics.

Dual-locked fluorescent probes are advanced molecular imaging tools that require two distinct biomarkers to activate, greatly improving specificity and minimizing false-positive signals. By integrating multiple recognition elements into a single construct, they enable precise and reliable visualization

of complex biological processes such as inflammation, apoptosis, and immune activation; reviewed in ref. 47. Hu *et al.* reported the design of **DMRP$_{NOCas}$**, a dual-locked near-infrared fluorescent probe that enables precise monitoring of M1 macrophage polarization in pulmonary inflammation (Fig. 3).[48] The probe is engineered to require simultaneous activation by two biomarkers: caspase-1 and nitric oxide (NO)-both of which are highly expressed in pro-inflammatory M1 macrophages, ensuring exceptional specificity. Structurally, **DMRP$_{NOCas}$** is built on a hemicyanine scaffold modified with an *o*-phenylenediamine group as the NO-reactive site and an Ac-YVAD peptide sequence as the caspase-1-cleavable domain, while a hydroxypropyl-β-cyclodextrin unit facilitates renal clearance for noninvasive urinalysis. The probe's dual-lock mechanism operates through a twisted intramolecular charge transfer (TICT) process, in which sequential NO reaction and caspase-1 cleavage "unlock" strong fluorescencE. Quantum chemical analysis revealed that *para*-substitution on the *o*-phenylenediamine group increased the TICT rotational barrier and enhanced signal output, resulting in a 9-fold fluorescence increase upon full activation. In cellular assays, **DMRP$_{NOCas}$** exhibited 12-fold higher fluorescence in M1 macrophages than in M2 or other immune cell types, outperforming single-locked control probes. In an influenza A virus infection mouse model, the probe successfully visualized macrophage dynamics in the lungs, showing peak fluorescence 48 hours post-infection and detectable urinary signals due to renal clearance. Treatment with the antiviral oseltamivir reduced both lung and urine fluorescence, demonstrating the probe's utility for therapeutic response monitoring. Flow cytometry and immunofluorescence confirmed that probe activation correlated with monocyte-derived M1 macrophages, providing mechanistic insights into inflammatory responses. Overall, **DMRP$_{NOCas}$** represents a major advance in dual-responsive molecular probe design, offering a clinically translatable, noninvasive platform for real-time monitoring of pulmonary immune activity and inflammation.

Another illustrative example is **YH-APN**, an enzyme-activatable fluorescent probe developed by Li *et al.* for imaging aminopeptidase N (APN/CD13) activity in tumors.[49] Designed for intraoperative fluorescence-guided surgery, the probe combines a recognition motif based on L-alanine with a dicyanoisophorone fluorophore that emits in the near-infrared region, ensuring deep tissue penetration and reduced background autofluorescence. Upon APN-mediated cleavage, the probe undergoes a structural change in its π-electron system, resulting in a sharp fluorescence turn-on without the need for external quenchers (Fig. 4). **YH-APN** exhibits excellent aqueous solubility (up to 100 μM), a large Stokes shift (205 nm), and is optimized for physiological conditions (37 °C, pH 7.4). These features translate into high imaging contrast and minimal self-quenching. The probe successfully distinguished APN-overexpressing cancer cells from non-cancerous cells in co-culture assays and produced strong tumor-to-normal tissue

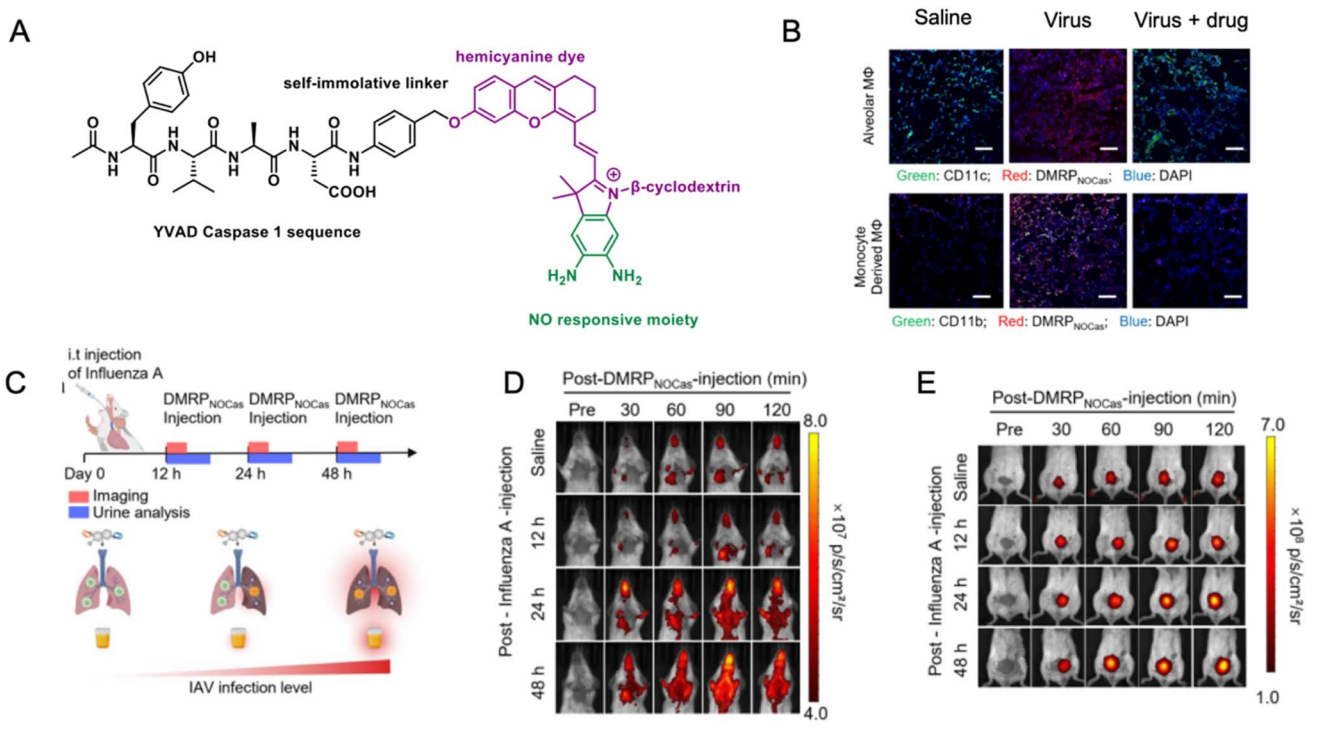

Fig. 3 An example of dual-locked fluorescent probe responsive to caspase-1 and nitric oxide. (A) The structure of DMRP$_{NOCas}$. (B) Representative confocal fluorescence microscopy images of M1 macrophage in lung slices from mice with different IAV infection times. Green: iNOS; red: caspase-1; blue: DAPI. (C) Real-time imaging of M1 macrophage polarization in IAV-infected mice. Schematic illustration of IAV infection and real-time imaging of the M1 macrophage. (D) Real-time imaging of mice breast; and (E) bladder with different treatments after intravenous injection of DMRP$_{NOCas}$. Adapted with permission from ref. 48 Copyright 2025, American Chemical Society.

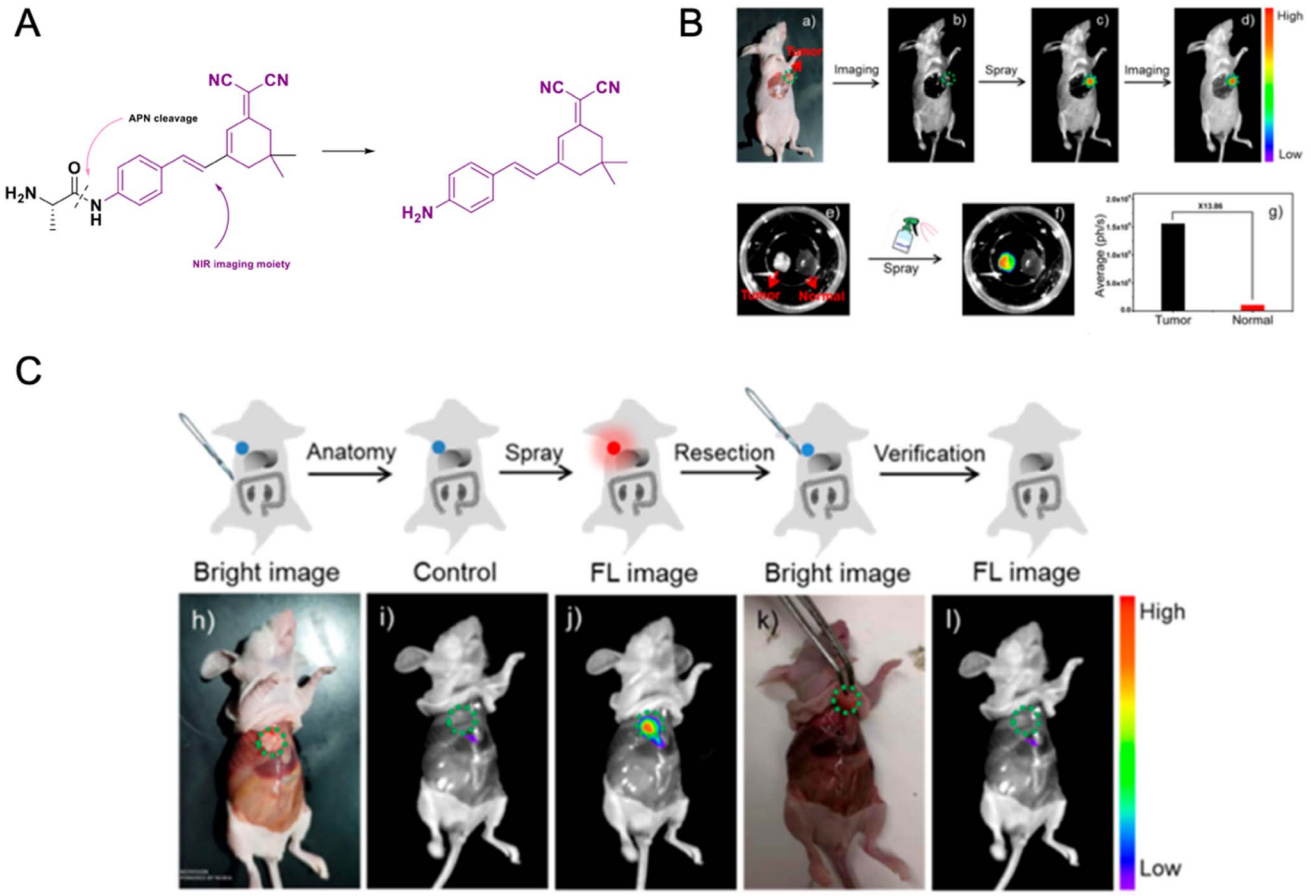

Fig. 4 The structure and application of YH-APN probe. (A) NIR fluorescence activation of YH-APN probe *via* structural restoration upon APN hydrolysis. (B) *In situ* spraying imaging *in vivo*: bright image; fluorescence image; spraying YH-APN for 30 min, then fluorescence image; the slipped effusion removed and fluorescence image. *In vitro* imaging of liver tissue and normal liver tissue through spraying probe YH-APN; statistical fluorescence intensities. (C) Image-guided resection by spraying probe YH-APN: bright image; fluorescence image; spraying YH-APN; surgical removal of tumor; respraying YH-APN, and fluorescence image. Fluorescence imaging of mouse was gathered with an excitation filter of 475 nm and an emission filter of 655 nm. Adapted with permission from ref. 49 Copyright 2020, American Chemical Society.

contrast (up to 13.9-fold) *in vivo* within 30 minutes of topical spray application. Its real-time activation enabled precise delineation of tumor margins during surgery and the detection of sub-millimeter metastatic lesions in the liver and spleen; capabilities that surpass standard clinical imaging tools. Beyond surgical guidance, **YH-APN** facilitated studies of cancer cell migration and APN involvement in metastatic behavior. Inhibition experiments with ubenimex confirmed its utility in monitoring therapeutic responses. Additionally, *ex vivo* imaging and 3D tissue reconstruction demonstrated the probe's potential for histological diagnostics and spatial mapping of enzyme activity. While the requirement for local application currently limits systemic use, the broad overexpression of APN across tumor types suggests significant translational potential in oncology.

Widen *et al.* introduced a next-generation strategy for improving protease probe specificity by designing AND-gate fluorescent probes that require cleavage by multiple enzymes for activation (Fig. 5A).[50] These probes address a common limitation of conventional single-parameter probes, namely their low signal-to-background ratios caused by nonspecific activation, tissue autofluorescence, and uneven biodistribution. The AND-gate design features a hub-and-spoke architecture, in which a central sulfo-Cy5 fluorophore is tethered to multiple quenchers *via* orthogonally cleavable peptide linkers. Fluorescence is only unmasked when all quenching groups are enzymatically removed, ensuring that activation occurs exclusively in regions where two or more specific proteases are co-expressed. Initial designs suffered from linker instability, especially in tumor lysates, which led to background activation. This was resolved by replacing L-glutamic acid in the core scaffold with its D-enantiomer, significantly improving resistance to off-target cleavage while maintaining specific responsiveness. The refined probe, **DEATH-CAT-2**, demonstrated strong performance in murine models of breast and lung cancer, targeting both lysosomal cysteine cathepsins and caspase-3. It provided superior delineation of tumor margins during surgery, successfully highlighted small metastatic lesions, and retained fluorescence post-fixation, making it compatible with histological workflows. Compared to single-substrate controls, the AND-gate probe exhibited markedly reduced background signals in non-tumor tissues including

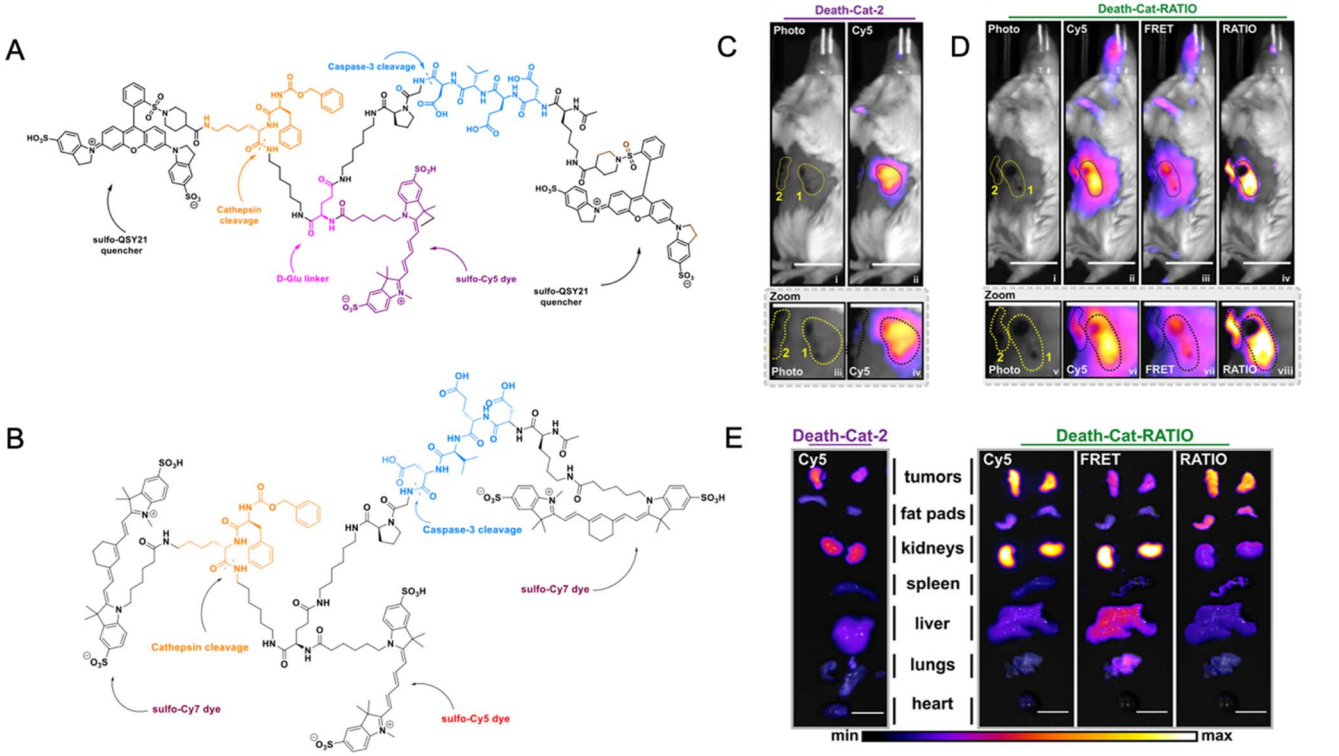

Fig. 5 Design and application of AND-gate probes. (A) Structure of **Death-Cat-2 ABP**. (B) Structure of **Death-Cat-RATIO ABP**. (C) A mouse with two breast tumors after injection with **Death-Cat-2** 24 h prior to imaging. The left panel shows the brightfield image; the right panel shows the overlay between the Cy5 channel and the brightfield image. The zoom inlet shows a magnification of the tumor. The tumor closer to the camera (area 1) is located in the third mammary fat pad; the tumor further from the camera (area 2) is located in the eighth mammary fat pad. (D) A mouse with two breast tumors injected with **Death-Cat-RATIO** 24 h prior to imaging. From left to right, the panels show the brightfield image, the overlay between the Cy5 channel and the brightfield image, the overlay between the FRET channel and the brightfield image, and the overlay between the RATIO channel and the brightfield image. The zoom inlet shows a magnification of the two tumors. The tumor closer to the camera (area 1) is located in the third mammary fat pad; the tumor further from the camera (area 2) is located in the 8th mammary fat pad. (E) Organs excised from mice injected with either **Death-Cat-2** (left panel) or **Death-Cat-RATIO** (right panel). Adapted with permission from ref. 42 Copyright 2023, The Authors. Published by American Chemical Society.

liver and kidneys. Importantly, the modular design of these probes allows for further expansion to logic systems responsive to three or more enzymes, opening avenues for ultra-selective diagnostics and future therapeutic applications. For example, the platform could be adapted for targeted drug delivery, where a cytotoxic payload is released only upon multi-protease processing within the tumor microenvironment. Compatibility with robotic surgery systems such as the da Vinci Xi Firefly further supports their translational potential.

Faucher *et al.* advanced the design of protease-activated imaging tools by developing ratiometric fluorescent probes to overcome key limitations of traditional quenched single-fluorophore systems (Fig. 5B–E).[42] Conventional probes suffer from variability caused by environmental lighting, tissue autofluorescence, and camera alignment; factors that reduce tumor visibility and increase the risk of surgical errors. To address this, the authors replaced dye-quencher designs with FRET-based constructs composed of two or more fluorophores, enabling ratiometric signal generation. For example, in the cathepsin-selective probe 6QC-RATIO, QSY-21 was replaced with Cy7 to allow FRET with Cy5, resulting in a self-normalizing signal that improved imaging contrast regardless of lighting conditions. In the AND-gate **Death-Cat-RATIO** probe, a trifluorophore architecture (two sulfo-Cy7 and one sulfo-Cy5) enabled AND-gate functionality, requiring sequential cleavage by cathepsins and caspase-3 for signal activation. These ratiometric probes demonstrated improved tumor-to-background ratios *in vivo*. **Death-Cat-RATIO** achieved a TBR of 7.23, among the highest reported for an AND-gate probe, and outperformed its predecessors by minimizing background signals in healthy organs such as the liver and kidneys. The ratiometric system also enabled accurate tumor margin delineation and detection of small metastatic lesions, even under suboptimal imaging conditions. Importantly, the technology was validated using the da Vinci Xi robotic surgery platform, confirming compatibility with clinical imaging hardware. Looking forward, the modular architecture of these probes allows for adaptation to additional fluorophore pairs, including future shortwave-infrared (SWIR) formats for deeper tissue imaging. The platform may also support endoscopic and multiplexed imaging strategies, expanding its utility in oncology, inflammatory disorders, and infectious disease diagnostics.

Continuing their work on AND-gate imaging tools, Chen *et al.* developed **Cas1-Cat-Cy7**, a dual-enzyme-activated fluorescent probe designed to selectively detect inflammasome activation by requiring sequential cleavage by both caspase-1 and cathepsins (Fig. 6).[51] Traditional probes targeting caspase-1 suffer from limited selectivity, as substrate sequences like YVAD or WEHD can be cleaved by other proteases, leading to false positives and poor signal-to-background ratios – especially in inflamed tissues with elevated vascular permeability or baseline caspase activity. To overcome this, **Cas1-Cat-Cy7** integrates two orthogonal peptide substrates into a single molecule using a D-glutamic acid scaffold. The caspase-1 recognition sequence (Tyr-*tert*-Leu-Pro-Asp) and a cathepsin-cleavable dipeptide (Phe-Lys) are linked to a sulfoCy5 fluorophore and a sulfoCy7 quencher. Only when both enzymes are active is the probe dequenched and fluorescently "turned on." The probe was further optimized with terminal amines that promote lysosomal retention, enhancing signal localization. A structurally similar negative control probe incorporating D-amino acids ensured minimal background activation. In co-culture models of macrophages and endothelial cells, the probe was selectively activated only in the presence of inflammasome stimulation, demonstrating its dual-enzyme specificity. In a mouse model of LPS/ATP-induced acute inflammation, **Cas1-Cat-Cy7** generated strong localized signals peaking around 8 hours post-injection, while the control probe remained largely inactive, confirming the importance of dual cleavage for accurate signal generation. This probe offers significant advantages for studying inflammasome biology and evaluating anti-inflammatory therapeutics. Its high specificity allows differentiation between compounds acting on upstream activators (like caspase-1) *versus* those affecting downstream inflammatory pathways. The design is also adaptable to ratiometric formats using the Cy5-Cy7 pair, which could further reduce variability and enhance quantification. With future development, dual-enzyme probes like **Cas1-Cat-Cy7** may also find utility in a range of diseases involving inflammasome dysregulation, including autoimmune, neurodegenerative, and metabolic disorders.

Kazim *et al.* reported the development of quenched activity-based probes designed to detect granzyme B (GzmB) activity in real time as a biomarker for evaluating tumor response to cancer immunotherapy (Fig. 7).[52] Immunotherapies such as immune checkpoint blockade and T cell-based treatments have transformed oncology, yet only a fraction of patients benefit. The absence of robust biomarkers to predict and monitor therapeutic response remains a major limitation. GzmB, a central effector protease released by cytotoxic T lymphocytes and natural killer cells to execute cancer cell death, represents an attractive functional readout of immune activity. Traditional antibody-based assays lack the temporal resolution and functional specificity required for dynamic monitoring, motivating the development of molecular imaging strategies. Optimization of the recognition element was achieved by replacing the canonical P1 aspartic acid of the IEPD sequence with cysteic

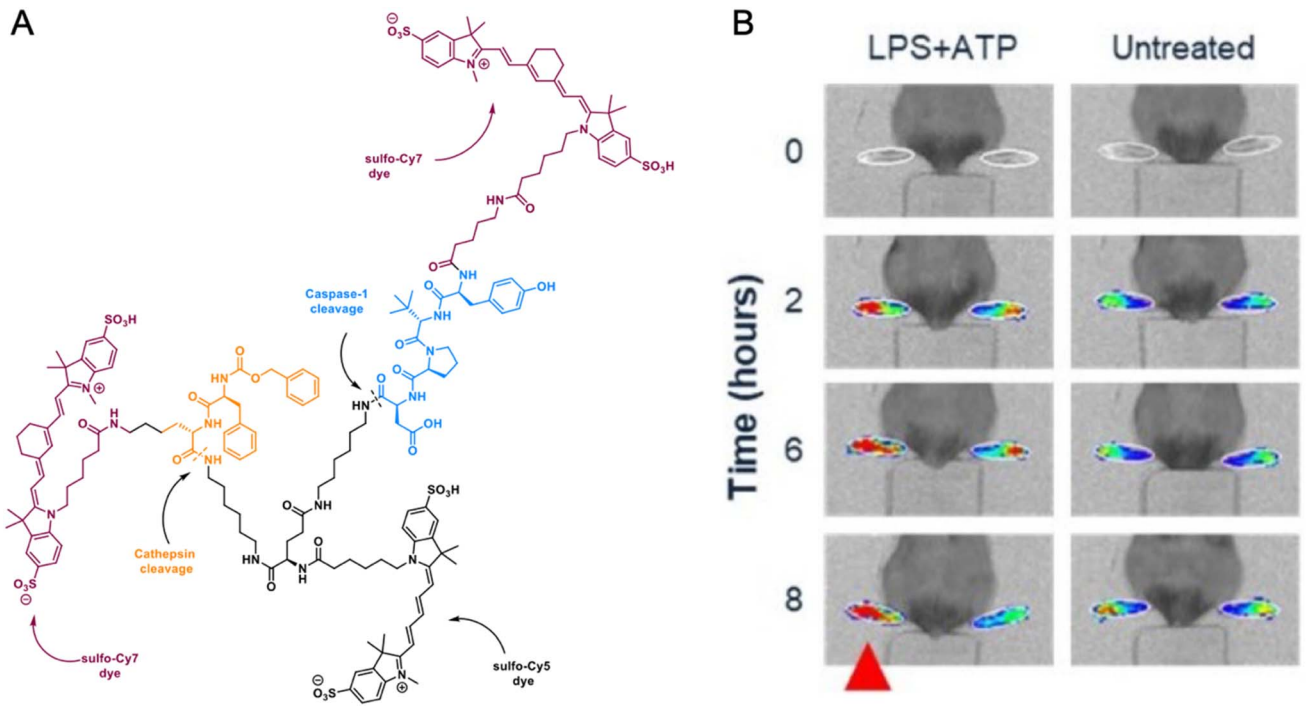

Fig. 6 The structure and application of **Cas1-Cat-Cy7**. (A) Structure of **Cas1-Cat-Cy7** ABP. (B) *In vivo* optical imaging of acute hindpaw inflammation using **Cas1-Cat-Cy7**. Representative *in vivo* fluorescence images of mice that were untreated or injected with LPS + ATP in the dorsal surface of the left hindpaw (red arrowhead). **Cas1-Cat-Cy7** and **d-Cas1-Cat-Cy7** probes were administered intravenously, and images were collected over an 8-hour period using a Cy5 filter on an IVIS SpectrumCT. Adapted with permission from ref. 51 Copyright 2025, The Authors.

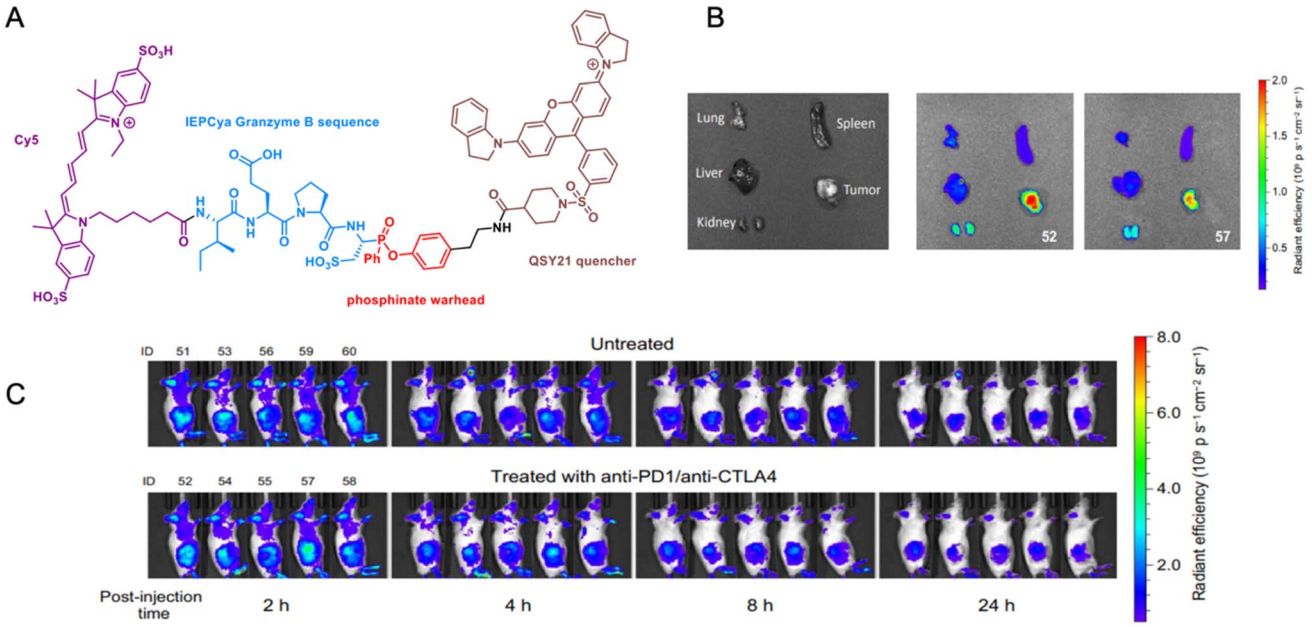

Fig. 7 The structure and application of inhibitor-based granzyme B qABP. (A) Cy5-IEPCya^{PhP}-QSY21 granzyme B probe. (B) *In vivo* imaging of granzyme B activity in mouse 4T1 tumor models. (C) Signal retention in harvested organs. Adapted with permission from ref. 52. Copyright 2025, The Authors.

acid, yielding superior kinetic efficiency and reduced cross-reactivity with caspase-8. In parallel, phenyl phosphinate ester warheads were employed in place of conventional phosphonates, eliminating secondary hydrolysis pathways and enabling rapid, clean probe activation. The lead compound, **Cy5-IEPCyaPhP-QSY21**, integrates a sulfo-Cy5 fluorophore and a QSY21 quencher for efficient FRET suppression. Comprehensive *in vitro* validation demonstrated highly selective labeling of active GzmB at nanomolar concentrations, with compatibility across human and mouse enzymes. The probe showed robust stability, efficient quenching, and negligible background activity. In NK-92 cells, the lead probe produced significantly higher signal-to-noise ratios than always-on fluorogenic substrates and successfully reported on GzmB transfer to target cancer cells during immune synapse formation. Serum stability studies confirmed sustained integrity, while optical properties provided deep tissue penetration. *In vivo* evaluation was carried out in the 4T1 breast cancer model, which is poorly immunogenic and considered challenging for immunotherapy studies. The probe enabled real-time identification of therapy responders, correlating high fluorescence signals with increased GzmB expression, $CD8^+$ T cell infiltration, and reduced tumor burden. The optimal imaging window occurred within two hours of probe administration, yielding tumor-to-background ratios exceeding fifteen. Renal clearance was confirmed as the main elimination pathway. This work represents the first demonstration of near-infrared quenched activity-based probes capable of detecting active GzmB in living systems. By combining cysteic acid-based recognition elements with phosphinate ester warheads, the probes achieve unprecedented selectivity and sensitivity. The ability to identify therapy-responsive tumors within hours of treatment initiation offers a powerful diagnostic approach for early response assessment, patient stratification, and real-time monitoring of immunotherapy efficacy. These findings establish a foundation for clinical translation of optical probes in precision oncology and highlight the potential of functional immune biomarkers to transform cancer treatment strategies.

Recently Wei *et al.* developed fluorogenic probes for imaging granzyme B activity during host immune responses to bacterial infections, with a particular emphasis on a self-immobilizing design that enhances *in situ* labeling (Fig. 8).[53] GzmB is a central effector protease of cytotoxic T lymphocytes and natural killer cells, capable of targeting multiple bacterial systems, making it an attractive biomarker for studying immune responses against drug-resistant pathogens. Three probes were constructed on a hemicyanine near-infrared scaffold, conjugated to the GzmB-specific IEPD tetrapeptide *via* a self-immolative PABA linker. Among them, **HCy-F** was engineered with a difluoromethyl substituent that generates a reactive methylene quinone intermediate upon enzymatic cleavage, enabling covalent immobilization at the site of activation. This feature prevents rapid probe diffusion, thereby improving retention and spatial resolution of fluorescence signals. Synthesis proceeded through standard Fmoc-based solid-phase peptide synthesis, PABA coupling, hemicyanine conjugation, and DAST-mediated fluorination for the self-immobilizing analog. Spectroscopic analysis showed that all probes were non-fluorescent prior to cleavage, but upon GzmB activation, they exhibited a red-shifted emission at 700 nm with up to thirty-fold fluorescence enhancement. Selectivity testing confirmed robust discrimination of GzmB over other proteases and cellular metabolites. Docking studies supported the observed high binding affinities. Cellular assays using YT natural killer cells validated probe responsiveness, with

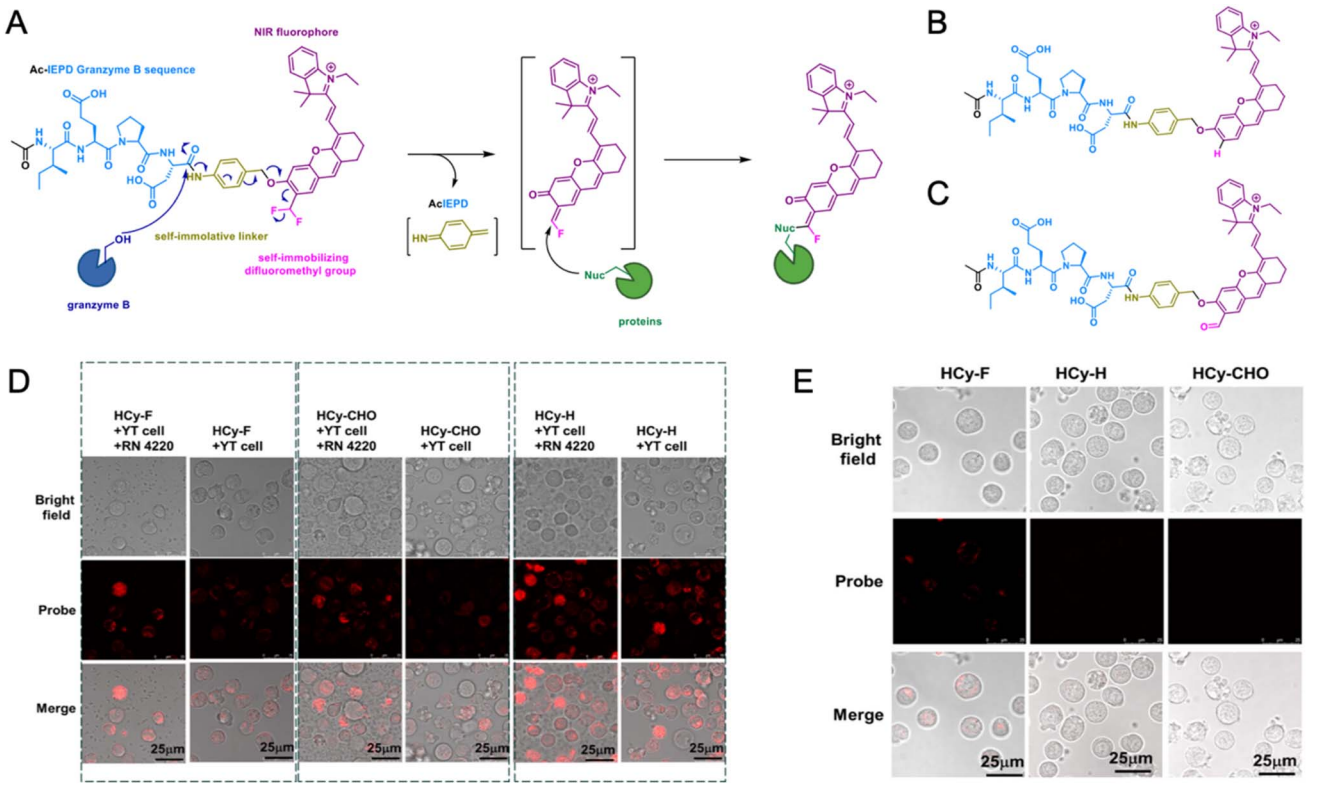

Fig. 8 The structure and application of substrate-based granzyme B probe. (A) Fluorescence activation mechanism in **HCy-F** probe. (B) Structure of **HCy-H** probe. (C) Structure of **HCy-CHO** probe. (D) NK-YT cells cocultured with or without *S. aureus* RN 4220 and visualized with the probes. (E) Retention of the probes in YT cells after washout. Adapted with permission from ref. 53 Copyright 2025 WILEY-VCH Verlag GmbH & Co. KGaA, Weinheim.

activation blocked by a specific GzmB inhibitor. Fluorescence SDS-PAGE experiments highlighted the distinct advantage of **HCy-F**, which retained strong signals even after washout, in contrast to non-immobilizing controls. In bacterial co-culture with *Staphylococcus aureus*, GzmB expression was significantly upregulated, as demonstrated by western blot and ELISA, and confocal microscopy confirmed increased probe activation in live cells. The superior retention of **HCy-F** after washing further underscored its utility for sustained and precise signal detection. Collectively, these findings establish self-immobilizing probes as powerful tools for monitoring immune dynamics. By integrating enzymatic selectivity with covalent retention, this work overcomes longstanding challenges of fluorogenic probe diffusion and clearance. The ability to visualize immune responses with high spatial resolution opens opportunities for diagnostic applications, immunotherapy monitoring, and therapeutic evaluation in drug-resistant bacterial infections. **HCy-F** thus represents a significant advance toward precision medicine approaches that harness and track the immune system's natural defense mechanisms.

The same structural motif and activation mechanism was applied by Chen *et al.* in a self-immobilizing NIR probe for *in vivo* imaging of FAP, a type II transmembrane serine protease with dipeptidyl peptidase, endopeptidase, and collagenase activities, minimally expressed in normal tissues but strongly upregulated in most carcinomas (Fig. 9).[54] However, optical probes developed to monitor FAP activity *in vivo* are limited by rapid diffusion and clearance, leading to weak signal retention and low contrast. Synthetic efforts produced **Hcy-CF_2H-PG** in two steps, confirmed by NMR analysis, and a non-immobilizing control probe lacking the difluoromethyl group **Hcy-PG**. Computational docking suggested favorable binding of **Hcy-CF_2H-PG** in the FAP active site, with close interactions to catalytic residues, while spectroscopic characterization revealed strong fluorescence enhancement and red-shifted emission after activation. *In vitro* assays showed selective activation by FAP with negligible interference from other proteases or biomolecules. SDS-PAGE and western blot confirmed covalent labeling, as fluorescence persisted after repeated washing, unlike the control probe. In HepG2 cancer cells, the probe exhibited rapid activation, high specificity, and strong resistance to washout. In tumor tissue sections and live-cell experiments, fluorescence signals closely correlated with endogenous FAP expression and were effectively suppressed by known FAP inhibitors. Crucially, detergent treatment experiments demonstrated that the self-immobilizing mechanism prevented fluorescence loss, validating covalent retention at target sites. *In vivo* imaging in HepG2 tumor-bearing mice further demonstrated the advantages of the probe. Intratumoral administration produced strong and persistent fluorescence confined to tumor tissue, while inhibitor pretreatment or use of the control probe yielded weaker or transient signals. Fluorescence light

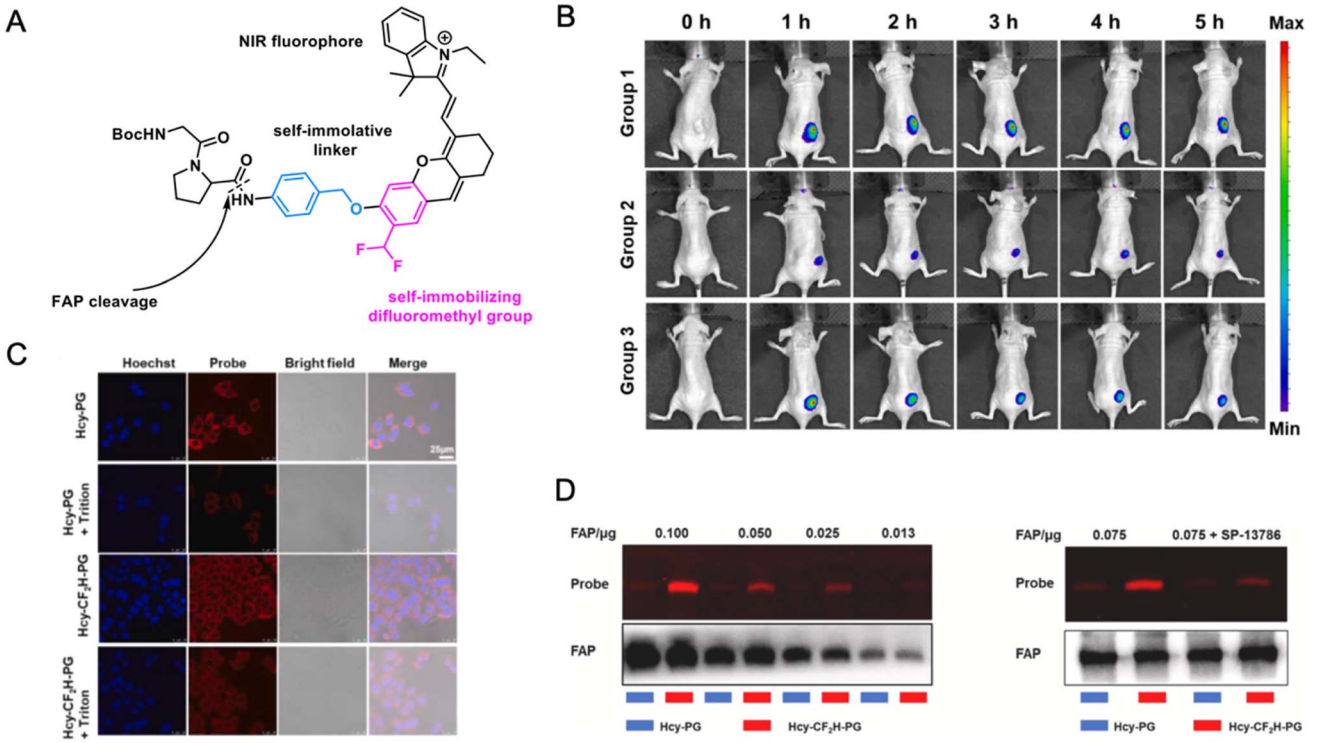

Fig. 9 Structure and application of **Hcy-CF2H-PG** probe. (A) Structure of **Hcy-CF_2H-PG** probe. (B) Representative fluorescence images of HepG2 tumour-bearing BALB/c-nu mice. Group 1 and 3 were subjected to an intratumoral injection with **Hcy-CF_2H-PG** or **Hcy-PG** for 0–5 h, respectively. Group 2 was subjected to an intratumoral injection with PT-100 (100 μM) first and then intratumorally injected with **Hcy-CF2H-PG**. (C) Fluorescence imaging of HepG2 cells incubated with **Hcy-CF_2H-PG** or **Hcy-PG** for 1 h and rinsed for an additional 0.5 h following fixation. (D) Fluorescence imaging of **Hcy-PG** and **Hcy-CF_2H-PG** incubated with recombinant FAP with of without SP-13786 (FAP inhibitor). Adapted with permission from ref. 54 Copyright 2024, Elsevier B.V.

imaging tomography combined with microCT confirmed precise localization without diffusion to adjacent tissues. The probe was well tolerated in multiple cell lines across a broad concentration range, and biodistribution studies suggested renal and hepatic clearance without systemic toxicity. The development of **Hcy-CF_2H-PG** represents a significant advance in molecular imaging by applying self-immobilization chemistry to overcome diffusion-related signal loss. This strategy enables improved tumor detection, real-time monitoring of therapeutic response, and potential guidance in surgical resection. Beyond FAP, the self-immobilizing probe design provides a generalizable approach for imaging other proteases and enzymatic biomarkers where enhanced spatial resolution and retention are essential.

2.3. Protease chemical probes in clinics

One of the most compelling success stories in the development of enzyme-responsive probes for medical applications is **VGT-309**, a quenched activity-based probe designed for intraoperative imaging of solid tumors (Fig. 10). Developed in Bogyo lab, **VGT-309**, called also abenacianine, is specifically designed to target cathepsins in cancer imaging. The probe was derived from its precursor, **BMV109**, by replacing the fluorophore and quencher pair.[38,55] It incorporates FDA-approved near-infrared ICG dye in place of far-red Cy5, enabling compatibility with multiple commercially available surgical imaging systems. QC-1 is used instead of sulfo-QSY21 to suppress fluorescence in the inactive state. **VGT-309** is an inhibitor-based probe featuring a phenoxymethyl ketone electrophilic warhead, which covalently binds to active-site cysteine residues. The probe retains the same cathepsin recognition sequence as **BMV109** (Cbz-Phe-Lys), demonstrating binding specificity for multiple cysteine cathepsins, including cathepsins X, B, L, and S. It operates through a quenching mechanism in which cathepsins covalently and irreversibly bind to **VGT-309**, displacing the QC-1 quencher. Once the quencher is removed, the ICG fluorescence is no longer suppressed, resulting in probe activation and high-contrast imaging. The main biomedical application of **VGT-309** is fluorescence-guided surgery. Suurs *et al.* showed that the probe enables real-time intraoperative tumor detection as early as one hour post-injection and provides high tumor-to-background contrast ratios in a 4T1 tumor allograft mouse model.[55] The optimal imaging window extends from 2 to at least 24 hours, offering flexible timing that supports same-day procedures. In 2022 Kennedy *et al.* reported the first comprehensive clinical translation of **VGT-309**, demonstrating selective labeling of human lung cancer cell lines and effective imaging in preclinical mouse models at 24 hours post-injection.[56] A Phase 1 safety study in 30 healthy volunteers showed that the probe was well tolerated across a range of doses with minimal

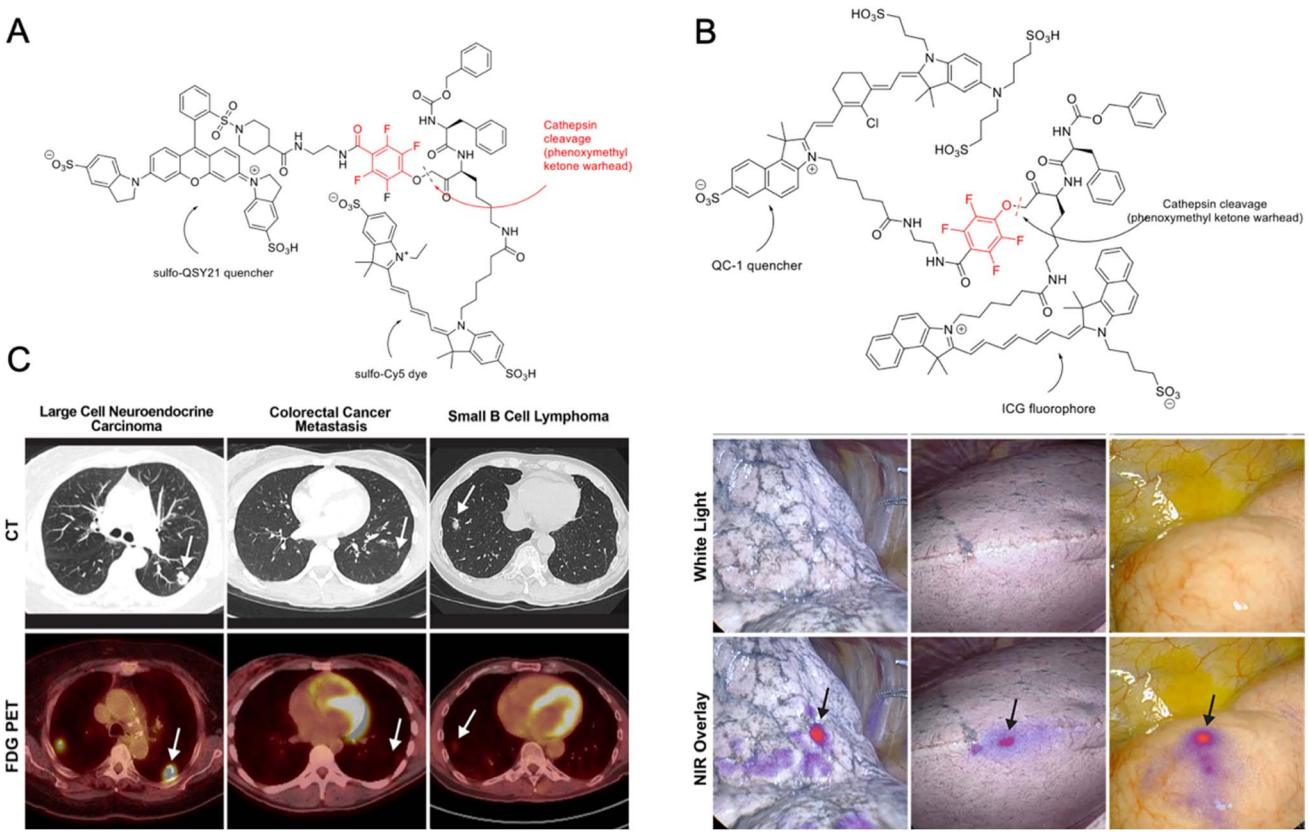

Fig. 10 The structure and application of **VGT-309** ABP. (A) Structure of the predecessor probe **BMV-109** that targets cancer-associated cathepsins. (B) Structure of **VGT-309** for intraoperative tumor imaging. (C) Intraoperative molecular imaging with **VGT-309** identified pulmonary lesions not found by standard surgical techniques. The left (large cell neuroendocrine carcinoma), middle (colorectal cancer metastasis), and right (small B cell lymphoma) columns show 3 representative locations of clinically significant event cases. Preoperative (row 1) computed tomography (CT) and (row 2) $^{[18]}$F-fluorodeoxyglucose positron emission tomography (FDG PET) imaging with lesions of interest shown with arrows. In each case, (row 3) white light only did not identify pulmonary lesions seen by preoperative imaging. Near-infrared (NIR) imaging with the Medtronic EleVision IR Platform identified all 3 lesions (row 4, white light with NIR heat map overlay). Adapted with permission from ref. 58 Copyright 2025, The Society of Thoracic Surgeons. Published by Elsevier Inc.

adverse events. In a canine study, **VGT-309** successfully labeled spontaneous pulmonary tumors, and two pilot human cases confirmed its utility in detecting lesions not visible under standard surgical lighting. Flow cytometry showed that **VGT-309** labeled both tumor cells and tumor-associated macrophages, suggesting its potential to assist in margin assessment during surgery. In the same year Kennedy *et al.* evaluated **VGT-309** for esophageal cancer detection, marking the first use of a covalent activity-based probe in this cancer type.[57] The probe demonstrated selective accumulation in esophageal cancer cells across various histological subtypes, with strong lysosomal localization and minimal background signal in normal tissues. In both syngeneic and xenograft mouse models, **VGT-309** achieved high signal-to-background ratios and accurately delineated tumor boundaries, with fluorescence abolished by a cathepsin inhibitor, confirming activity dependence. These results highlight **VGT-309**'s suitability for intraoperative guidance and endoscopic surveillance, supporting its broader application in esophageal cancer resection. Another example of **VGT-309** utility was provided by Bou-Samra *et al.* who conducted the first study of this ABP in robotic-assisted thoracic surgery with intraoperative molecular imaging (RIMI), comparing its performance to video-assisted thoracic surgery (VIMI) in a phase 2 trial involving 10 patients with suspicious pulmonary lesions.[58] **VGT-309** enabled detection of all nodules missed by white light alone, with RIMI and VIMI both identifying 80% of lesions and achieving 88.9% sensitivity and 100% positive predictive value for cathepsin activity. Fluorescence intensity was similar between the two methods, though RIMI showed higher variability in tumor-to-background ratios. The study demonstrated clinical equivalence between RIMI and VIMI and confirmed **VGT-309**'s utility for precisely locating small subpleural lesions, supporting more conservative surgical approaches. Very recently, in 2025 Bou-Samra *et al.* conducted the largest clinical study of **VGT-309** to date, a phase 2 trial involving 40 patients undergoing pulmonary resection, which met its primary endpoint with 42.5% experiencing clinically significant events such as tumor localization, detection of additional cancers, or margin identification (NCT05400226).[59] **VGT-309** successfully localized 18 of 19 nodules missed by standard techniques, with 15 confirmed as malignant, and showed strong safety with only three mild adverse events

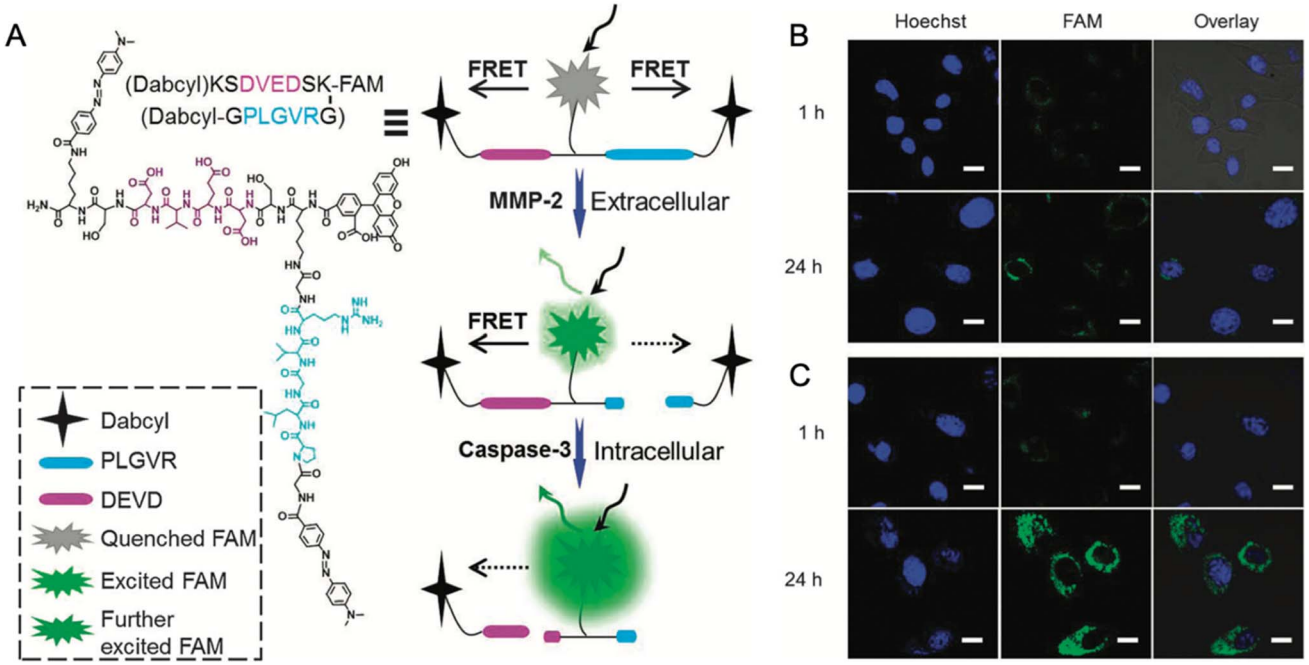

Fig. 11 Chemical probe for MMP-2 and caspase-3 imaging. (A) The chemical structure and activation mechanism of fluorescent probe sensitive to MMP-2 and caspase-3. (B and C) Fluorescent images of MMP-2 and caspase-3 activity in SCC-7 cells with (B) or without (C) doxorubicin stimulation. Excitation wavelength: 488 nm. Scale bar: 40 μm. Adapted with permission from ref. 60. Copyright 2015, The Authors. Published by the Royal Society of Chemistry.

attributed to the probe. It demonstrated 85% sensitivity and 77% positive predictive value for cancer detection, with some limitations in identifying certain adenocarcinomas and metastatic lesions. The study validated **VGT-309**'s effectiveness across multiple tumor types and its compatibility with various surgical imaging platforms, reinforcing its clinical utility for both tumor localization and intraoperative margin assessment. As of mid-2025, **VGT-309** has completed Phase 2B VISUALIZE trial (NCT06145048), which enrolled 89 patients across the US and Australia and met its primary efficacy endpoint – 45% of cases featured clinically significant surgical guidance events such as tumor localization, margin assessment, or detection of occult lesions. Based on these robust outcomes, the FDA granted Fast Track designation in January 2025, accelerating regulatory collaboration aimed at facilitating approval. The positive Phase 2 results are expected to guide the initiation of a global Phase 3 VISUALIZE-2 trial later in 2025. In parallel, a Phase I investigator-initiated study is underway to evaluate **VGT-309** during fluorescence-guided colonoscopy for colorectal cancer, further expanding its application. As cathepsins are dysregulated in a broad range of malignancies, including ovarian, brain, and soft tissue cancers, **VGT-309** stands out as a clinically viable platform for enzyme-targeted surgical navigation, with strong potential to become a standard adjunct in oncologic procedures across diverse tumor types.

Matrix metalloproteinases (MMPs) play pivotal roles across diverse pathological contexts, from tumor invasion to neuroinflammation, making them key targets for the development of enzyme-responsive imaging probes. Recent advances in probe engineering have expanded from fluorescence-based detection in cancer models to clinically translatable dual-modal systems capable of monitoring inflammatory activity in neurological disease. The following examples illustrate how rational probe design can be tailored to distinct biological settings spanning tumor progression and blood–brain barrier disruption through modulation of specificity, signal activation and imaging modality. In 2015 Li *et al.* developed a dual-FRET-based fluorescence probe, FAM-K(GRVGLPG-Dabcyl)SDEVDSK(Dabcyl), capable of sequentially detecting matrix metalloproteinase-2 (MMP-2) and caspase-3, marking a considerable advance in multi-enzyme imaging technology for cancer diagnostics (Fig. 11).[60] The probe integrates two Förster resonance energy transfer quenching systems within a single molecular scaffold, enabling distinct yet sequential fluorescence activation corresponding to extracellular and intracellular enzyme activities. Its structure features a fluorescein (FAM) fluorophore flanked by two Dabcyl quenchers linked *via* enzyme-specific peptide substrates-PLGVR for MMP-2 and DEVD for caspase-3-arranged to ensure maximal fluorescence suppression in the intact state. Upon MMP-2 cleavage, one quencher is released, partially restoring fluorescence, followed by caspase-3-mediated cleavage of the second sequence, resulting in full activation and a strong cumulative signal. The dual-FRET design achieved >94% fluorescence quenching efficiency and demonstrated precise temporal control, producing strong fluorescence enhancement upon MMP-2 and combined enzyme treatment, respectively. Enzyme specificity was confirmed through inhibitor assays, and fluorescence intensity correlated linearly with enzyme

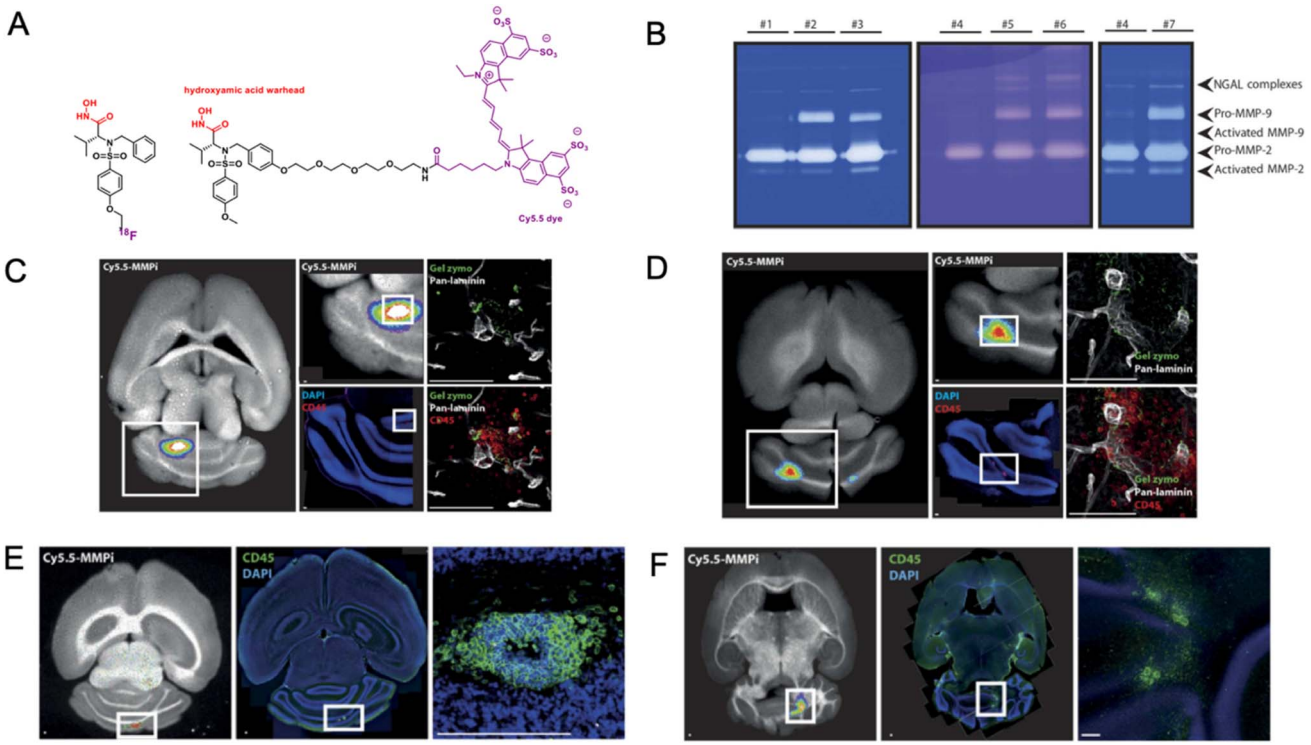

Fig. 12 **Cy5.5-MMPi** tracer signal localizes at sites of perivascular cuffs and gelatinase activity *in vivo*. (A) Chemical probe for imaging MMP-2 and MMP-9 activity in multiple sclerosis. (B) Gelatin gel zymographies of CSF samples from seven patients with suspected MS, showing positions of pro-MMP-2/9 and activated MMP-2/9 and neutrophil gelatinase-associated lipocalin (NGAL). (C and D) Five hours after intravenous administration of **Cy5.5-MMPi** (4 nmol) to two EAE mice with a clinical score of 3, the brains were cut into 200-μm thick sections and imaged using FRI. Near-infrared fluorescence (color-encoded) and white-light images were acquired and aligned (left). The same sections were then analyzed by *in situ* zymography to detect active gelatinases and subsequently stained for pan-laminin to outline vessel borders and for CD45 to identify inflammatory infiltrates (right). Scale bars: 100 μm. (E and F) FRI images of 200-μm brain sections obtained 5 hours after intravenous injection of **Cy5.5-MMPi** (4 nmol). The near-infrared fluorescence signal corresponding to high MMP activity (red) was overlaid on the white-light image. The same slice was later stained immunofluorescently with CD45 antibody, and nuclei were labeled with DAPI (blue). Two representative brains are shown in (C) and (D). Scale bars: 100 μm. Adapted with permission from ref. 61 Copyright 2016, American Association for the Advancement of Science.

concentration, allowing quantitative analysis of enzyme activity. In cellular studies, the probe effectively distinguished MMP-2-overexpressing SCC-7 cancer cells from controls and successfully monitored caspase-3 activation during doxorubicin- and UV-induced apoptosis. Real-time confocal imaging revealed time-dependent signal increases consistent with apoptotic progression, while high signal-to-noise ratios enabled no-wash imaging suitable for live-cell monitoring. The probe's sequential response mirrors physiological tumor progression, where extracellular matrix degradation by MMP-2 precedes intracellular apoptosis, providing a mechanistic link between invasion and therapy response. Overall, this dual-enzyme FRET probe establishes a powerful and generalizable platform for multi-biomarker imaging, offering enhanced diagnostic precision, therapeutic monitoring capabilities, and translational potential for personalized cancer management.

Gerwien *et al.* developed the first clinically translatable chemical probes for imaging MMP-2 and MMP-9 activity in multiple sclerosis (MS), providing a transformative approach for monitoring blood–brain barrier (BBB) disruption and neuroinflammation (Fig. 12).[61] The researchers designed dual-modal probes based on a broad-spectrum MMP inhibitor containing a hydroxamic acid zinc-binding motif, enabling both fluorescent (**Cy5.5-MMPi**) and radioactive (**18F-MMPi**) imaging modalities. The **Cy5.5-MMPi** probe, featuring a pegylated hydroxamic acid linked to a near-infrared fluorophore, allowed deep-tissue optical imaging, while the **^{18}F-MMPi** analogue was optimized for PET imaging with high radiochemical purity and clinical-grade synthesis. These probes selectively bind to the active zinc site of MMPs, with strong affinity for MMP-2 and MMP-9, achieving highly specific and irreversible labeling of enzyme activity without nonspecific diffusion. In experimental autoimmune encephalomyelitis (EAE) mouse models, probe uptake correlated with clinical severity and localized to perivascular immune cell infiltrates, confirming that probe signals directly reflected active MMP-mediated BBB breakdown. Genetic and bone marrow chimera experiments revealed that leukocyte-derived MMP-9 was essential for initiating BBB penetration, with MMP-2 serving compensatory roles at later disease stages. Translation to human MS patients demonstrated that **18F-MMPi** PET detected active inflammatory lesions with greater sensitivity than conventional gadolinium-

enhanced MRI, often identifying MMP-positive regions before visible BBB disruption. Furthermore, signal reduction following corticosteroid therapy confirmed the probe's capacity to monitor treatment response and distinguish active inflammation from residual structural damage. By enabling early and functionally specific detection of immune infiltration, MMPi-PET provides a novel biomarker for lesion activity and disease progression. Overall, this work establishes a pioneering framework for enzyme-responsive neuroimaging, demonstrating how rational chemical design and mechanism-based targeting can yield clinically viable probes that bridge preclinical discovery and precision medicine in neuroinflammatory diseases.

2.4. Challenges in chemical probes synthesis

Efficient and modular synthesis is essential for translating protease-targeted chemical probes into biomedical tools, especially when rapid iteration, scale-up, and structural optimization are needed for imaging or therapeutic use. Synthetic accessibility also determines whether a probe can transition from academic proof-of-concept to practical clinical application. To address these needs, Vanhoutte *et al.* developed a new class of azapeptide activity-based probes targeting the SARS-CoV-2 main protease (M^{pro}), an essential enzyme in viral replication (Fig. 13).[62] The probes feature an azapeptide backbone in which the α-carbon of the P1 glutamine residue is replaced by nitrogen, allowing stable resin attachment while preserving M^{pro} substrate recognition. This design enabled the modular installation of diverse cysteine-reactive warheads, including methylfumarate, chloroacetamide, and epoxysuccinate, through a solution-phase synthesis followed by solid-phase peptide elongation. Structure–activity relationship studies revealed that warhead positioning relative to the P1 site critically affects probe performance: a two-bond spacing provided optimal alignment with the M^{pro} catalytic cysteine, as confirmed by docking studies. Among the tested compounds, probe **7d** (chloroacetamide) showed the best performance, with high sensitivity (LOD = 20 nM), strong selectivity (no cross-reactivity with cysteine cathepsins), and antiviral activity (EC_{50} = 3.25 μM). The probes enabled real-time imaging of M^{pro} activity in SARS-CoV-2-infected VeroE6 cells and were used to monitor inhibition by antiviral drugs such as nirmatrelvir. Their synthesis is fully compatible with automated peptide platforms, supporting rapid generation of probe libraries. This flexibility not only facilitates hit-to-lead optimization but also opens possibilities for targeting proteases in other viruses or diseases. Beyond mechanistic studies, the approach supports diagnostic development and therapeutic monitoring by combining rational design with scalable and adaptable chemistry.

Marshall *et al.* tackled a recurring challenge in probe development: the integration of fluorescent tags without compromising peptide structure or biological performance.[63] Conventional probes often rely on bulky fluorophores appended at terminal positions, which can interfere with folding, enzymatic recognition, or bioavailability. To address this, the authors developed a concise synthetic route for intrinsically fluorescent amino acids that can be seamlessly embedded within peptide chains. Their approach centers on a one-pot Suzuki–Miyaura cross-coupling reaction, starting from a tyrosine-derived aryl nonaflate intermediate. The use of XPhos Pd G2 catalyst, potassium phosphate as base, and water as co-solvent under mild heating (60 °C) enabled efficient coupling with a variety of arylboronic acids. This strategy proved robust across a range of electron-rich, electron-poor, sterically hindered, and heteroaromatic partners, yielding a panel of thirteen novel biaryl amino acids with high overall efficiency. The process avoids harsh reagents and reduces the number of synthetic steps compared to traditional fluorescent amino acid synthesis. One of the most promising products, compound **8l**, a 4-dimethylaminobiphenyl analog, exhibited excellent photophysical properties, including a quantum yield of 0.73, high brightness, and a large Stokes shift. Its fluorescence was strongly environment-sensitive: it showed solvatochromic behavior with red-shifted emission in polar solvents and a pH-dependent signal loss under acidic conditions due to charge-transfer quenching upon protonation ($pK_a \approx 5.1$). These features make it suitable for sensing applications in variable biological microenvironments. Importantly, the synthesized amino acids were fully compatible with solid-phase peptide synthesis and could be incorporated into peptides without affecting synthetic yield or purity. To demonstrate functional utility, **8l** was used as a FRET donor in a trypsin substrate, with 2,4-dinitrophenyl-Lys as the acceptor (Fig. 14). The intact peptide displayed >90% fluorescence quenching, which was fully reversed upon proteolytic cleavage, validating its use in protease activity assays. This synthetic platform offers a practical solution to common limitations in fluorescent probe design. It enables the efficient and scalable generation of structurally minimal, tunable fluorogenic residues that can be

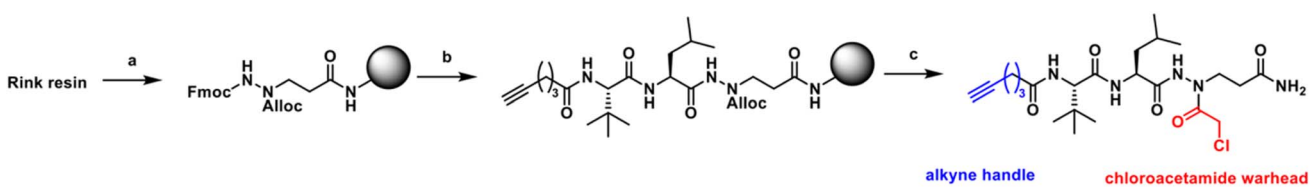

Fig. 13 The synthesis of azapeptide probe **7d**. (a) (1) 20% piperidine/DMF; (2) 2-Fmoc-1-allyl-1-(3-(*tert*-butoxy)-3-oxopropyl)hydrazine-1,2-dicarboxylate, HBTU, DIPEA, DMF, rt, overnight. (b) Repeated cycles: (1) 20% piperidine/DMF, 5 min; (2) Fmoc-Leu-OH; Fmoc-Tle-OH; or hexynoic acid - 3 h, HBTU, DIPEA, DMF, rt. (c) (1) $Pd(PPh_3)_4$, $PhSiH_3$, DCM, 30 min; (2) chloroacetyl chloride, DIPEA, DCM, rt, overnight; (3) TFA/TIPS/water 95/2.5/2.5, 30 min.

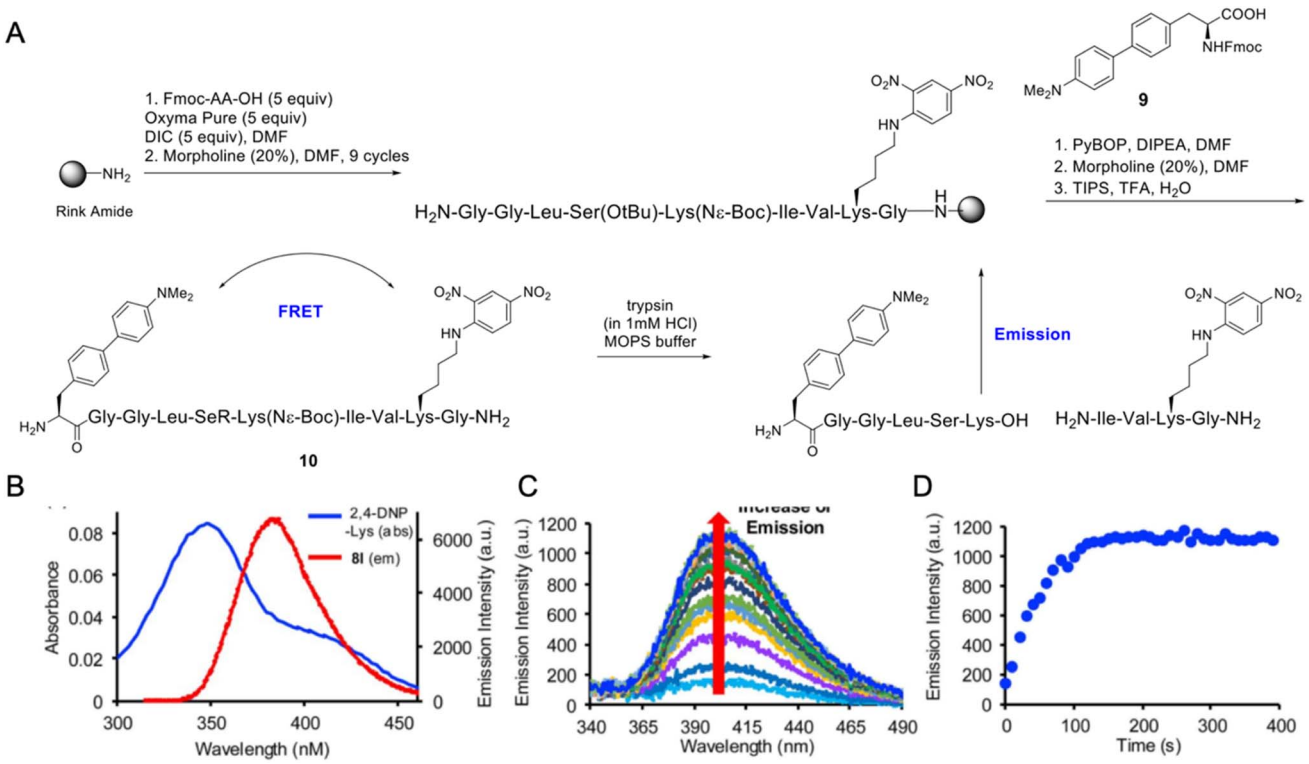

Fig. 14 Example of protease IQF substrate with novel donor–acceptor pair. (A) Solid-phase peptide synthesis (SPPS) of peptide **10**, followed by enzymatic cleavage with trypsin. (B) Spectral overlap between the absorption band of 2,4-DNP-lysine (blue trace) and the emission profile of amino acid **8l** probe (red trace). (C) Fluorescence emission spectra illustrating the progressive increase in signal during trypsin-mediated cleavage of decapeptide **10**. (D) Time-dependent plot of emission intensity during enzymatic hydrolysis of decapeptide **10**. The cleavage reaction was performed using trypsin (0.01 mM) with varying peptide concentrations (0.50–2.50 mM) in MOPS buffer (20 mM, pH 7.0); $n = 3$. Adapted with permission from ref. 63 Copyright 2025, The Authors. Published by the Royal Society of Chemistry.

embedded directly within enzyme substrates or protein tags. Beyond protease probes, the method opens opportunities in biosensor design, pH mapping, conformational studies, and even genetic code expansion strategies, where small, environmentally responsive fluorophores are highly desirable.

The synthesis of enzyme probes requires sophisticated optimization strategies to address unique challenges in protecting group selection, purification methods, and overall synthetic efficiency. Modern approaches leverage orthogonal protection strategies, advanced synthesis techniques, and streamlined purification protocols to produce high-quality probes for enzymatic studies. J. Almaliti *et al.* introduced an alternative Fmoc deprotection strategy based on palladium-catalyzed hydrogenolysis under mildly acidic conditions (Fig. 15).[64] Conventional Fmoc removal typically relies on basic secondary amines such as piperidine, which generate free nucleophilic amines and dibenzofulvene byproducts that can induce unwanted side reactions. Although acid-catalyzed or neutral hydrogenation methods have been proposed, they often require additional quenching steps or still produce nucleophilic intermediates, limiting their utility in late-stage peptide synthesis. The new approach directly converts the liberated amine into a non-nucleophilic ammonium salt, thereby preventing undesired reactions with electrophilic groups during peptide synthesis while maintaining orthogonality with Boc protections. The method was optimized and applied to Fmoc-Lys(Boc)-AOMK for the solution-phase synthesis of Z-Arg-Lys-AOMK, completed through coupling with Boc-protected arginine followed by global Boc removal using TFA. Compared with traditional protocols, it improved both yield and purity, eliminated the need for multiple chromatographic purifications, and avoided the moisture-sensitive linkers required in earlier solid-phase approaches. This acidic hydrogenolysis strategy also demonstrated broad applicability. It enabled efficient Fmoc deprotection of peptides containing α-chloroketones and facilitated one-pot Michael and Mannich reactions by allowing electrophiles to be introduced directly after deprotection without generating side products. This strategy might come useful in the development of inhibitor-based probes selective for trypsin-like serine proteases.

It is now well established that unnatural amino acids may increase selectivity and metabolic stability of probes. The synthesis of those compounds in terms of probe development remains a challenge since such building blocks must be orthogonally protected to be compatible with Solid-Phase Peptide Synthesis (SPPS). G. Geylan *et al.* addressed this gap between computational peptide design and practical synthesis by building **NNAA-Synth** – computational tool integrating orthogonal protection strategies, retrosynthetic prediction, and feasibility scoring.[65] Starting from a library of 9985 diverse

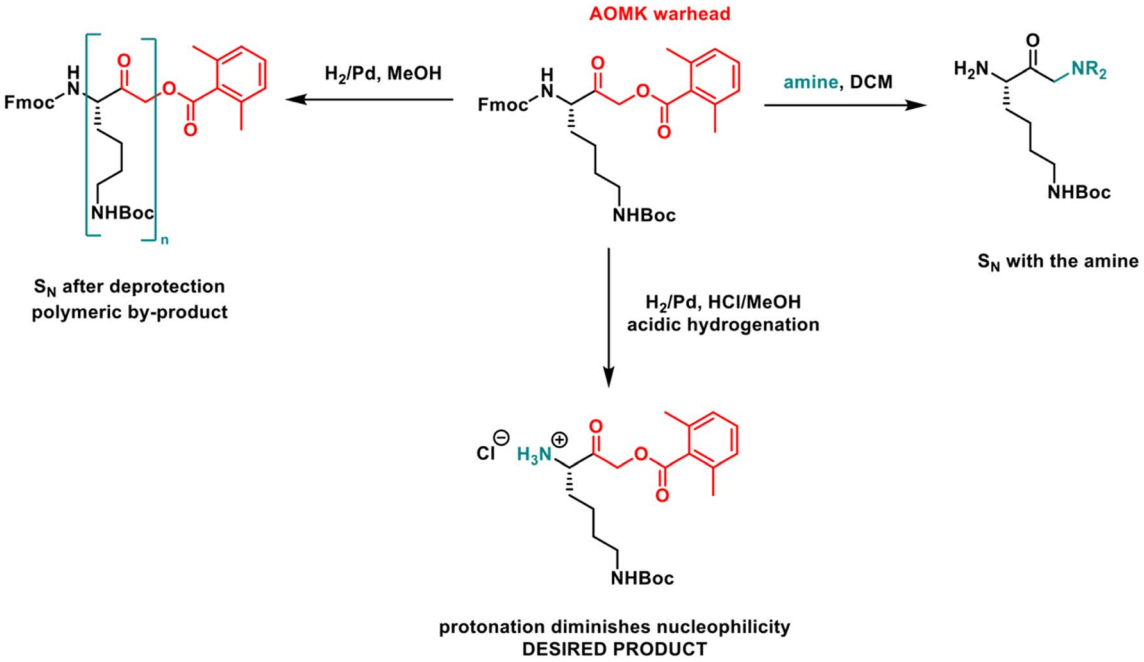

Fig. 15 The novel Fmoc deprotection strategy by acidic dehydrogenation.

amino acids, the tool identifies reactive functional groups using SMARTS patterns, applies systematic protection strategies to generate 15 508 protected variants, and conducts retrosynthetic analysis with search depths up to 15 steps. Routes are scored using deep learning models trained on USPTO data and expert assessments. Analysis revealed that about 70% of amino acids required only backbone protection, while 30% needed side-chain protection, significantly expanding molecular complexity. Out of the generated variants, 4435 protected molecules (representing 1692 NNAAs) were deemed synthetically infeasible. Among feasible candidates, 40% had routes with fewer than four reaction steps, and 20% were "solved" with all starting materials commercially available. The expert-augmented scoring system demonstrated strong correlation with human evaluation and reliably categorized routes into "Good," "Plausible," or "Bad." Practical applications included individual NNAA optimization, exemplified by amino acid 2G6, and integration with virtual screening in a Keap1-Nrf2 peptide study, where 30% of computationally promising candidates were found synthetically inaccessible. The tool represents the first computational framework combining protection strategy selection, retrosynthesis, and feasibility assessment for α-amino acids, though it currently does not address SPPS-specific issues or extend to β- and γ-amino acids.

2.5. Incorporation of unnatural amino acids in the recognition sequence

Achieving high selectivity remains one of the central challenges in chemical probe development for proteases. Many available probes are broadly reactive, making it difficult to distinguish individual proteases within complex biological samples.[66–68] This lack of specificity not only compromises imaging precision but also limits the utility of probes in mechanistic studies, drug discovery, and clinical diagnostics. Chemical probes targeting exopeptidases, such as aminopeptidases or dipeptidyl peptidases, are often constrained by their reliance on substrates composed exclusively of natural amino acids.[69] This limitation narrows the chemical diversity available for optimizing probe selectivity and activity. However, incorporating a broader range of unnatural amino acids can significantly expand the repertoire of substrate- and inhibitor-based probes, enabling the development of tools with improved enzymatic selectivity and functional performance.[70] Building on earlier advances in protease specificity profiling, the Drag laboratory has systematically employed both natural and unnatural amino acids to map substrate preferences of various enzymes (Fig. 16).[37,71] This approach has led to the generation of highly selective chemical probes with enhanced catalytic efficiency and reduced off-target activation. Using this strategy, the authors systematically investigated the substrate preferences of S1 binding pockets across a diverse panel of exopeptidases. These included: (i) aminopeptidases involved in the generation of antigenic peptides,[72] (ii) Plasmodium-derived aminopeptidases implicated in malaria pathogenesis,[73,74] (iii) human and bacterial methionine aminopeptidases (MetAPs),[75] (iv) aminopeptidases from *Porphyromonas gingivalis*,[76] (v) the alanine aminopeptidase from *Neisseria meningitidis* (NmAPN),[77] and (vi) the leucine aminopeptidase (LAP) from *Staphylococcus aureus*.[78] The approach was further extended to profiling both S1 and S2 pockets of human and malarial cathepsin C,[79] as well as malarial dipeptidyl aminopeptidases DPAP1 and DPAP3,[80] and the S1–S3 subsites of ClpP proteases.[81] The substrate specificity data obtained from these studies often correlated well with available crystallographic structures, validating the biochemical

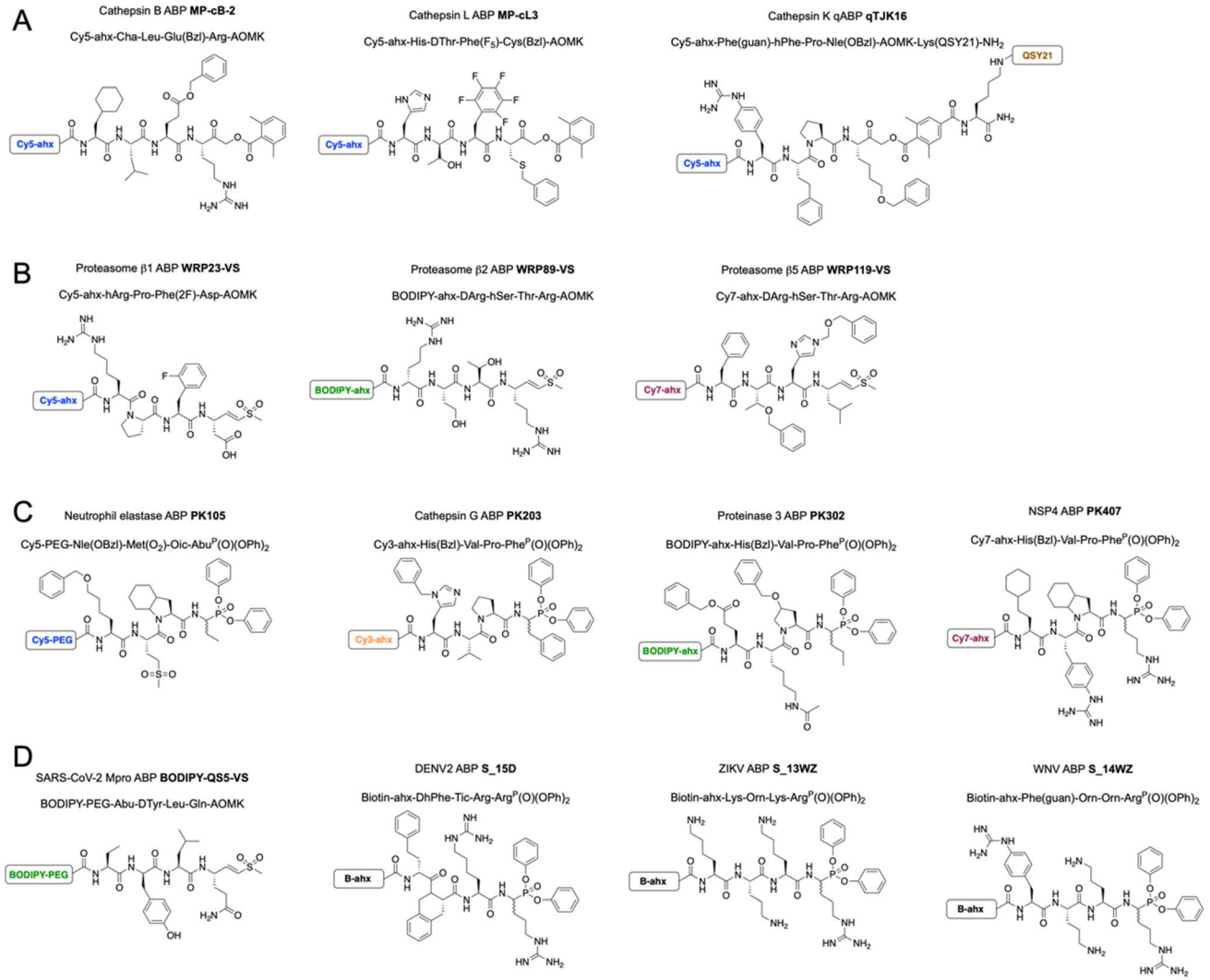

Fig. 16 The structure of selected inhibitor-based covalent activity-based probes containing unnatural amino acids for protease activity detection. (A) ABPs with an acyloxymethyl ketone warhead targeting lysosomal cysteine cathepsins: cathepsin B (**MP-cB-2**), cathepsin L (**MP-cL3**), and cathepsin K (**TJK16**). (B) ABPs with a vinyl sulfone warhead selective for the three catalytic subunits of the 20S proteasome: β1 (**WRP23-VS**), β2 (**WRP89-VS2**), and β5 (**WRP119-VS5**). (C) ABPs with a diphenylphosphonate warhead targeting neutrophil serine proteases: neutrophil elastase (**PK105**), cathepsin G (**PK203**), proteinase 3 (**PK302**), and NSP4 (**PK407**). (D) ABPs for viral proteases: SARS-CoV-2 main protease (**BODIPY-QS5-VS**) and NS3B/NS3 serine proteases from DENV2 (**S_15D**), ZIKV (**S_13WZ**), and WNV (**S_14WZ**). Ahx – aminohexanoic acid linker; PEG – polyethylene glycol (PEG4) linker; Cy3, Cy5, Cy7 – cyanine dyes 3, 5, and 7, respectively; B – biotin; QSY21 – a Cy5-quencher fluorophore.

findings and providing detailed molecular insight into enzyme–substrate recognition. Importantly, the results enabled the rational design and synthesis of organophosphorus-based inhibitors and activity-based probes (ABPs) targeting MetAPs, NmAPN, and DPAPs. These chemical tools demonstrated high potency and selectivity, underscoring the utility of combining positional scanning with unnatural amino acids to guide the development of next-generation probes for functionally and clinically relevant exopeptidases.

To develop probes for endoproteases, the Hybrid Combinatorial Substrate Library (HyCoSuL) approach was established as a powerful platform for peptide optimization.[71] This method builds upon earlier profiling techniques such as the Positional Scanning Substrate Combinatorial Library (PS-SCL), which rely exclusively on the 20 canonical amino acids.[82,83] In contrast, HyCoSuL incorporates a broad range of unnatural amino acids, greatly expanding the chemical diversity and conformational space that can be explored within protease binding pockets. HyCoSuL libraries are typically constructed as tetrapeptide substrates conjugated to a fluorogenic leaving group. This design enables systematic mapping of the S4–S1 subsites of proteases, revealing distinct substrate preferences and key recognition features that can be exploited for the development of selective probes. Over the past decade, the HyCoSuL strategy has provided critical insights into substrate specificity across a broad spectrum of proteases, including caspases, cathepsins, calpain, neutrophil serine proteases, 20S proteasome and viral proteases.[79,84–90] This approach has facilitated the rational design of activity-based probes, fluorogenic substrates, and inhibitors with markedly improved selectivity and kinetic

performance. These advances have opened new avenues for therapeutic targeting, particularly in systems where protease families exhibit high sequence and structural similarity.

Cancer-associated protease imaging has proven valuable for diagnostics, as demonstrated by the intraoperative use of cathepsin-cleavable probes.[8,57] Developing next-generation probes that incorporate peptides with improved selectivity toward individual proteases represents a promising direction for future biomedical applications. Such selective peptides can be directly identified through HyCoSuL screening and integrated into probe design (Fig. 16A). Poreba *et al.* used this approach to develop highly selective chemical probes for imaging cathepsin L activity in breast cancer cells.[84] Screening over 100 unnatural amino acids at P4–P2 (with fixed P1 arginine) revealed strong preferences for phenylalanine derivatives at P2, D- and basic residues at P3, and basic residues at P4. Further profiling identified cysteine analogs at P1 that enhanced both activity and selectivity. These insights enabled the design of selective fluorogenic substrates, such as Ac-His-DThr-Phe(F_5)-Cys(Bzl)-ACC, and conversion into Cy5-labeled activity-based probes with AOMK warheads. The most selective probe, **MP-cL3**, showed robust labeling of cathepsin L in cell models, with minimal cross-reactivity. Another example of a chemical probe developed using the HyCoSuL approach targets the cancer-associated protease cathepsin B.[85] Following a similar strategy, Poreba *et al.* profiled cathepsin B specificity using two complementary libraries, one exploring over 100 unnatural amino acids at P1, and another mapping P4–P2 preferences with fixed P1 arginine. While cathepsin B preferred arginine among natural residues, several bulky hydrophobic analogs, such as Lys(2-Cl-Z) and Cys(Bzl), were cleaved even more efficiently. The enzyme also favored large hydrophobic amino acids at P2 and aliphatic residues at P3, with minimal selectivity at P4. These insights led to the development of the highly selective substrate Ac-Cha-Leu-Glu(Bzl)-Arg-ACC, which exhibited over 3500-fold selectivity for cathepsin B over cathepsin L. This sequence was converted into Cy5-labeled activity-based probes, with **MP-CB-2** demonstrating optimal potency and selectivity. The probe showed robust cathepsin B labeling across multiple cancer cell lines and in clinical lung tumor samples, confirming its utility for both basic and translational research. Another examples of selective probe for cancer-related protease includes cathepsin K.[91] Fluorescent substrates like Ac-Phe(guan)-hPhe-Pro-Nle(OBzl)-ACC (**TJK16**) achieved high catalytic efficiency and selectivity. An irreversible inhibitor was synthesized by attaching an AOMK warhead to the **TJK16** scaffold. A quenched activity-based probe (**qTJK16**) was created by incorporating a Cy5 fluorophore, QSY21 quencher, and AOMK. These tools demonstrated strong selectivity for CatK with minimal off-target activity and facilitated real-time imaging and functional studies in osteoclasts, underscoring their biological relevance.

Caspases also play important roles in cancer; however, unlike cathepsins, they are not direct markers of cancer cells. Instead, they serve primarily as biomarkers for evaluating the effectiveness of apoptosis-inducing therapies.[92,93] Our group has contributed to this field by developing caspase-selective peptides incorporating unnatural amino acids, which have been further converted into chemical probes.[26,79] These probes target both apoptotic and inflammatory caspases. In a recent example, caspase-6 activity was detected in apoptotic cells, particularly in leukemic T cells, using aggregation-induced emission (AIE) substrate probes.[94] For cellular imaging, tetraphenylethene (TPE)-based fluorogens were conjugated to alkyne-functionalized peptides *via* click chemistry, resulting in AIE substrates with high selectivity for caspase-6. Imaging studies in Jurkat T cells revealed the temporal dynamics of caspase activation during apoptosis. Additionally, mass cytometry combined with selective inhibitors confirmed the specificity of the probes and enabled real-time, single-cell analysis of caspase-6 activity. On the other hand, inflammatory caspases can be monitored to visualize cell lysis and detect ongoing inflammation.[95] Selective chemical probes for proinflammatory caspases, caspase-1, -4, -5, and -11, were developed using an innovative delivery strategy in which membrane-impermeable probes gain entry exclusively into pyroptotic cells through gasdermin D (GSDMD) pores.[96] This approach allows precise detection of inflammatory caspase activity in the context of pyroptosis and immune activation. Another example of imaging cancer-relevant protease was demonstrated by Rut and colleagues, who developed a set of selective ABPs for the human constitutive 20S proteasome (Fig. 16B).[89] Targeting the β1 (caspase-like), β2 (trypsin-like), and β5 (chymotrypsin-like) catalytic subunits, they designed fluorochrome-labeled probes with VME warheads based on HyCoSuL-optimized peptide sequences. These probes, **WRP23-VS**, **WRP89-VS**, **WRP119-VS**, enabled parallel imaging of individual proteasome activities in cells and were shown to be effective tools for monitoring functional proteasome states, for instance in response to proteasome inhibitors such as bortezomib.

Neutrophil serine proteases are key proteases stored in neutrophil azurophil granules, and four proteases belong to this group: neutrophil elastase (NE), cathepsin G (CATG), proteinase 3 (PR3), and neutrophil serine protease 4 (NSP4). The activity of these enzymes is essential for neutrophil-mediated host defense, including pathogen degradation, regulation of inflammation, and formation of neutrophil extracellular traps (NETs).[97,98] Importantly, accumulating evidence highlights that dysregulated activity of NSPs also contributes to cancer progression by promoting tumor-associated inflammation, extracellular matrix remodeling, angiogenesis, and metastasis.[99] In 2014, Kasperkiewicz and colleagues profiled the substrate specificity of human neutrophil elastase using the HyCoSuL strategy.[86] The resulting substrate with unnatural amino acids (Nle(OBzl)-Met(O_2)-Oic-Abu) displayed over 7000-fold improved activity over classical substrates (Ala-Ala-Pro-Val) and was further converted into a biotinylated phosphonate probe (**PK101**) that selectively labeled active NE in neutrophils, particularly during NET formation. Building on this approach, in 2017 the same group expanded the probe toolbox to target the full panel of neutrophil serine proteases.[87] By applying the HyCoSuL approach and leveraging distinct substrate preferences in the S4–S1 subsites, they created highly selective fluorophore-conjugated ABPs for neutrophil elastase (**PK105**),

cathepsin G (**PK203**), PR3 (**PK302**), and neutrophil serine protease 4 (**PK407**), each distinguishable by different spectral signatures (Fig. 16C). This allowed for the first time the simultaneous visualization of all four proteases in primary human neutrophils, revealing a mutually exclusive localization pattern within azurophil granules. These studies collectively demonstrated the power of chemical probe design for specific and parallel imaging of neutrophil protease activity and laid a foundation for studying their roles in health and disease at the single-cell level.

Next to cancer-associated proteases and inflammatory proteases, viral proteases are also good targets for the development of chemical probes for biomedical applications (Fig. 16D). In one of such study, the authors applied the HyCoSuL approach to profile the substrate specificity of SARS-CoV-2 main protease (M^{pro}), identifying key preferences for natural and unnatural amino acids at P4–P2 positions.[88] This enabled the design of potent inhibitors and ABPs with vinyl sulfone warheads. Crucially, one optimized ABP (**Bodipy-QS5-VS**) successfully visualized active SARS-CoV-2 M^{pro} in nasopharyngeal epithelial cells from COVID-19 patients using confocal microscopy. In another study, HyCoSuL profiling revealed distinct substrate specificity differences between Dengue virus (DENV) NS2B-NS3 protease *versus* Zika (ZIKV) and West Nile virus (WNV) orthologs, particularly at P2 and P4 positions.[100] This knowledge allowed the design of peptide sequences selectively recognized by DENV protease, which were converted into phosphonate-based ABPs. These probes enabled specific detection and differentiation of DENV protease from ZIKV/WNV proteases in SDS-PAGE assays. Together, HyCoSuL-derived chemical tools provide structural frameworks for inhibitor design and have direct biomedical applications, such as imaging active viral proteases in patient samples or differentiating closely related viral pathogens diagnostically. A practical limitation of HyCoSuL is the expense of the non-natural amino acids required to assemble comprehensive positional libraries. However, these libraries are reusable across enzyme families. The P1-Asp HyCoSuL, first built for apoptotic caspases, has also been applied to inflammatory caspases, granzyme B, legumain and the β1 subunit of the 20S proteasome, whereas the P1-Arg HyCoSuL has seen even broader use with cysteine cathepsins, NSP4, trypsin, matriptase and others. This cross-applicability amortizes the upfront synthetic investment. Although early costs were high because many Fmoc-protected amino acids had to be made *de novo*, the growing commercial availability and routine use of non-natural amino acids have reduced prices. As a result, HyCoSuL screening has become increasingly affordable and accessible.

2.6. DNA-binding dyes as reporter tags in protease chemical probes

In classical substrate-based probes, the reporter tag is released into the cytoplasm following bond cleavage, where it can readily diffuse or be washed away – resulting in signal attenuation over time. However, this limitation can be mitigated by selecting fluorophores that become retained within the cell upon enzymatic activation. For example, aggregation-induced emission fluorophores form hydrophobic aggregates after hydrolysis, which tend to remain localized within cells or tissues.[101] This prevents diffusion or leakage from the site of enzymatic activity, enabling more accurate and sustained imaging over time. In contrast, traditional fluorophores such as coumarin analogies are more prone to diffusion, reducing spatial fidelity. An especially promising strategy, particularly for clinical translation and broader biomedical application, involves the use of DNA-binding dyes.[102] Upon release, these dyes can remain inside the cell due to non-covalent interactions with nuclear DNA. Additionally, many of these dyes exhibit significant fluorescence enhancement upon DNA binding, which not only improves imaging contrast but also allows simultaneous visualization of nuclear morphology (Fig. 17A).

In 2008, H. Cen *et al.* introduced a caspase-3-selective probe incorporating a DNA-intercalating fluorophore.[102] The probe was designed by conjugating a caspase-selective Ac-DEVD peptide sequence to NucView488, a fluorophore derived from thiazole orange, a well-known DNA intercalator (Fig. 17B). Like thiazole orange, the probe was fluorescent only when bound to DNA, due to conformational restrictions. A critical design challenge was ensuring the dye remained non-fluorescent and DNA-inactive until cleaved by caspase-3. DNA-binding properties of such dyes are typically associated with their cationic character, given DNA's overall negative charge. To overcome premature DNA interaction, the researchers masked the dye's binding ability by attaching the negatively charged DEVD sequence to obtain **DEVD-NucView488**. Only upon enzymatic cleavage was the dye's positive charge restored, reinstating its DNA-binding capacity. This design enabled selective detection of caspase-3 activity with high signal-to-noise ratios. Furthermore, the probe effectively addressed limitations associated with poor cell permeability and retention, which typically restrict non-permeable probes to cell lysates and preclude single-cell resolution. **DEVD-NucView488** enabled detection of caspase-3 activation within 30 minutes, much faster than traditional assays, allowing real-time monitoring of enzyme activity in living cells. Its speed, specificity, and capacity for single-cell imaging underscore the potential of this approach for kinetic studies and heterogeneity analysis. Notably, the probe's dual function – reporting enzyme activity while staining DNA, offers opportunities for multiparametric imaging. The authors also proposed that this design strategy could be adapted for detecting other enzymes by replacing the DEVD sequence with alternative recognition motifs. Similarly, the fluorophore component could be varied to suit different experimental needs. Overall, this research outlines a promising direction for next-generation protease probes, while also highlighting key technical and conceptual challenges that must be addressed for broader live-cell and clinical applications. Although DNA-binding dyes have also been used in probes for monitoring histone deacetylase activity,[103] concept appears to have received limited attention in the context of ABPs. To the best of our knowledge, the structure of only one commercially available caspase-3/7 detection reagent has been published: **DEVD-NucView488** by Cen *et al.* which provide much room for further development.[102]

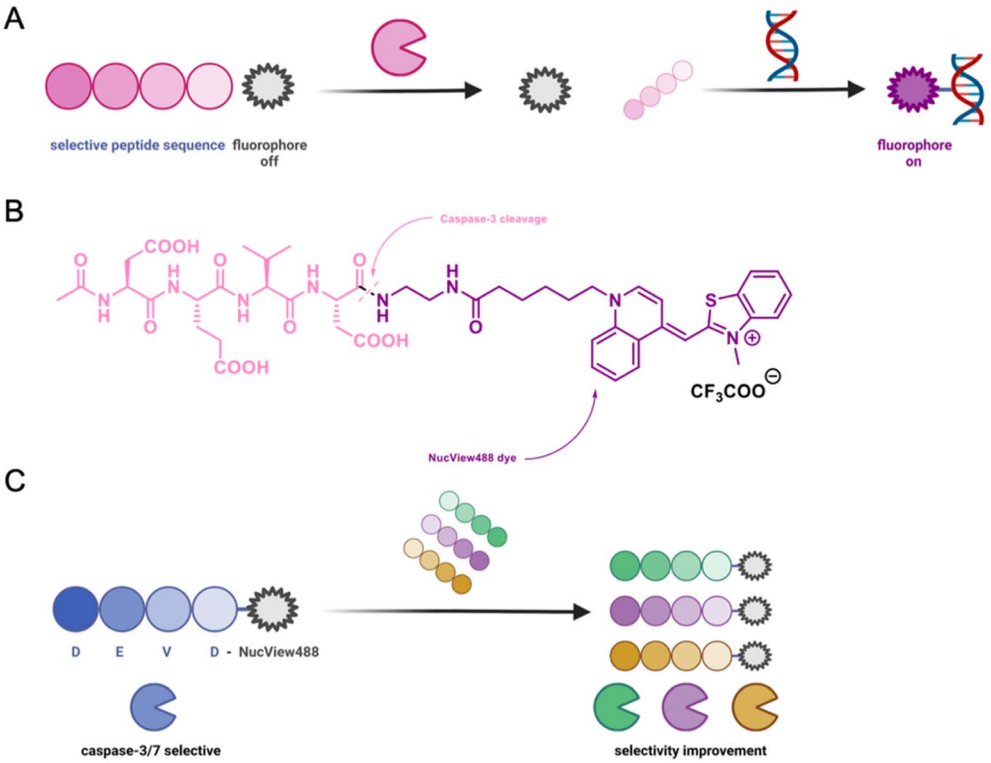

Fig. 17 Protease detection through substrates with DNA-binding dye. (A) Intercalation-induced fluorescence. (B) Structure of caspase-3/-7 DEVD-NucView488 ABP. (C) The application of HyCoSuL strategy for the development of protease-selective probes with NucView488 dye.

The HyCoSuL methodology's success represents a significant advancement in protease research methodology, demonstrating that incorporation of unnatural amino acids can yield substrates and inhibitors with enhanced selectivity profiles. Eliminating cross-reactivity with related enzymes establishes HyCoSuL as a valuable route for developing selective chemical probes for various proteases. The use of DNA-binding fluorophores in substrate-based probes significantly enhances signal-to-noise ratio and intracellular retention, distinguishing them favorably from classical fluorescent substrates. Based on the examples presented, we propose that integrating such dyes with the HyCoSuL strategy could lead to the development of novel, highly selective, real-time protease imaging probes (Fig. 17C). Such chemical tools are currently under development in our laboratory. Furthermore, DNA-binding fluorophores operating in the near-infrared (NIR) and NIR-II ranges are also known offering promising avenues for deep-tissue imaging and clinical translation.[104]

3. Luminescent probes for proteases

Chemiluminescent probes have provided new modality for enzyme activity imaging by removing the need for external excitation light, thus eliminating background interference from tissue autofluorescence and light scattering. The phenoxy-1,2-dioxetane scaffold serves as a highly adaptable platform, allowing precise tuning of photophysical properties through chemical modifications (Fig. 18).[105,106] These probes operate *via* the chemically initiated electron exchange luminescence (CIEEL) mechanism, where enzyme-triggered decomposition generates light-emitting intermediates for real-time enzyme monitoring. Recent advances have improved sensitivity, emission longevity, and near-infrared performance, enabling powerful applications in disease diagnosis, surgical imaging, and dynamic biological process visualization.

Recent developments have yielded several promising probes with validated utility in cancer diagnostics and therapeutic monitoring. A notable example is a chemiluminescent probe

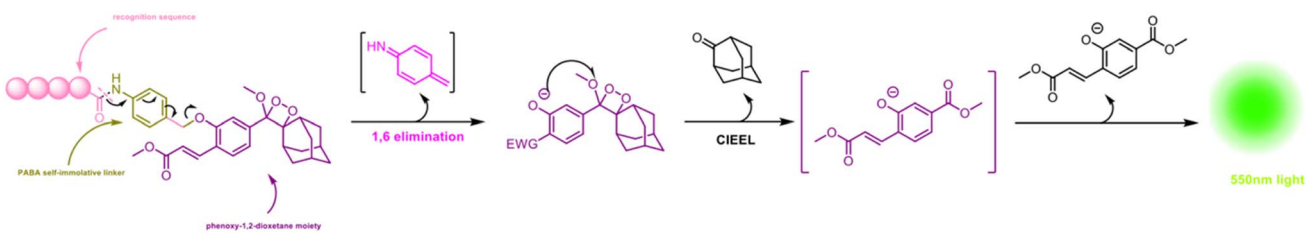

Fig. 18 A mechanism of chemiluminescence emission through proteolytic cleavage.

(Probe **1**) for leucine aminopeptidase (LAP) developed by Wang *et al.* (Fig. 19).[107] The probe employs a caged L-leucine recognition motif, a self-immolative linker (PABA), and a phenoxy 1,2-dioxetane luminophore. Upon LAP-mediated cleavage, a cascade reaction is triggered, producing a strong chemiluminescent signal without the need for external excitation. Compared to conventional fluorogenic probes such as Leu-AMC (7-amino-4-methylcoumarin), this design achieved a 27.5-fold increase in sensitivity and an exceptional signal-to-noise ratio (>1200). These features enabled real-time LAP detection in cancer cells, animal models, and human liver cancer tissues. Importantly, the probe differentiated malignant from healthy tissue with high contrast and responded within 10 minutes post-injection, aligning well with intraoperative imaging demands. Its lack of background activation, resistance to nonspecific enzymes, and quantitative performance further highlight its diagnostic potential. While the current emission profile (~550 nm) limits deep-tissue imaging, future iterations with near-infrared output are under development. This example illustrates how structure-based design, combined with chemiluminescence, can address major limitations of traditional fluorescence probes and push enzyme-targeted diagnostics closer to clinical translation. The same probe was reported by Sun *et al.*[108] By employing an uncapped leucine recognition group, the design ensures efficient enzymatic cleavage, as demonstrated by a 183-fold higher luminescence compared to the Boc-protected control probe, confirming substrate accessibility as essential for APN specificity. **APN-CL** exhibits remarkable sensitivity, low detection limit and a broad linear response range suitable for clinical quantification. The probe displays excellent selectivity against potential interferents, high stability under physiological conditions, and negligible cytotoxicity, validating its biocompatibility for live-cell and animal imaging. In cell assays, **APN-CL** successfully distinguished APN-overexpressing HepG2 cancer cells from normal LO2 cells, while *in vivo* studies in tumor-bearing mice demonstrated rapid, inhibitor-sensitive luminescence localized to APN-active tissues. Clinically, **APN-CL** showed strong correlation with ELISA-based measurements in human plasma and proved valuable for screening APN inhibitors, accurately reproducing known IC_{50} values. Its light-free activation circumvents autofluorescence and photobleaching issues, achieving a superior signal-to-noise ratio compared to fluorescence probes. Overall, **APN-CL** represents a major advancement in chemiluminescent probe design, offering a powerful and versatile tool for enzyme imaging, clinical diagnostics, and therapeutic screening.

In another study Shi *et al.* introduced **Ala-PD**, an aminopeptidase N (APN)-activatable chemiluminescent probe engineered for precise image-guided surgery (IGS) and metastasis tracking, representing a major advance over fluorescence-based intraoperative imaging (Fig. 20A).[109] The probe's tripartite molecular design integrates an L-alanine substrate for APN recognition, a *p*-aminobenzyl alcohol (PBAB) self-immolative linker, and an acrylonitrile-substituted Schaap's adamantylidene-dioxetane (SAD) core, yielding high quantum efficiency and long-lasting light emission. Upon APN-mediated cleavage of the alanine group, the PBAB linker undergoes spontaneous fragmentation, releasing the dioxetane luminophore and producing intense, background-free chemiluminescence. **Ala-PD** exhibits exceptional sensitivity, detecting APN down to 0.531 ng mL^{-1} with a wide linear range and strong selectivity against other enzymes and ions, while its signal is completely inhibited by the APN-specific inhibitor ubenimex, confirming mechanistic specificity. In cell-based studies, the probe showed excellent biocompatibility, discriminating hepatocellular carcinoma cells from normal hepatocytes

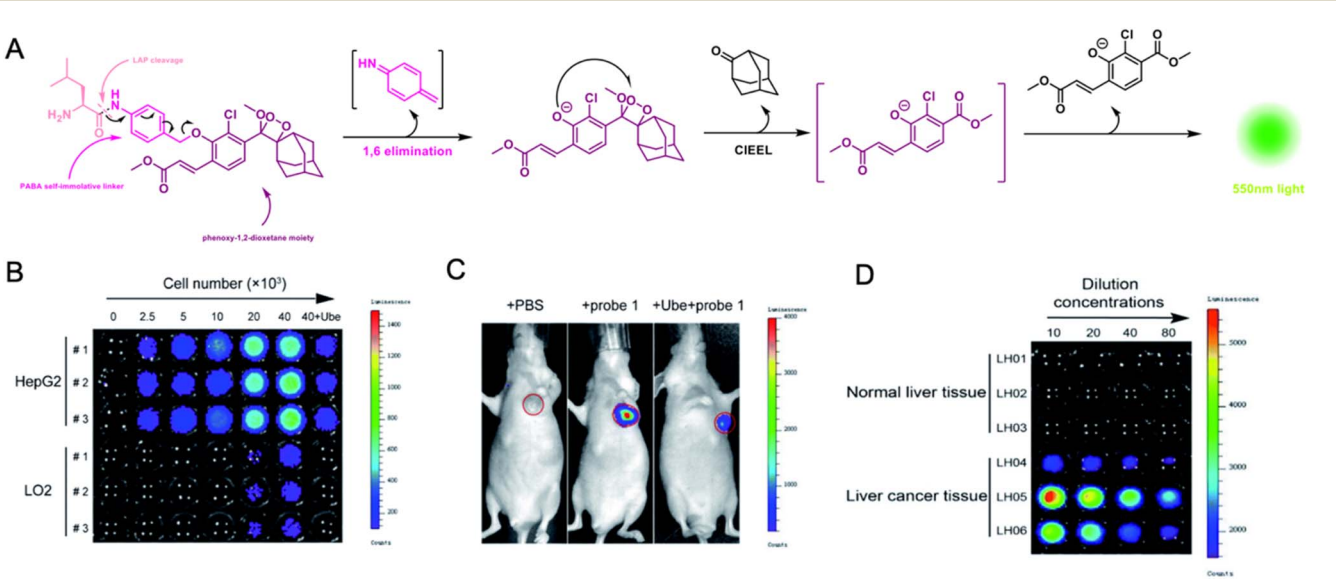

Fig. 19 Substrate-based chemiluminescent probe for LAP. (A) Chemiluminescence activation mechanism upon LAP cleavage. (B) Chemiluminescence images of HepG2 and LO2 cells after incubation with chemical probes. (C) Chemiluminescence imaging of LAP activity in HepG2 tumor-bearing BALB/c nude mice with Probe **1**. (D) Chemiluminescence imaging and detection of LAP activity with probes in human tissue samples. Adapted with permission from ref. 107 Copyright 2022, The Authors. Published by the Royal Society of Chemistry.

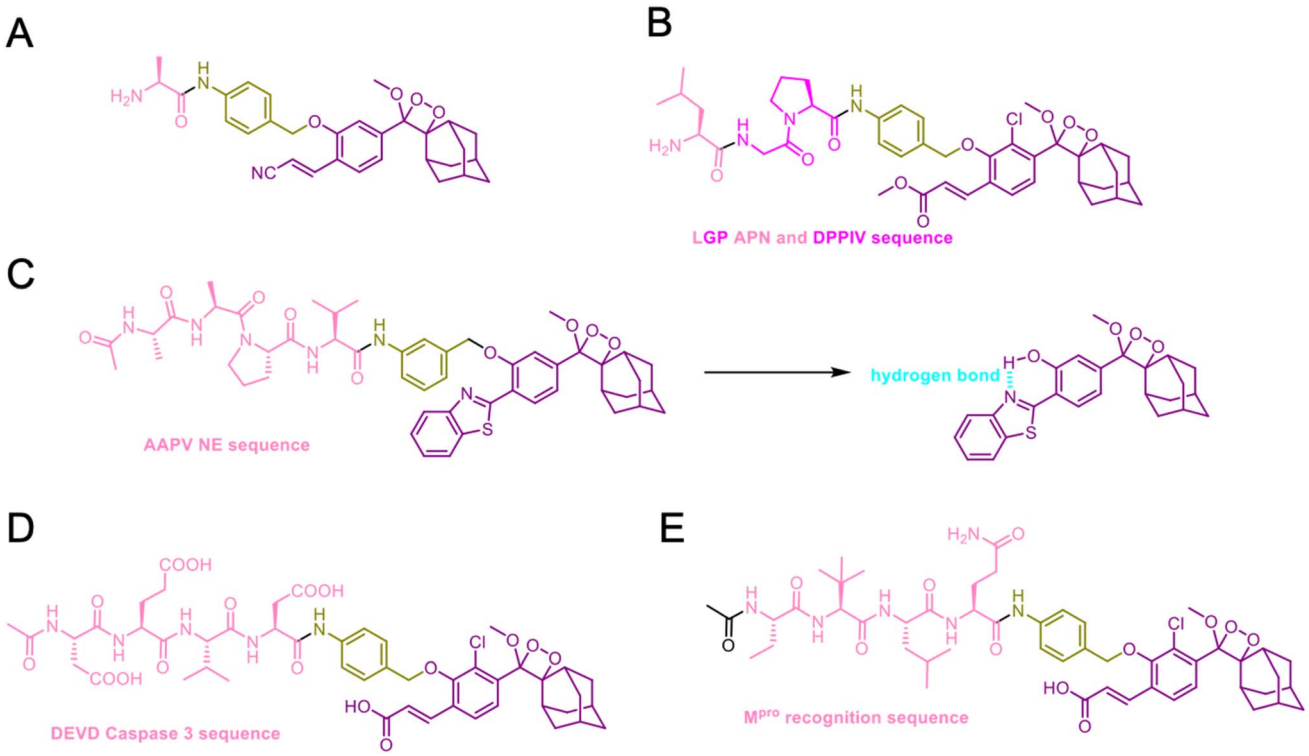

Fig. 20 Chemiluminescent probes for proteases. Structures of (A) **Ala-PD** (Ala aminopeptidase), (B) **APN-CL** (aminopeptidase and DPPIV), (C) $BTPD_{Ne}$ and hydrogen-bonding stabilization (neutrophil elastase), (D) **Ac-DEVD-CL** (caspase-3), and (E) **MPCL-2** (M^{pro} SARS-CoV-2 protease).

through their differential APN expression, with a detection limit of just 562 cells. *In vivo*, **Ala-PD** enabled real-time visualization of tumors in mouse models, providing ultrahigh tumor-to-normal tissue contrast (>10^6) and prolonged emission suitable for extended surgical procedures. During 4T1 breast cancer resections, the probe's topical spray formulation allowed rapid tumor identification, precise margin delineation, and reliable detection of residual lesions, with post-resection imaging confirming complete clearance. Remarkably, **Ala-PD** also detected micrometastases in lung tissues invisible to the naked eye, with histological validation confirming its diagnostic accuracy. Overall, **Ala-PD** establishes chemiluminescent probes as a next-generation platform for surgical oncology, offering unmatched sensitivity, simplicity, and safety for real-time tumor mapping and metastasis detection in clinical settings.

Very recently, by integrating multi-enzyme logic control into probe design, Zhang *et al.* developed **LGP-CL**, a dual-protease-activated chemiluminescent probe designed for precise liver cancer imaging through simultaneous detection of aminopeptidase N (APN) and dipeptidyl peptidase IV (DPPIV) (Fig. 20B).[110] The probe integrates a "dual-lock–dual-key" activation mechanism, requiring sequential enzymatic cleavage by both APN and DPPIV to trigger light emission, thereby achieving exceptional diagnostic specificity and minimizing false-positive signals. Its molecular design consists of a cascaded LGP peptide substrate sequence, a self-immolative linker, and a phenoxy-dioxetane luminophore. Upon cleavage by APN and subsequent DPPIV processing, the probe generates a green emission with a 382-fold signal enhancement. Structural validation and docking analyses confirmed precise substrate recognition and demonstrated that the specific LGP sequence is essential for dual-enzyme activation, unlike its inactive isomer GPL-CL. **LGP-CL** exhibits outstanding analytical performance, with sub-nanogram detection limits for both enzymes, rapid activation kinetics, and remarkable stability under physiological conditions. In cellular assays, the probe showed excellent biocompatibility and distinguished liver cancer (HepG2) cells from normal and non-hepatic cell lines, producing strong chemiluminescent signals exclusively in dual-enzyme-active environments. In tumor-bearing mice, **LGP-CL** enabled real-time, inhibitor-sensitive tumor imaging with sustained emission and high contrast, allowing dynamic assessment of dual-protease activity *in vivo*. The system's logic gate character further highlights its potential as a prototype for molecular logic computation in biological diagnostics. Overall, **LGP-CL** represents a major advance in chemiluminescent probe engineering, providing a powerful platform for intelligent, enzyme-driven tumor diagnostics and paving the way for precision molecular imaging and smart therapeutic monitoring in clinical oncology.

Expanding the design principles to inflammation imaging, Huang *et al.* developed a new class of benzoazole-phenoxyl-dioxetane (BAPD) chemiluminescent probes that achieve unprecedented emission duration and brightness through intramolecular hydrogen-bonding stabilization, enabling real-time imaging of neutrophil activity in inflammatory diseases

(Fig. 20C).[111] The molecular design replaces traditional Schaap's dioxetane scaffolds with *ortho*-benzoazole substitutions on the phenoxyl ring, creating internal hydrogen bonds that stabilize the phenoxy anion intermediate formed during light emission. Hydrogen-bonding strength, confirmed by ^{1}H NMR downfield shifts and solvent titration experiments, was directly correlated with chemiluminescence longevity. The neutrophil elastase (NE)-specific probe **BTPD$_{Ne}$** integrates a AAPV peptide substrate that masks luminescence until enzymatic cleavage. This design achieved a detection limit of 1.3 U per L NE and exhibited exceptional selectivity over other proteases, supported by high quantum yields up to eightfold higher than those of classical dioxetane systems. *In vitro*, **BTPD$_{Ne}$** selectively illuminated activated neutrophils with over 30-fold signal enhancement compared to other immune cells and showed no cytotoxicity, confirming suitability for live-cell imaging. *In vivo*, the probe successfully visualized neutrophil infiltration in mouse peritonitis and psoriasis models, with sustained emission lasting over an hour and excellent correlation with histological neutrophil markers. The ability to non-invasively monitor inflammation dynamics and therapeutic responses, exemplified by cyclosporin A treatment response tracking, underscores the probe's biomedical utility. Overall, the BAPD platform introduces a mechanistically innovative and clinically promising chemiluminescence strategy for long-term immune imaging, establishing hydrogen-bond-stabilized dioxetanes as a new benchmark in probe design for inflammation diagnostics and drug evaluation.

In the context of apoptosis monitoring, Tannous *et al.* developed **Ac-DEVD-CL**, a super-sensitive chemiluminescent probe engineered for real-time detection of caspase-3 activity during apoptosis, representing a major advancement in apoptosis imaging technology (Fig. 20D).[112] The probe design is based on a caspase-3-specific peptide substrate Ac-DEVD. **Ac-DEVD-CL** exhibits exceptional analytical performance with a 5000-fold turn-on response, a 901-fold signal-to-noise ratio, and a detection limit of 5.45×10^{-4} μg mL^{-1}, outperforming traditional fluorescent probes by over two orders of magnitude. The probe demonstrates extraordinary selectivity for caspase-3 over other enzymes, with inhibitor studies confirming exclusive activation through the targeted apoptotic pathway. In live-cell experiments, **Ac-DEVD-CL** showed high biocompatibility and effectively monitored drug-induced apoptosis in 4T1 breast cancer cells, producing intense chemiluminescent signals upon cisplatin treatment that were abolished by caspase-3 inhibition. Real-time imaging enabled precise correlation between biochemical caspase activation and morphological features of apoptosis, establishing a direct mechanistic link between luminescent output and cell death progression. The probe's background-free emission, prolonged signal duration, and high stability make it ideally suited for continuous monitoring of therapeutic responses and high-throughput drug screening. Overall, **Ac-DEVD-CL** introduces a transformative platform for apoptosis imaging and quantitative enzyme analysis, offering unmatched sensitivity and specificity for biomedical research, anticancer drug evaluation, and potential clinical translation in apoptosis-based diagnostics.

Shifting focus to viral protease detection, Xia *et al.* reported the development of **MPCL-2**, an ultrasensitive chemiluminescent probe specifically designed for detecting SARS-CoV-2 main protease (M^{pro}) activity, marking the first use of chemiluminescence for viral protease imaging (Fig. 20E).[113] The probe's architecture integrates a modified peptide-based recognition substrate derived from known M^{pro} covalent inhibitors, a self-immolative *p*-aminobenzyl alcohol linker, and a Schaap's adamantylidene-dioxetane luminophore, enabling efficient enzymatic activation and strong photon emission. This design strategy, transforming covalent inhibitors into activity-based probes, ensures high substrate specificity and optimal enzyme accessibility, while avoiding covalent binding that could hinder turnover. MPCL-2 achieved an unprecedented detection limit of 0.11 nM with a wide linear range and rapid response time under 20 minutes, outperforming fluorescence and colorimetric assays in both sensitivity and signal-to-noise ratio. The probe displayed excellent selectivity against unrelated enzymes and ions, with complete inhibition by GC376 confirming specific recognition of M^{pro} activity. Molecular docking revealed strong binding interactions within the M^{pro} catalytic site, while enzymatic assays validated the predicted cleavage and luminescent product formation. In cell-based studies using SARS-CoV-2-infected TMPRSS2-VeroE6 cells, **MPCL-2** successfully distinguished infected from uninfected cells in real time, and its signal was attenuated by antiviral inhibitors, confirming biological specificity. Preliminary *ex vivo* lung tissue imaging demonstrated strong chemiluminescent signals in M^{pro}-positive regions, supporting future *in vivo* diagnostic potential. Overall, MPCL-2 establishes a powerful and versatile platform for real-time viral protease imaging, high-throughput antiviral drug screening, and longitudinal monitoring of viral activity, offering transformative applications in SARS-CoV-2 research, long COVID investigation, and emerging pathogen diagnostics.

4. Imaging fluorescent probes for kinases

4.1. Inhibitor-based fluorescent probes for cancer detection

Kinases play pivotal roles in cellular signaling, and their dysregulation is implicated in numerous diseases, particularly cancer.[114,115] This underscores the need for chemical tools to dissect kinase activity in living systems. Over the years, the development of activity-based chemical probes has emerged as a powerful approach for imaging kinases (reviewed by Usama *et al.*[116]). This chapter explores selected recent advances in nongenetic and nonpeptide kinase-targeted probes, focusing on design strategies, synthetic challenges, and applications in biomedical research. It draws insights from key studies involving ALK, Pim-1, PLK1, and EGFR kinases. These examples illustrate how the utility of such probes is influenced by factors such as: binding affinity and mode, selectivity, fluorescent properties, photostability, solubility and permeability, cellular uptake, cytotoxicity, biodistribution, background signal, and compatibility with various imaging modalities. In all these

cases, target specificity and affinity are achieved through pharmacophore-driven probe design. The imaging probes discussed incorporate known small-molecule kinase inhibitor scaffolds as warheads. A primary challenge in developing these probes lies in maintaining kinase binding potency and selectivity while integrating functional elements such as tags, linkers, or ligation handles.[116] Addressing selectivity is crucial – off-target interactions can obscure imaging results and lead to false-positive signals. To mitigate this, competitive inhibition assays using the parent drugs are commonly employed. Moreover, the often multi-step synthetic routes require a balance between structural precision and practical considerations such as scalability and reproducibility – factors that are especially important for clinical translation.[117]

Hou *et al.* developed two fluorescent probes targeting polo-like kinase 1 (PLK1), a protein involved in cell division and cancer progression.[118] The researchers incorporated a six-carbon alkyl linker between the fluorophore and the binding ligand to prevent steric hindrance while preserving the molecular recognition properties of SBE13, type II PLK1 inhibitor (Fig. 21). Coumarin was selected as the fluorophore for Probe **1** due to its high photostability, large Stokes shift, and ease of functionalization. However, the short absorption and emission wavelengths of Probe **1** limited its utility for deep tissue imaging in *in vivo* applications. To address this limitation, the researchers designed Probe **2** with a red-shifted emission profile by incorporating 3-cyano-4-phenyl-2(5*H*)-furanon as a strong electron-withdrawing group, resulting in dramatic bathochromic shifts suitable for *in vivo* tumor imaging in mouse xenograft models. Furthermore, a two-fold increase in Stokes shift contributed to an exceptional signal-to-background ratio, despite the probe being an "always-on" agent. In nocodazole-pretreated mice the tumor-to-liver fluorescence intensity ratio was 17.6 compared to 3.3 in probe-only treated mice. The molecular design process involved enzymatic docking experiments and molecular dynamics simulations. Both probes demonstrated excellent cell permeability and showed no detectable cytotoxicity, supporting their suitability for biological applications and potential in cancer diagnosis and precision therapeutics. The work highlights the importance of rational fluorophore design. Introducing a single substituent can dramatically alter fluorescence properties, enhancing the probe's utility for specific applications, such as *in vivo* imaging, while also reducing background fluorescence, a common limitation in many affinity-based imaging agents. Another red-emitting agent was presented by Guo *et al.*[119] Authors developed **NB-BF**, a probe selective for Pim-1 kinase, which is overexpressed in various cancer types, and acts as an oncogenic serine/threonine kinase that drives cell survival, proliferation, and therapy resistance by phosphorylating regulators of apoptosis, cell-cycle progression, and transcription. The probe's architecture integrates a Pim-1 inhibitor, 5-bromobenzofuran-2-carboxylic acid (BF), linked to a red-emitting Nile Blue (NB) fluorophore *via* a hexanediamine spacer. **NB-BF** is an "on-off" (activatable/responsive) probe that utilizes a photoinduced electron transfer mechanism, where fluorescence is quenched in the unbound state and turned on upon kinase binding. Optimal spatial arrangement between the fluorophore and quencher enables efficient PET quenching while preserving the kinase inhibitory activity after fluorophore conjugation. The probe's functionality was validated through spectroscopic characterization, showing favorable properties including pH stability, photostability, good water solubility, and minimal cytotoxicity. Target specificity was confirmed *via* genetic silencing. Biomedical studies demonstrated the probe's ability to selectively distinguish Pim-1-overexpressing cancer cells from normal cells, enabling real-time imaging in live cells and mouse tumor xenograft models. These features highlight its potential for early cancer diagnosis and fluorescence-guided surgery. These works emphasizes the advantages of red-emitting or near-infrared fluorescent probes, whose long-wavelength emission reduces background autofluorescence, photon scattering, and photodamage, while enabling deeper tissue penetration.[35,120,121] Additionally, the signal enhancement enabled by the "on-off" activation mechanism contributes to a high signal-to-noise ratio. Those features make such probes suitable for high contrast *in vivo* imaging.

The next example of a kinase targeted by a fluorescent probe is **VEGFR2**, a key regulator of angiogenesis that is highly expressed in endothelial cells and often upregulated in solid

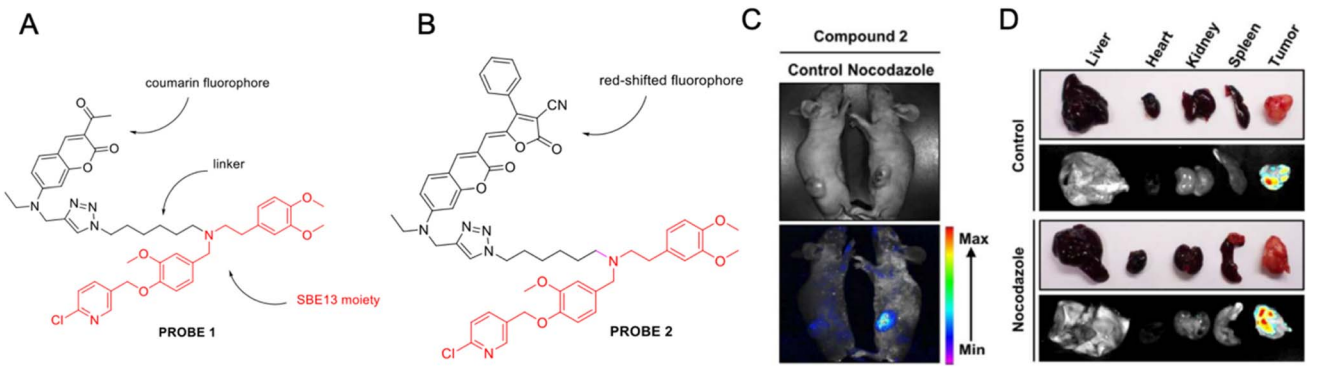

Fig. 21 SBE13-derived PLK1 probes. (A) Chemical structure of Probe **1**. (B) Chemical structure of Probe **2**. (C) White light (top) and fluorescence (bottom) images of HCT116-xenograft tumor bearing mice injected with Probe **2**, pretreated with DMSO (left) and nocodazole (right). (D) Dissected organs and tumors and the corresponding fluorescent images form probe 2-injected tumor-bearing mice. Adapted with permission from ref. 118 Copyright 2017, American Chemical Society.

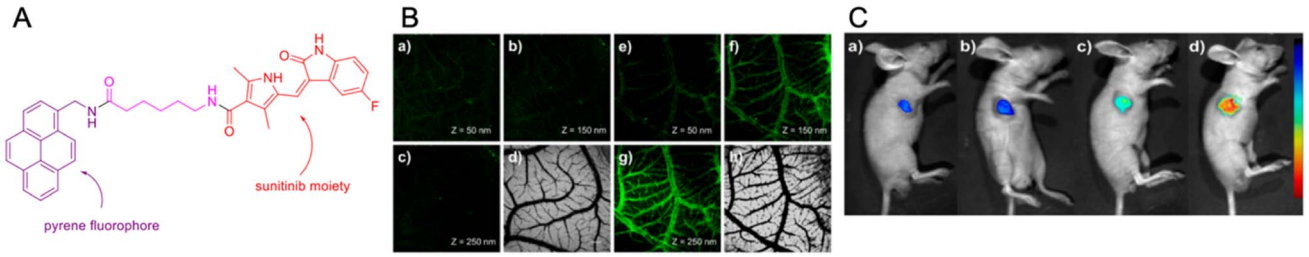

Fig. 22 Sunitinib-based VEGFR2 probe. (A) Chemical structure of **SP1**. (B) Fluorescence images of the chick embryo using **SP1** in 9-day-old fertilized eggs. (a–d) 15 μM **SP1**; (e–h) 20 μM **SP1**. Images were acquired using 458 nm excitation after incubation with **SP1** for 24 h at 37 °C; scale bar = 300 μm. (C) *In vivo* fluorescence imaging of SP1 in a HT-29 tumor-bearing mouse model *via* SP1 injection: (a) 0.1 mM, 100 μL; (b) 0.5 mM, 100 μL; (c) 1 mM, 100 μL; (d) 2 mM, 100 μL. Adapted with permission from ref. 124 Copyright, 2018 American Chemical Society.

tumors, including colorectal, breast, lung, and renal cancers.[122] Dysregulated VEGFR2 signaling promotes tumor vascularization, growth, and metastasis, making it an important biomarker and therapeutic target in oncology.[123] In 2019 Jiao *et al.* developed SP1, a conformationally induced "off-on" fluorescent chemosensor (Fig. 22).[124] The probe integrates sunitinib, a VEGFR2 inhibitor, with a pyrene fluorophore *via* a hexamethylenediamine linker, enabling selective detection of VEGFR2-overexpressing cancer cells through a PET quenching mechanism. Due to pyrene's π–π stacking interactions, **SP1** dimerizes in its free state, effectively quenching fluorescence. Upon binding to RTKs, the dimer is disrupted, restoring fluorescence. The study also investigated the effect of solvent composition on fluorescence. **SP1**'s fluorescence was quenched in aqueous media, while the highest signal enhancement was observed in a 1 : 9 DMSO/H_2O mixture. This medium was identified as optimal for achieving the lowest background signal in imaging experiments. The probe was successfully applied *in vivo* tumor imaging in mouse xenograft models. The use of the pyrene fluorophore highlights the diversity of probe design strategies that leverage intermolecular and intramolecular interactions. The work also emphasizes the importance of solvent optimization for maximizing signal-to-noise ratios in fluorescence imaging.

One of the most common protein targets in cancer therapy and diagnostics are EGFR (epidermal growth factor receptor, also known as HER1) and HER2 (human epidermal growth factor receptor 2).[125,126] These receptor tyrosine kinases play

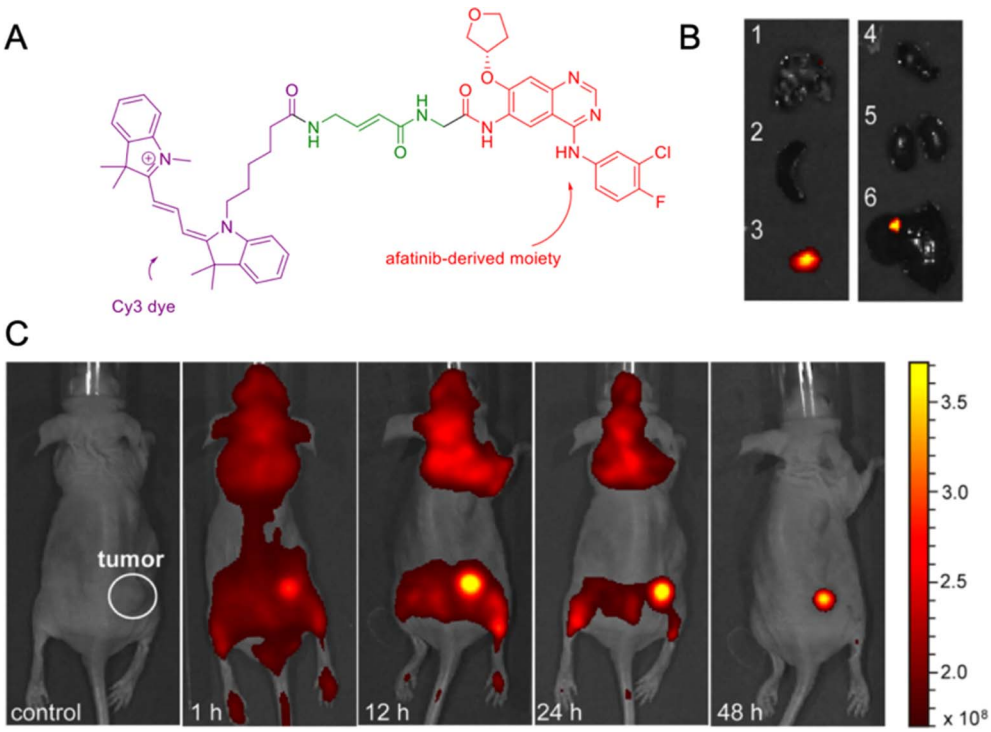

Fig. 23 Structure of afatinib-based HER1/HER2 chemical probe. (A) Chemical structure of **Cy3-AFTN**. (B) The *ex vivo* optical images of organs ((1) lung; (2) spleen; (3) tumor; (4) heart; (5) kidney; (6) liver) of the A549 tumor-bearing mice sacrificed at 48 h after administration. (C) Fluorescence imaging obtained for **Cy3-AFTN**-treated A549-bearing mice for up to 48 h (λ_{ex} 540 ± 10 nm and λ_{em} 560 ± 20 nm). Adapted with permission from ref. 128 Copyright 2018, American Chemical Society.

central roles in driving tumor growth, survival, and proliferation, and their aberrant activation, through overexpression or mutation, is strongly linked to poor clinical outcomes and therapy resistance.[125,126] EGFR alterations are particularly prevalent in non-small cell lung cancer (NSCLC), while HER2 is frequently overexpressed in breast and gastric cancers, making both receptors critical targets for precision oncology. To date, multiple small-molecule inhibitors have been developed targeting these proteins, with several examples, such as erlotinib, gefitinib (EGFR), and lapatinib, afatinib (HER2/EGFR dual inhibitors), successfully translated into clinical use for the treatment of various cancers.[127] Liu *et al.* developed reversible HER1/HER2 dual-targeting "always-on" NIR fluorescent probes **Cy3-AFTN** and **Cy5-AFTN**, derived from the irreversible kinase inhibitor afatinib (Fig. 23).[128] A key challenge was converting afatinib's irreversible binding mechanism, cysteine-mediated thia-Michael addition, into a reversible, noncovalent interaction without compromising binding affinity. This was achieved by inserting a glycine spacer to block nucleophilic attack. The resulting probes selectively illuminated HER1/HER2-overexpressing cells under confocal microscopy, with fluorescence intensity correlating to receptor expression levels. Competitive assays with afatinib confirmed the reversibility of the interaction. In xenograft mouse models, **Cy3-AFTN** demonstrated high tumor-to-background ratios, with signal accumulation peaking between 12 and 48 hours post-injection. *Ex vivo* imaging further confirmed selective accumulation in tumor tissue over normal organs. This research highlights how modifications to a pharmacophore scaffold can alter the binding mode and expand the potential applications of chemical agents in drug discovery. The authors suggest that the reversible nature of these probes could enable their use in competitive displacement assays for cell-based fluorometric screening, helping identify new dual EGFR/HER2 inhibitors.

Another example of chemical probes targeting HER1/HER kinases was described by Li *et al.* who developed a series of NIR fluorescent probes, **YQ-H-01** to **YQ-H-07**.[129] These probes were designed by conjugating the HER1/HER2 inhibitor lapatinib with a bulky, hydrophilic cyanine dye MPA (Fig. 24). The authors explored various linkers, including alkyl, PEG and glycine chains, in order to minimize steric hindrance and modulate hydrophobicity. All probes demonstrated superior retention times and target affinity, outperforming indocyanine green (ICG) in mouse models. Probes with alkyl chain linkers (**YQ-H-02** and **YQ-H-03**) accumulated in the liver and lungs, likely due to increased hydrophobicity and slower clearance from normal tissues. In contrast, PEG-based linkers (**YQ-H-04** and **YQ-H-05**) reduced off-target accumulation but at the cost of diminished tumor signal. Glycine-based linkers in **YQ-H-06** and **YQ-H-07** provided a favorable balance, enabling sustained tumor accumulation (up to 48 hours) while minimizing off-target retention. **YQ-H-06**, in particular, showed excellent performance, with favorable pH tolerance, biosafety profile, photostability, and contrast with a peak tumor-to-normal tissue ratio of 2.7, highlighting its potential for clinical translation, especially in cancer diagnosis and fluorescence-guided surgery. This study underscores the critical role of linker design in optimizing probe performance, particularly in terms of metabolism, biodistribution, and retention time.

Lapatinib was also used as a scaffold by Xie *et al.* who developed **LP-S**, a novel NIR fluorescent probe targeting EGFR/HER2 kinases for metastatic lymph node imaging in oral squamous cell carcinoma (OSCC) (Fig. 25).[130] The binding affinity of lapatinib was retained after conjugation with the

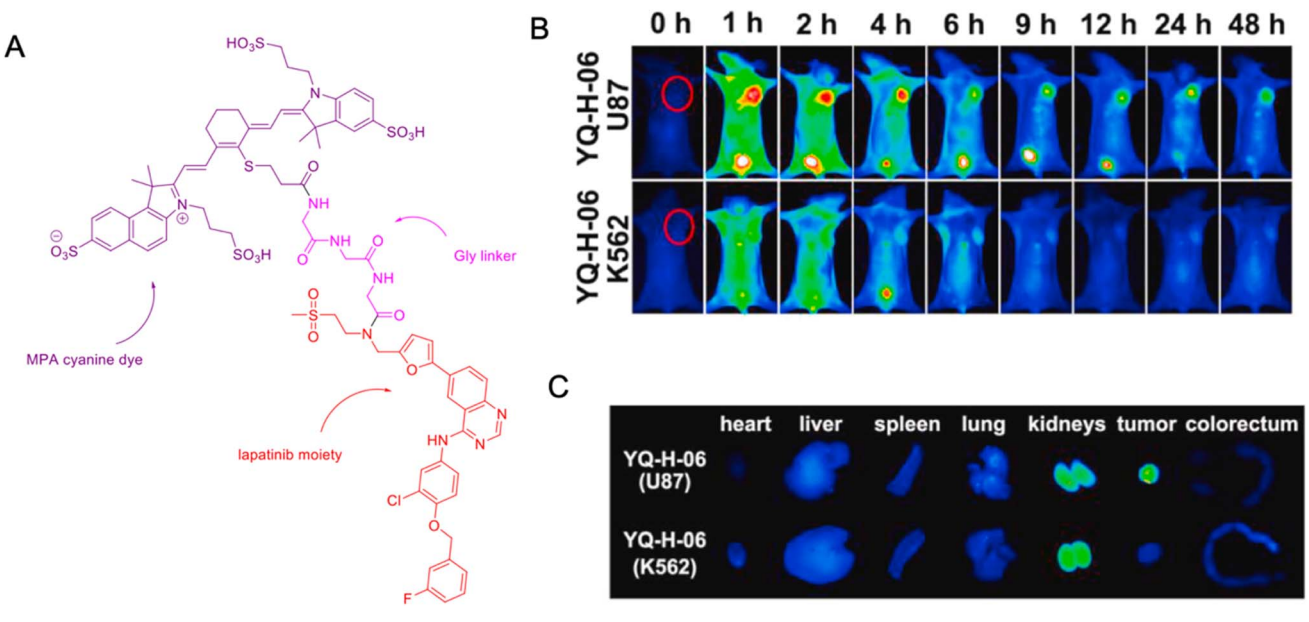

Fig. 24 Lapatinib-based HER1/HER2 chemical probe. (A) Chemical structure of **YQ-H-06** probe. (B) *In vivo* imaging of HER1/HER2 in U87 and K562 tumor-bearing mice with **YQ-H-06**. (C) Fluorescence imaging of the tumors and main organs, which were taken from U87 and K562 tumor-bearing mice at 10 h after injection. Adapted with permission from ref. 129 Copyright 2022, Elsevier B.V.

bulky S0456 fluorophore *via* a semi-rigid hydroxyphenyl-propionic acid (HPPA) linker. The resulting probe exhibited a 20-fold higher quantum yield, reduced nonspecific tissue diffusion due to increased molecular weight, and enhanced photostability under prolonged irradiation compared to indocyanine green (ICG). **LP-S** also showed lower cytotoxicity than lapatinib, and the inclusion of the HPPA linker increased fluorescence intensity compared to S0456. **LP-S** selectively accumulated in EGFR-overexpressing OSCC cell lines (CAL27, HSC3) *versus* low-EGFR-expressing SCC9 cells, with time-dependent cytoplasmic internalization. Its binding affinity was confirmed *via* molecular docking (-8.56 kcal mol^{-1} for EGFR, compared to -9.2 kcal mol^{-1} for native lapatinib). In mouse models, **LP-S** enabled high-contrast visualization of lymphatic drainage pathways (tumor-to-normal signal ratio of 3.6 : 1) within 30 minutes post-injection and demonstrated sustained retention in metastatic lymph nodes (T-LNs) compared to normal lymph nodes (N-LNs). Moreover, **LP-S** guided the resection of metastatic lymph nodes in OSCC with significantly reduced false-positive rates compared to ICG, thereby enhancing surgical precision. This study illustrates how molecular weight and the electronic properties of linkers can influence the clinical utility of imaging probes.

4.2. The HX series: fluorescent probes for functional imaging of EGFR and ALK kinase activity

A notable contribution to the field of fluorescent chemical probes for kinase imaging was made by the Li laboratory. Among their efforts, the HX series stands out as a collection of small-molecule probes specifically designed to image kinase activity in non-small cell lung cancer specimens (Fig. 26). This innovative toolbox comprises six structurally distinct probes, **HX103**, **HX03**, **HX04**, **HX05**, **HX101**, **HX16**, and **HX106**, each optimized for selective labeling of kinase targets and compatible with imaging in *ex vivo* tumor samples.[131–135]

HX103 represents a pioneering fluorogenic probe specifically designed to predict treatment response in NSCLC patients harboring EGFR-activating mutations.[132] Its design strategy centers on incorporating an environment-sensitive fluorogenic sulfonamide-benzoxadiazole moiety into the pharmacophore of gefitinib, an established EGFR tyrosine kinase inhibitor (Fig. 26A). The rational design approach involved structure–activity relationship (SAR) analysis based on X-ray crystallographic data, as well as molecular docking studies, ensuring that the fluorescent modification would not compromise the potency of the original EGFR-TKI scaffold. **HX103** demonstrated the ability to quantify EGFR activation in living cells through flow cytometry analysis. The probe exhibited specific accumulation in cells with EGFR-activating mutations, enabling precise discrimination between mutant and wild-type EGFR expression using a fluorescence-activated cell sorting (FACS) assay. Clinical validation studies revealed that **HX103** labeling strongly correlated with treatment response to EGFR-TKIs, with patients exhibiting high probe labeling demonstrating significantly better objective response rates compared to traditional mutation-based selection methods. The probe's ability to detect functional EGFR activation provides clinicians with valuable information for treatment stratification that goes beyond conventional genomic sequencing approaches.

The "clickable" probe series **HX03**, **HX04**, and **HX05** represents an innovative application of bioorthogonal chemistry to EGFR activity visualization (Fig. 26B). These probes are based on EGFR-TKI scaffolds, **HX03** derived from canertinib, **HX04** from dacomitinib, and **HX05** from afatinib.[131] The design strategy incorporated alkyne functional groups into the TKI structures, enabling subsequent copper-catalyzed azide–alkyne cycloaddition (CuAAC) reactions for fluorescent labeling. The synthesis focused on maintaining the enamide moiety crucial for covalent inhibitory potency while introducing the alkyne functionality required for click chemistry applications. The

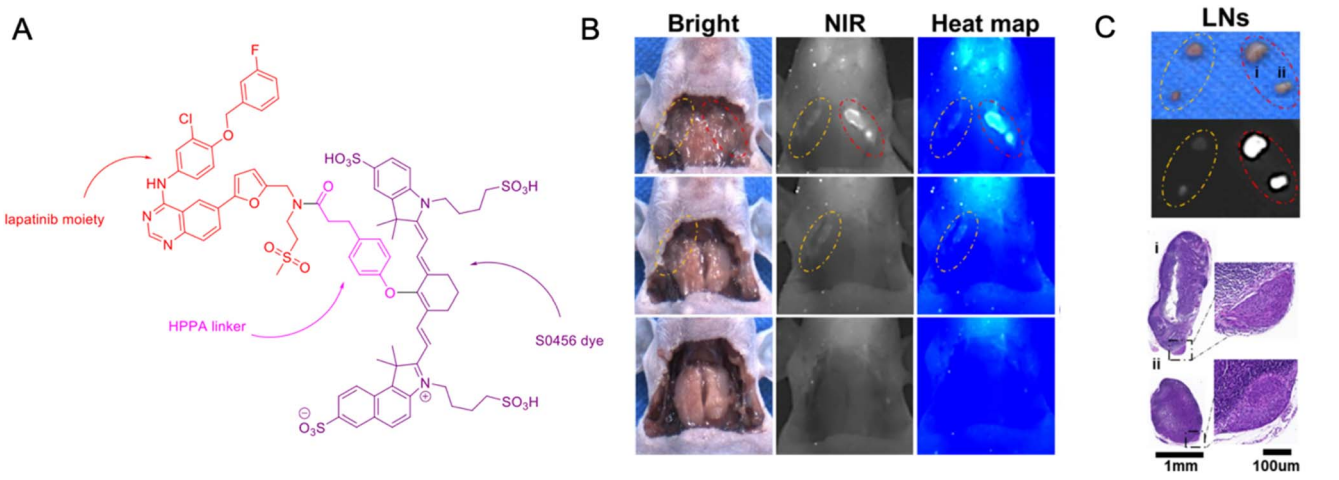

Fig. 25 Lapatinib-based EGFR activity-based probe. (A) Chemical structure of **LP-S** probe. (B) Fluorescence-guided surgery for the excision of cervical LNs after 24 h injection, including highlighting (red circle) and contralateral (yellow circle) LNs. (C) Fluorescence images of excised cervical LNs after 24 h injection of **LP-S**. H&E staining of highlighted LNs confirmed metastasis. Adapted with permission from ref. 130 Copyright 2023, The Authors. Published by Springer Nature.

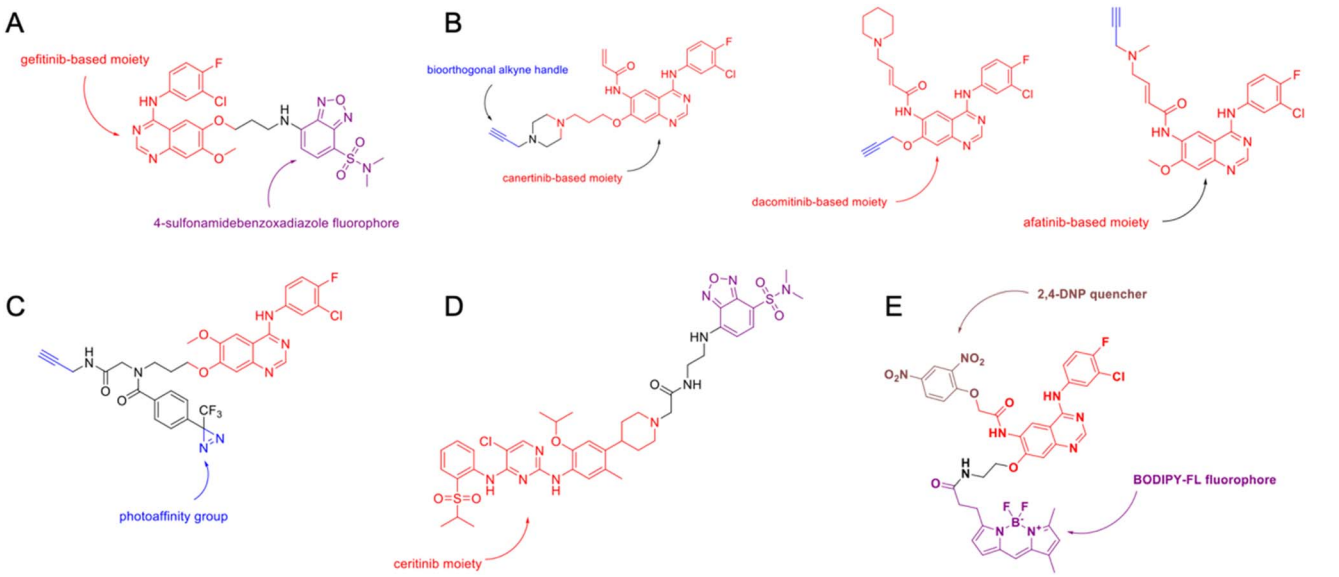

Fig. 26 Chemical structures of ABPs from HX series. (A) **HX103** probe. (B) Clickable probes **HX03**, **HX04**, **HX05**. (C) Photoaffinity probe **HX101**. (D) **HX16** probe. (E) Quenched **HX106**.

biomedical applications of these clickable probes demonstrate exceptional versatility in cellular imaging and tissue analysis. **HX03** showed particularly high potency, with IC_{50} values of 0.2 μM in **HCC827** cells and 3.1 μM in **H1975** cells, both harboring EGFR primary mutations. The probe enabled concentration-dependent labeling of EGFR kinase with high sensitivity, allowing specific visualization of EGFR activity in native cellular contexts at submicromolar concentrations. Tissue slice experiments revealed that the clickable probe could effectively distinguish between tumor and adjacent normal tissues, as well as between mutant-positive and mutant-negative tissues. This capability positions the clickable probe series as valuable diagnostic tools for providing information on EGFR mutations in clinical specimens, which offers an opportunity to improve both diagnosis and prediction of therapeutic responses to EGFR-TKI therapy.

HX101 represents a sophisticated two-step photoaffinity probe (Fig. 26C).[133] Its design incorporates diazirine as a photoactivatable group, enabling covalent attachment upon UV irradiation, combined with an alkyne handle for subsequent fluorescent labeling through click chemistry. This dual-functionality design allows for both target engagement studies and fluorescence-based detection, making **HX101** a versatile tool for both research and diagnostic applications. The probe demonstrates the capability to target active EGFR in living cells and tissue slices, with strong fluorescence signals observed in EGFR-positive cancer cells upon UV activation and subsequent click labeling. **HX101** successfully identified potential off-targets, including ERBB2, TRIM28, RTN3, RTN4, APOB, HNRNPU, PTBP1, EHD1, and HEXB, based on photoaffinity-based protein profiling. The probe was successfully used for imaging EGFR at the single-molecule scale *via* stochastic optical reconstruction microscopy (STORM). Clinical tissue studies revealed that **HX101** could effectively discriminate between tumor tissues harboring EGFR mutations and adjacent normal tissues in NSCLC patients, demonstrating strong fluorescence signals in EGFR-positive regions while showing minimal labeling in normal tissue areas. This study highlights how thoughtful probe design can broaden the utility of imaging agents across different modalities, including quantitative MS-based proteomics, FACS, confocal microscopy, and super-resolution techniques like STORM.

HX16 represents a unique departure from EGFR-focused probes, targeting anaplastic lymphoma kinase activity in NSCLC.[135] Similar to **HX103**, the probe design incorporates an environment-sensitive fluorophore into the ceritinib scaffold, creating a probe that exhibits dramatically different fluorescence properties depending on its binding environment (Fig. 26D). The synthetic strategy for **HX16** involved SAR analysis based on crystallographic data of ceritinib–ALK complexes. **HX16**'s biomedical applications demonstrate remarkable specificity for ALK-positive cancer cells. Flow cytometry analysis revealed that **HX16** accumulation in cancer cells strongly correlates with ALK expression levels, with the highest labeling observed in SU-DHL-1 cells (ALK-NPM fusion), followed by H2228 and H3122 cells (both harboring ALK-EML4 fusions). The probe successfully inhibited ALK phosphorylation and downstream signaling pathways in ALK-positive cancer cells. Clinical validation studies demonstrated that **HX16** could effectively distinguish ALK-positive tumor cells from wild-type controls in mouse models and biopsy slices from a NSCLC patient with ALK-EML4 rearrangement, providing a functional readout of ALK activity that complements traditional immunohistochemical approaches. This environment-sensitive detection capability makes **HX16** particularly valuable for identifying patients who may benefit from ALK inhibitor therapies.

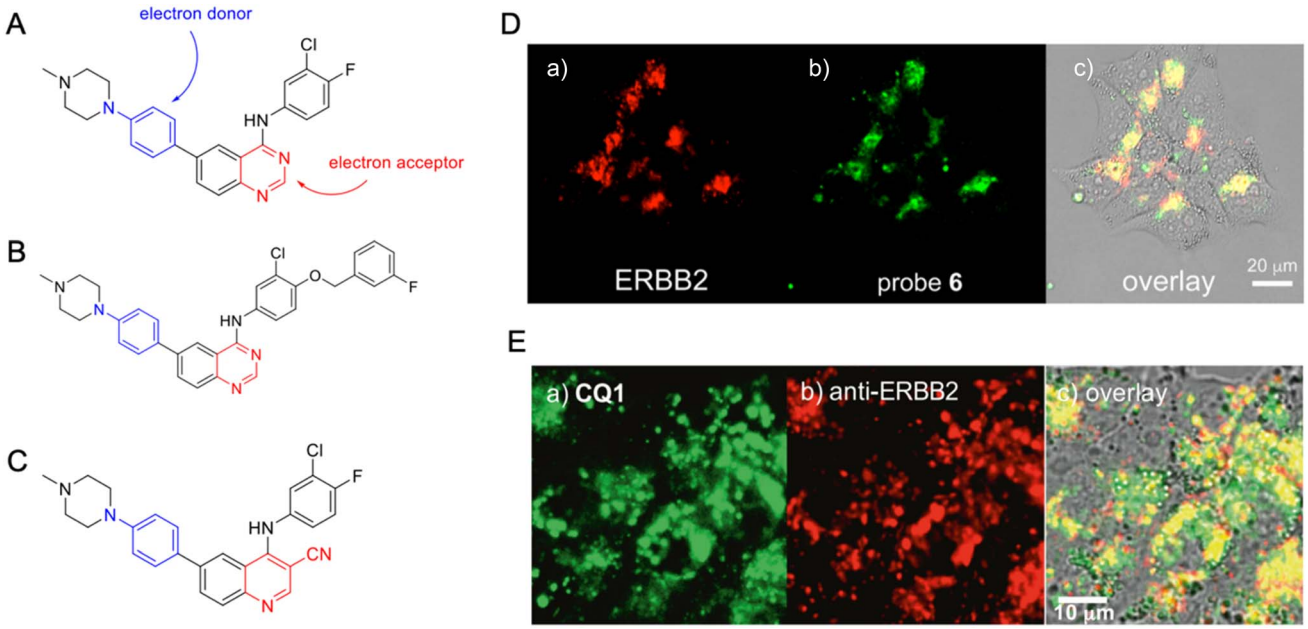

Fig. 27 A push–pull π-electron system of kinase probes. (A) Quinazoline-based probe **QA1**. (B) **QA2**. (C) Cyanoquinoline-based probe **CQ1**. (D) Costaining of BT474 cells with (a) ERBB2-directed antibody and (b) **QA2**; (c) overlay demonstrates a high degree of overlap; 2 μM, $\lambda_{ex} = 405$ nm, $\lambda_{em} = 450–550$ nm. Adapted with permission from ref. 137 Copyright 2016, American Chemical Society. (E) Co-staining of BT474 cells with (a) **CQ1** and (b) anti-ERBB2; (c) overlay of the two channels shows a high degree of overlap; $\lambda_{ex} = 405$ nm, $\lambda_{em} = 500–600$ nm. Adapted with permission from ref. 138 Copyright 2017, Elsevier Ltd.

HX106 represents the most recent advancement in the HX probe series, employing a quenched fluorescence mechanism for rapid and accurate assessment of EGFR-activating mutations (Fig. 26E).[134] The probe design incorporates DNP and BODIPY-FL as a quencher–fluorophore pair that becomes activated upon specific binding to mutant EGFR kinases. **HX106** improves upon **HX103**, which is based on a noncovalent TKI and thus requires repetitive washing to achieve a high signal-to-noise ratio. In contrast, **HX106** binds irreversibly, enabling "no-wash" real-time detection and significantly streamlining the diagnostic workflow. The probe shows rapid kinetics, with fluorescence saturation achieved within 2 hours and a detection limit of 13 nM for EGFR kinase labeling. Flow cytometry analysis revealed excellent correlation between **HX106** labeling and EGFR expression levels across multiple cancer cell lines. Most importantly, clinical validation studies using surgically resected NSCLC samples demonstrated that **HX106** could accurately identify tumors harboring EGFR-activating mutations with 94% accuracy. The probe showed strong positive correlation with EGFR mutant protein expression as determined by immunohistochemistry, with Pearson correlation values exceeding 0.94. This high accuracy, combined with its rapid detection capability, positions **HX106** as a promising tool for intraoperative or rapid diagnostic applications in clinical oncology.

The HX probe series represents a paradigm shift in kinase activity detection for NSCLC diagnosis and treatment planning. Each probe was designed with different mechanistic approaches including clickable chemistry, photoaffinity labeling, environment-sensitive fluorescence, and quenched fluorescence detection. These probes collectively address critical challenges in precision oncology by enabling real-time visualization of kinase activity, particularly targeting EGFR mutations and ALK-EML4 fusion. The innovative design strategies demonstrate the versatility of chemical probe approaches in detecting activating mutations, bearing therefore potential for predicting treatment responses to tyrosine kinase inhibitors. The series' ability to provide real-time, functional information about kinase activity offers significant advantages over traditional genomic sequencing approaches, potentially improving treatment selection and patient outcomes in NSCLC. As precision medicine continues to evolve, these chemical tools provide essential capabilities for translating molecular insights into clinical practice, offering hope for more effective and personalized cancer treatment strategies.

The examples above illustrate probes developed by conjugating a small-molecule kinase inhibitor scaffold with a fluorescent dye. However, modifying the pharmacophore structure itself can induce intrinsic fluorescent properties. Continuing on their previous work, Lee *et al.* developed such fluorescent inhibitors by introducing an electron-donating moiety at the 6-position of the electron-withdrawing quinazoline core, a scaffold common to EGFR/ERBB-targeted inhibitors (Fig. 27).[136,137] This modification extends conjugation and creates a push–pull system with strong intramolecular charge transfer (ICT) character. The excited state of the probe is stabilized in polar environments, and fluorescence is activated through conformational restriction upon binding to the more hydrophobic kinase pocket. Further incorporation of an *N*-methylpiperazine moiety enhanced the water solubility, giving probes **QA1** and **QA2**. The optimized compounds demonstrated

nanomolar affinity, comparable to clinically approved inhibitors, and successfully distinguished HER2-overexpressing cells from those with low HER2 levels in live-cell assays. Moreover, FACS combined with western blot analysis using **QA1** enabled monitoring of HER2 activation dynamics in BT474 cells, offering complementary information to traditional immunohistochemical assays. To increase the utility of quinoline probes **QA1** and **QA2** in drug screening and studies on available pharmacophores, Lee *et al.* introduced an electron withdrawing nitrile group.[138] A resulting red-shift in fluorescence emission of cyanoquinoline probe **CQ1** mitigated the spectra overlap with known HER2 inhibitors, allowing for selective HER2 imaging in cells treated with pharmacophores. Based on assays with type-I and type-II inhibitors, **CQ1** is useful in imaging HER2 internalization and studying binding mode of pharmacophores.

4.3. Environment-sensitive and photocaged probes for imaging of kinases

Another notable example of fluorescent inhibitors are probes for lymphocyte-specific protein tyrosine kinase (LCK), developed by Fleming *et al.* (Fig. 28).[139] The probes were developed by incorporating a prodan-derived solvatochromic fluorophore into a pyrazolo[3,4-*d*]pyrimidine heterocyclic scaffold, which is commonly found in ATP-competitive kinase inhibitors. The fluorescent moiety was introduced at the 3-position of the heterocycle, allowing it to extend into the hydrophobic back pocket of the kinase. The authors synthesized six different prodan derivatives to explore various linker-fluorophore conjugation strategies (alkane *vs.* alkyne linkers) and to assess the importance of the carbonyl group in the prodan core. The researchers thoroughly evaluated the photophysical properties of all compounds in solvents of varying polarity, measuring absorption maxima, emission maxima, fluorescence quantum yields, and lifetimes. Compounds #**3** and #**4** were selected for further evaluation due to their favorable fluorescent behavior in aqueous solution. A kinome-wide screen against 65 kinases was conducted to assess selectivity. While compound #**3** exhibited little kinase inhibition, compound #**4** showed strong inhibitory activity toward Aurora-A, Blk, and LCK, with the strongest effect against LCK (IC_{50} = 124 nM). Fluorescence titration experiments with compound #**4** demonstrated a dramatic 400-fold increase in emission intensity upon binding to LCK, accompanied by a blue shift in emission wavelength and a 1 : 1 binding stoichiometry. These changes make compound #**4** an excellent reporter of LCK binding, as the fluorescence response is diagnostic of the interaction. The developed fluorescent kinase inhibitor has several important applications. It enables to monitor LCK activity in LCK(+) Jurkat cells. The solvatochromic behavior allows distinction between free and target-bound inhibitor molecules. Microscopy and flow cytometry experiments confirmed that fluorescence intensity correlates with intracellular LCK levels. The probe also demonstrated compatibility with two-photon microscopy in the HTB-177 human lung cancer cell line, suggesting potential for deep-tissue imaging.

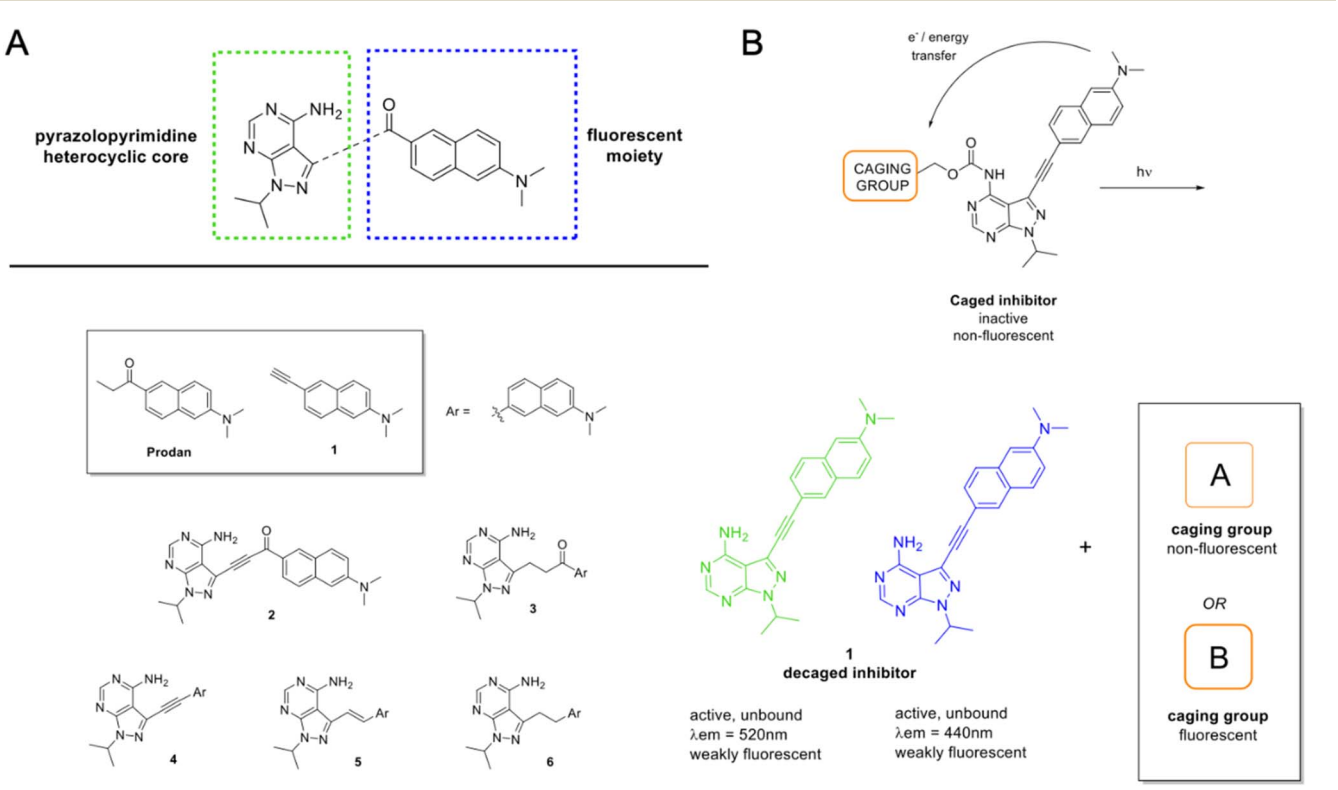

Fig. 28 LCK-specific chemical probes. (A) Potential prodan-derived pyrazolopyrimidine kinase inhibitors. (B) Working principle of proposed caged inhibitors. Biologically active LCK inhibitor **1** is released by means of light, and only shows strong emission upon binding to LCK enzyme. Different caging groups are incorporated, classifying them as (A) non-fluorescent or (B) fluorescent.

Co-localization experiments with LCK-specific antibodies revealed accumulation of the probe in regions consistent with LCK localization.

Building upon this work, the group later developed novel all-photonic probes for LCK.[140] A major challenge in kinase research is achieving precise spatiotemporal control over kinase activity while simultaneously monitoring therapeutic efficacy in real time. Traditional kinase inhibitors suffer from poor selectivity and lack control over when and where activation occurs, limiting their utility as both research tools and therapeutic agents. To overcome these limitations, the researchers developed a dual-function system in which light serves as both an activation trigger and a fluorescence-based reporter. Their design involved modifying a previously characterized solvatochromic LCK inhibitor #**4** by incorporating photolabile caging groups *via* a carbamate linkage. These caging groups quenched fluorescence through electron and/or energy transfer mechanisms, without compromising the inhibitor's selectivity. The ideal caging groups had to be biocompatible, responsive to non-damaging wavelengths, and capable of releasing non-toxic byproducts upon photolysis. Coumarin-derived and BODIPY-derived caging groups were identified as promising candidates, along with traditional *o*-nitrobenzyl groups for comparison. The incorporation of fluorescent *versus* non-fluorescent caging groups introduced distinct design considerations: non-fluorescent groups acted as spectroscopically silent quenchers, while fluorescent caging groups provided additional reporting capabilities. The latter were quenched in their caged form and regained fluorescence upon photolytic release. Photophysical analyses revealed important structure–activity relationships. Caging groups such as *o*-nitrobenzyl had minimal effects on the inhibitor's inherent fluorescence, while fluorescent caging groups efficiently quenched emission. Electrochemical studies confirmed that photoinduced electron transfer was thermodynamically favorable in the coumarin and BODIPY systems. Decaging kinetics varied across the caging groups, with some reactions deviating from simple mono-exponential behavior due to secondary photochemical processes. Even small changes in structure affected decaging properties. Introduction of a methyl group at the benzylic position of *o*-nitrobenzyl group in #**4b** significantly improved decaging efficiency and thermal stability. However, probes #**4a** and #**4b** showed photodegradation under 365 nm light, underscoring the need for caging groups that respond to longer excitation wavelengths. This criterion was met by probes #**3c**–**3e**, which were chosen for further biological studies. Biological evaluation confirmed that the photochemical designs translated successfully into functional cellular tools. Fluorescence titration with purified LCK validated the release-and-report mechanism: the caged inhibitor #**3e** showed no specific binding before photolysis, but fluorescence dramatically increased upon light activation, signaling release and binding to LCK. Displacement with the known inhibitor TC-S7003 confirmed binding specificity. Importantly, the caged inhibitors lost all LCK activity but retained efficient cellular uptake in peripheral blood mononuclear cells (PBMCs), confirming that the placement of caging groups effectively masked activity without hindering cell permeability. Light-mediated LCK inhibition by probes #**3c** and #**3d** in natural killer cells was successfully demonstrated, marking a significant advance in chemical probe technology. Subcellular localization patterns varied across the caging designs: coumarin-derived #**3c** and #**3d** showed non-specific distribution, while BODIPY-based #**3e** preferentially localized to membranes. These differences may be leveraged for compartment-specific inhibition.

4.4. Kinase probes compatible with mass spectrometry

Mass-spectrometry-compatible kinase probes couple a recognition element for the ATP site (or adjacent allosteric pockets) with a reporter workflow that survives cell biology and sample preparation, enabling unbiased, proteome-wide readouts. Two broad classes dominate: (i) affinity/photoaffinity probes that capture transient binders upon irradiation and (ii) activity-based covalent probes that react with conserved catalytic residues. Both these types are outfitted with minimal bioorthogonal handles (*e.g.*, alkyne or *trans*-cyclooctene) for enrichment and LC-MS/MS identification. Key design priorities include cellular permeability, chemical stability, selective engagement, and orthogonal conjugation strategies (CuAAC or IEDDA) that avoid artifacts and maximize recovery. When paired with quantitative proteomics (label-free, SILAC, or isobaric tags), these probes support target-engagement and occupancy measurements, dose–response profiling, and systematic off-target deconvolution in live cells or lysates. Therefore, such probes enable mechanism-of-action studies, guide scaffold optimization, and surface pharmacodynamic biomarkers that inform therapeutic window and patient stratification.

In one of such studies, Korovesis *et al.* developed and evaluated photoaffinity probes based on the imidazopyrazine scaffold, a core structure present in several FDA-approved kinase inhibitors and drug candidates.[141] The probes were designed with a minimalist strategy using an alkyne-diazirine module for photoaffinity labeling. Three probe variants were created: one derived from KIRA6 targeting the IRE1α kinase domain, one from acalabrutinib as a BTK probe, and one from linsitinib as an IGF-1R probe. Validation experiments demonstrated concentration-dependent, UV-dependent labeling that could be competed with parent inhibitors and produced cell-line-specific labeling patterns. Chemical proteomics in A431 lysates confirmed specificity using enrichment thresholds, competition with parent inhibitors, and TAMRA-biotin-azide tagging followed by LC-MS/MS. The KIRA6 probe was the most selective, which was confirmed *via* molecular dynamics simulations. The biomedical applications of these probes are broad. They enable proteome-wide selectivity profiling, uncover non-kinase targets, and provide structure–activity insights for scaffold optimization. This helps in designing more selective inhibitors, predicting off-target profiles, and balancing efficacy with safety. Clinically, mapping off-targets aids in optimizing therapeutic windows, predicting side effects, and identifying cases where polypharmacology may be beneficial. The identified proteins can serve as biomarkers for drug engagement, resistance mechanisms, or patient stratification.

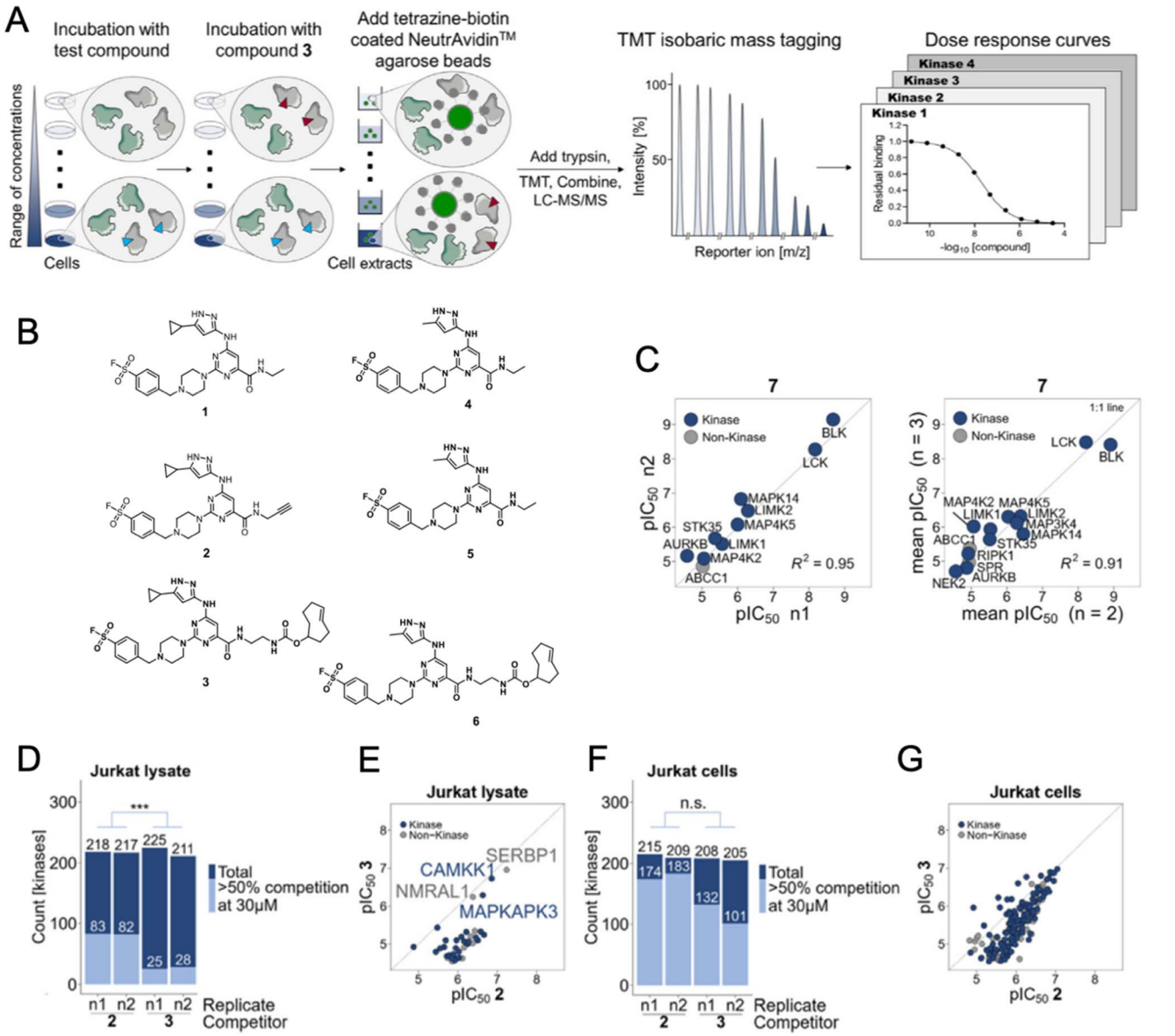

Fig. 29 Characterization of probes using chemoproteomic selectivity profiling with kinobeads. (A) Schematic of the kinobeads workflow: cell extracts or intact cells are treated with a compound (red triangle) or vehicle control. Compound-bound kinases are unable to bind to kinobeads coated with broad-spectrum ATP-competitive inhibitors (yellow circles). After washing, bead-bound proteins are eluted, digested with trypsin/LysC, TMT-labeled, combined, and analyzed by MS. Decreased peptide signal intensity relative to control reflects compound competition for the target. (B) Structures of sulfonyl fluoride-containing pyrimidine 2-aminopyrazole derivatives (XO44 analogs) used for kinobeads profiling. (C and D) Kinobeads analyses of compound sets (1–6) using mixed cell extracts (C) or Jurkat extracts (D), showing total and competed kinases. (E) Correlation of binding strengths for competed proteins (>50% competition at 30 μM) between compounds **2** and **3** in Jurkat extracts. (F) Kinobeads profiling of Jurkat cells treated with compounds **2** and **3** for 60 min. (G) Correlation of binding strengths for competed proteins (>50% competition at 30 μM) between compounds **2** and **3** in treated Jurkat cells. Adapted with permission from ref. 142 Copyright 2025, The Authors. Published by Elsevier Inc. on behalf of American Society for Biochemistry and Molecular Biology.

In another study, Glocker *et al.* presented a comprehensive strategy for developing and optimizing activity-based probes to monitor kinase target engagement in live cells (Fig. 29).[142] The design began with the XO44 scaffold, a broad-spectrum covalent kinase inhibitor that reacts with the conserved catalytic lysine in most kinases. Its core contains a pyrimidine 2-aminopyrazole motif that mimics ATP binding, a sulfonyl fluoride warhead for covalent modification, and an ATP-competitive mechanism. To improve downstream enrichment, the traditional alkyne handle was replaced with a *trans*-cyclooctene group, enabling copper-free bioorthogonal conjugation through the inverse electron-demand Diels–Alder (IEDDA) reaction with tetrazine-biotin. This modification simplified the workflow, eliminated copper-induced artifacts, and provided higher enrichment efficiency. Kinobeads assays showed that the optimized probe affected fewer kinases in extracts yet performed better in live cells.

Comparative profiling confirmed that Probe **3** captured 171 kinases in live cells, of which 137 were robust, outperforming the alkyne-based variant. Multiplexed TMT-based quantification enabled detailed dose–response profiling, showing excellent reproducibility and robust statistical power. The platform was benchmarked using clinical kinase inhibitors. Unexpectedly, the study identified non-kinase off-targets, further validated through competition experiments with known inhibitors. The broader biomedical applications of this work include proteome-wide selectivity profiling, mechanism-of-action studies, and scaffold optimization during drug development. The platform supports therapeutic window determination, dose optimization, and biomarker discovery for pharmacodynamics, resistance, and patient stratification. Its compatibility with *ex vivo* patient samples opens opportunities for precision medicine, companion diagnostics, and real-time treatment monitoring. Importantly, live-cell profiling revealed binding patterns that lysate systems could not capture, highlighting the physiological relevance of the approach.

4.5. Future perspectives for kinase imaging *via* fluorescence

Kinase-targeted probes exemplify how molecular design and translational science are converging to drive innovation in oncology.[143,144] Although challenges persist in synthesis, pharmacokinetics, and imaging depth, ongoing advances in fluorescence and PET probe design promise to expand the role of kinase-specific probes in precision medicine. These tools are poised to transform our understanding of disease mechanisms and therapeutic responses, paving the way for more targeted and effective cancer care. However, several challenges remain in optimizing tissue penetration, reducing off-target activation, and enhancing contrast in complex biological environments. The next frontier lies in hybrid platforms: lanthanide-tagged probes for multiplexed imaging (see next chapter), photoactivatable probes for spatiotemporal control, and dual-purpose agents that bridge diagnostics and therapy. These innovations collectively point to a future where kinase imaging is integrated into clinical decision-making, not merely to observe, but to guide, personalize, and optimize cancer treatment in real time. Together, these strategies showcase a multifaceted approach to designing kinase-specific probes, combining chemical biology, pharmacology, computational modeling, synthetic chemistry, biological validation, and diverse imaging modalities to tackle complex biological and clinical challenges.

Despite substantial progress in the development of kinase-specific probes, several limitations hinder their broader clinical adoption. A major constraint is tissue penetration. Most fluorophores operate in the visible light spectrum, which restricts their utility for deep-tissue imaging. Some of the reviewed works explored red-emitting and NIR probes; however, there is a growing demand for fluorophores that emit in the NIR-II window. These offer even deeper tissue penetration, higher spatial resolution, and lower background interference due to reduced scattering and absorption-showing potential for whole-body imaging.[18,145,146] Liu *et al.* demonstrated how introducing reversibility in probe design expands their utility in pharmacophore screening for drug discovery.[128] Moreover, reversible probes may offer distinct advantages. Compared to irreversible inhibitors, which provide prolonged action and often enhanced potency, reversible inhibitors can dissociate from their targets, reducing risks of toxicity and immunogenicity, and allowing for tunable residence.[144,147–150] These properties may enhance inhibition control and improve the clinical translatability of such probes.

Fluorescent "non-dye-derived" inhibitors that intrinsically report their binding status fill an important gap in chemical biology, as they are rare compared to conventional dye-conjugated kinase inhibitors. This approach aligns with green chemistry principles by eliminating the need for external fluorophores, improving atom economy, and simplifying synthesis. These benefits underscore the need for more innovation and expansion in this area. Following Fleming *et al.*, the ability to achieve spatiotemporal control over kinase activity in live cells opens new opportunities to study kinase signaling in complex systems.[139,140] Real-time monitoring of drug release and target engagement could inform research on drug resistance and support optimization of therapeutic dosing. Clinically, selective activation in diseased tissue could reduce systemic toxicity and improve outcomes, especially relevant in autoimmune diseases and cancers involving LCK. Caged probes also offer promise for multiplexed systems, an underexplored yet promising frontier. Targeting multiple kinases at different wavelengths could elucidate complex signaling crosstalk in tumors, offering a more comprehensive view of oncogenic networks and their dynamic response to treatment. However, current designs are primarily focused on single-target probes, highlighting a need for innovation. Additionally, incorporating two-photon activation strategies could enhance spatial resolution, making this approach powerful for subcellular imaging and precision pharmacology. Another challenge is applying kinase inhibitors to brain tumors due to the blood–brain barrier (BBB), necessitating the design of brain-penetrant chemical probes that yield measurable signals for both research and therapeutic monitoring. Müller *et al.* highlighted the need for BBB-optimized analogs to enable imaging of HER2-positive brain metastases.[151] A viable solution lies in pharmacophore-driven probe design based on novel, brain-penetrable HER2 TKIs.[152–154] Lastly, the development of probes derived from small-molecule bivalent inhibitors, targeting both the ATP and substrate binding sites, remains limited, despite their potential to enhance selectivity.[155,156]

5. Fluorescent probes for other enzymes

Over the last years, increasing attention has been directed toward developing chemical tools for monitoring glycosidase activity in biomedical applications. Glycosidases catalyze the hydrolysis of glycosidic bonds in glycoconjugates, including glycoproteins and glycolipids.[157] The altered expression of these enzymes has been linked to tumor initiation, progression, and metastasis, creating opportunities for targeted diagnostic

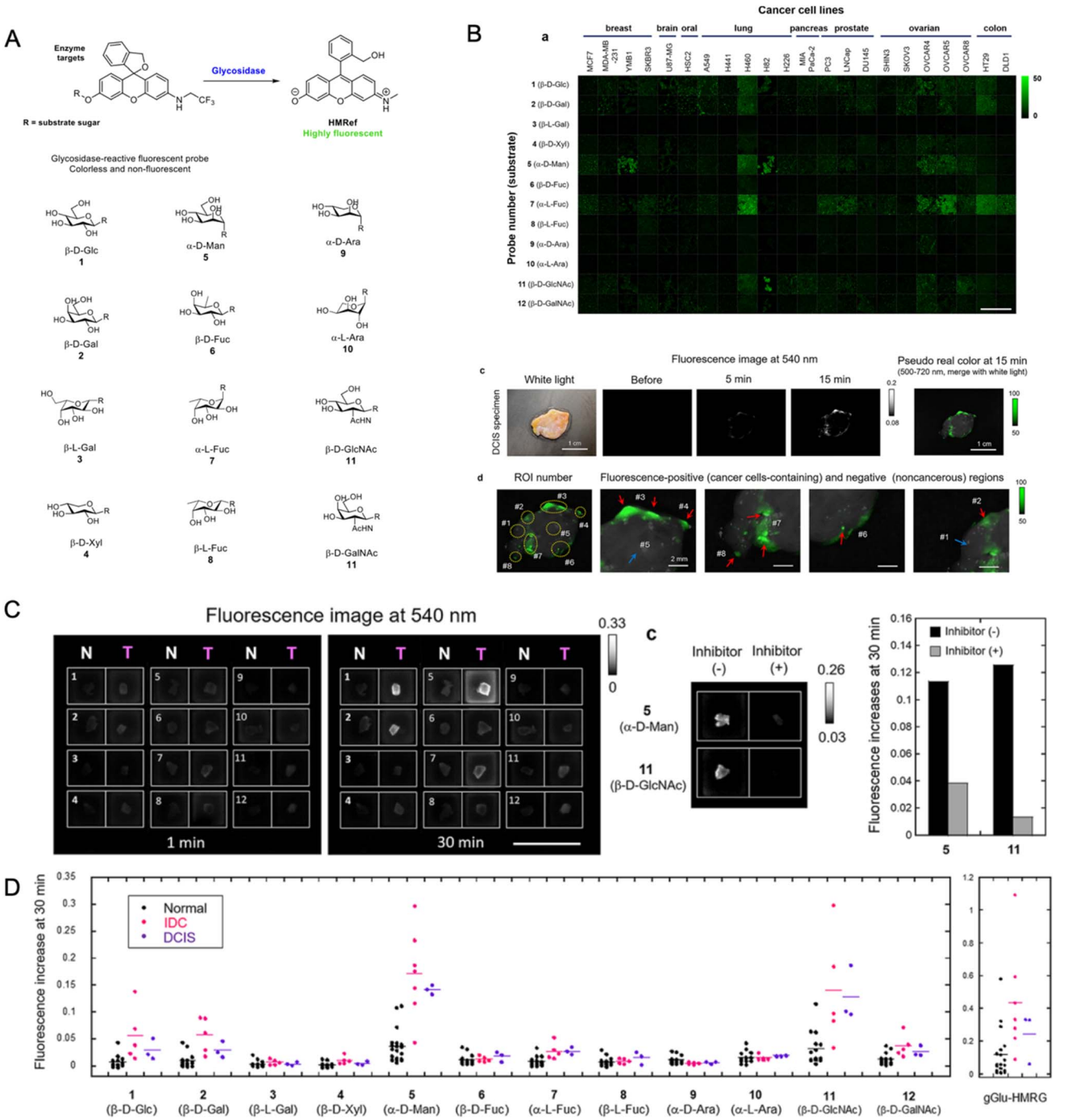

Fig. 30 Fluorescent probes for detection of glycosidase activities. (A) These probes exist in colorless, nonfluorescent spirocyclic forms, but are converted to a colored, highly fluorescent hydrolysis product HMRef, which emits green fluorescence, upon reaction with the targeted glycosidase. (B) Fluorescence imaging of glycosidase activities in 22 living cancer cell lines. All fluorescence images were captured 1 h after administration of each fluorescent probe. Time-dependent fluorescence image of surgically resected frozen human DCIS specimen containing both normal and cancer tissues after administration of **HMRef-αMan** ROI number of the evaluated DCIS specimen (left). Fluorescence-positive (red arrows) and -negative (blue arrow) regions (right). Cancer cells were detected in all fluorescence-positive ROIs by histological analysis. (C) Screening of glycosidase-reactive fluorescent probes for the detection of breast tumors. Example of screening using surgically resected frozen human breast IDC and normal tissues. The compound number of the applied probe is shown on each well. Black bars: fluorescence increase in the absence of inhibitor. Gray bars: fluorescence increase in the presence of inhibitor. (D) Comprehensive analysis of intact glycosidase activities in normal breast, IDC and DCIS tissues using 12 fluorescent probes or **gGlu-HMRG.** Fluorescence increase represent increase at 30 min from 1 min after addition of fluorescent probes. Black, pink, and purple dots represent fluorescence increases in normal breast, IDC and DCIS tissues, respectively. Adapted with permission from ref. 158 Copyright 2020, American Chemical Society.

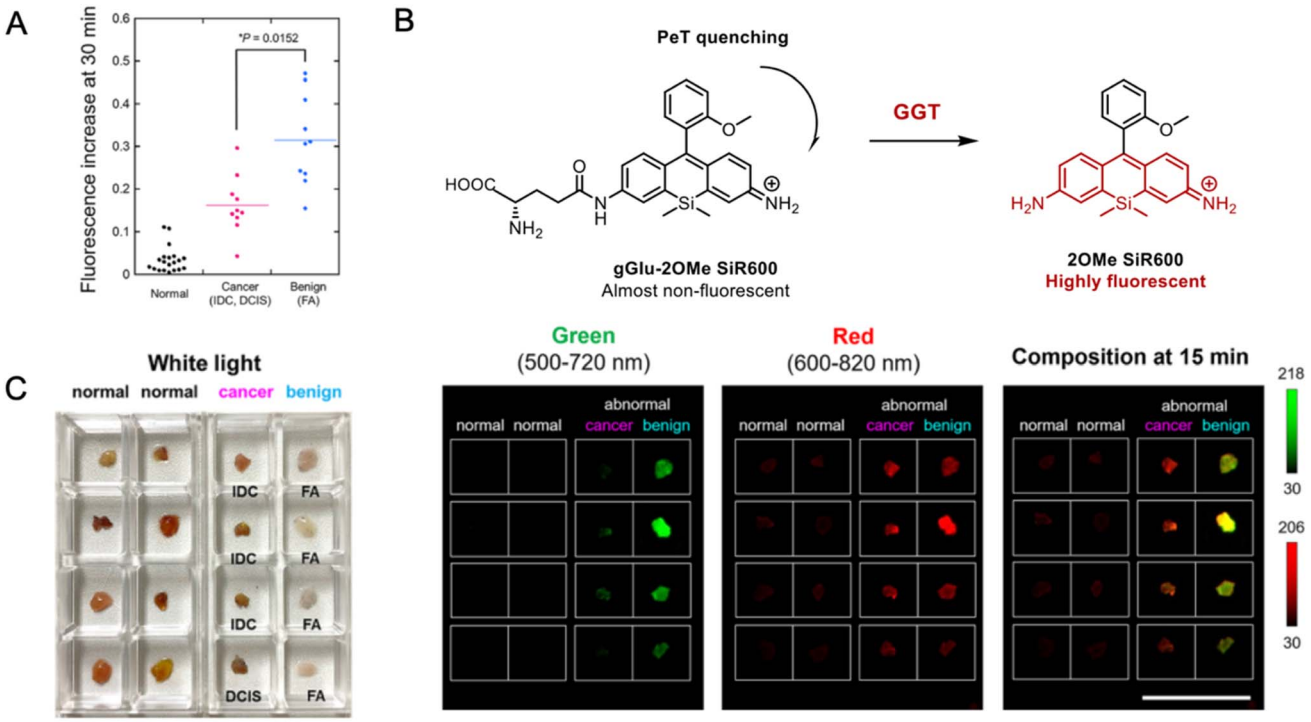

Fig. 31 Application of fluorescent probes for optical discrimination of breast cancer and benign breast lesions. (A) Fluorescence increase of **HMRef-αMan** in normal, malignant (IDC, DCIS), and benign (FA) tissues. The probe showed stronger signals in FA than in cancer tissues. (B) A newly developed activatable red fluorescent probe for GGT, **gGlu-2OMe** SiR600, with fluorescence quenched *via* PeT. (C) White light (left) and dual-color fluorescence images (right) of normal, malignant, and benign tissues acquired 15 min after administration of both probes. Adapted with permission from ref. 158 Copyright 2020, American Chemical Society.

approaches. Glycosidase-activated fluorescent probes serve as valuable tools that exploit this dysregulated enzyme expression, enabling investigation of functional roles and spatial distribution within complex biological environments to advance understanding of disease mechanisms.

Fujita *et al.* reported the development of a chemical probe designed to target α-mannosidase for the rapid and precise visualization of breast tumors. In their study, the authors synthesized a series of 12 glycosidase-responsive probes derived from the HMRef scaffold (Fig. 30).[158] These probes remain non-fluorescent while conjugated to a sugar substrate however, upon rapid one-step cleavage of this group by the target enzyme, they begin to emit a strong fluorescent signal. This transformation enables highly sensitive detection of glycosidase activity in living cells. The lead compound **HMRef-αMan** (Probe **5**) targets α-D-mannose and undergoes enzymatic cleavage by α-mannosidase to generate highly fluorescent HMRef with green emission at 540 nm. Through diced electrophoresis gel assay and peptide mass fingerprinting, the authors identified α-mannosidase 2C1 (MAN2C1) as the specific target enzyme responsible for probe activation in breast tissues. MAN2C1 belongs to glycoside hydrolase family 38 and is involved in processing free oligosaccharides in the cytosol. When applied to surgically resected human breast specimens, **HMRef-αMan** demonstrated 90% sensitivity and 100% specificity for breast cancer detection, outperforming the previously reported **gGlu-HMRG** probe (80% sensitivity, 79% specificity). The probe successfully detected invasive ductal carcinoma, ductal carcinoma *in situ*, and various benign lesions including fibroadenoma, with the ability to visualize lesions smaller than 1 mm within 15 minutes (Fig. 31). Immunohistochemical analysis confirmed MAN2C1 overexpression in both malignant and benign breast tumors compared to normal tissue. Notably, the authors discovered that fibroadenoma exhibits higher MAN2C1 activity than malignant cancer tissues. To discriminate between malignant and benign lesions, they developed a dual-color imaging strategy combining green-emitting **HMRef-αMan** with a newly synthesized red-emitting probe **gGlu-2OMe** SiR600 targeting γ-glutamyltranspeptidase. This approach enabled optical discrimination where normal tissues showed no fluorescence, malignant cancer appeared red, and benign fibroadenoma displayed yellow composite fluorescence. The study establishes MAN2C1 as a novel biomarker for breast tumors and demonstrates the example of enzyme activity-based optical discrimination between malignant and benign breast lesions.

Traditional glycosidase probes often rely on glycosylation of phenolic groups on donor–acceptor fluorogens, but these probes suffer from aggregation-caused quenching (ACQ), limited substrate scope, low sensitivity, and poor performance in long-term cell imaging. To address these limitations Dong *et al.* developed aggregation-induced emission (AIE)-based glycoclusters as a general platform for glycosidase detection (Fig. 32).[159] These probes exploit the unique properties of AIE fluorophores, including high photostability, enhanced signal-

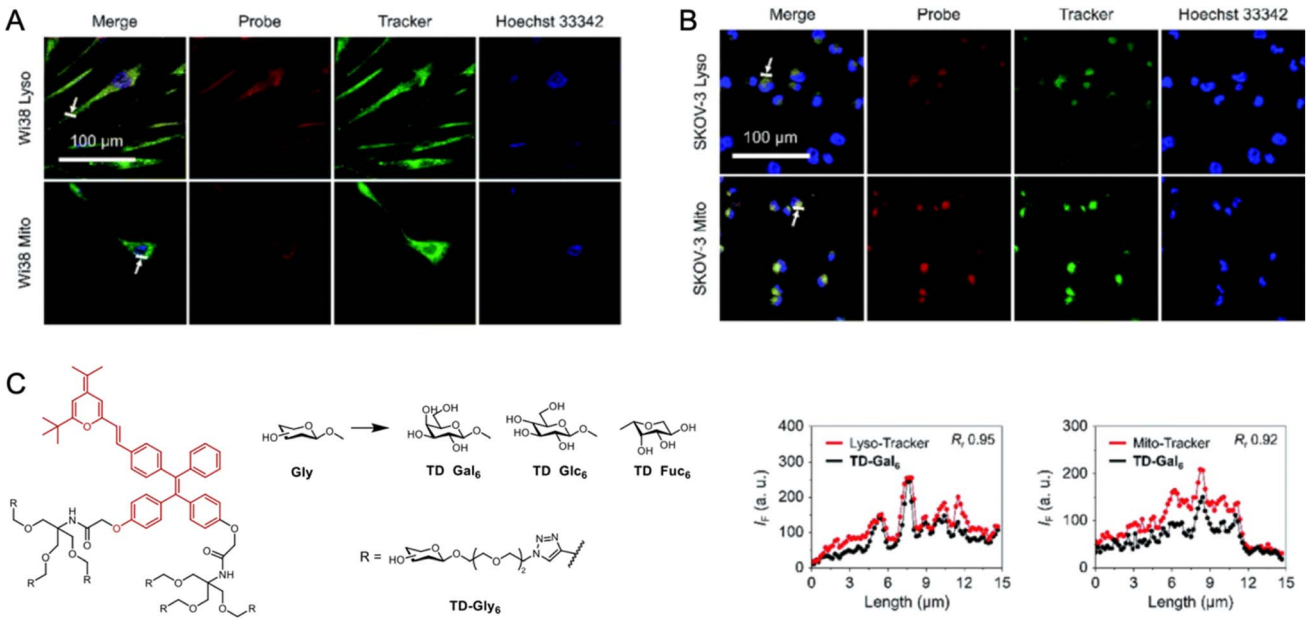

Fig. 32 Fluorescence visualization and quantitative analysis of **TD-Gal6**. β-Galactosidase activity in (A) senescent Wi38 lung-derived fibroblasts and (B) SKOV-3 human ovarian cancer cells, with signal quantification indicated by arrows. Subcellular localization studies employed mito-tracker and lyso-tracker for colocalization analysis with the probe. (C). Structure of the AIE glycoclusters synthesized in this study including AIE-based galactosyl cluster **TD-Gal$_6$**, glucosyl cluster **TD-Glc$_6$**, and fucosyl cluster **TD-Fuc$_6$**. Adapted with permission from ref. 159 Copyright 2022, The Authors. Published by the Royal Society of Chemistry.

to-noise ratios, and large Stokes shifts, offering significant advantages over conventional fluorescent systems. The design strategy centers on a tetraphenylethylene core conjugated with a dicyanomethylene-4H-pyran derivative (TPE-DCM), functionalized with dendritic arms bearing six monosaccharide units (D-galactose, D-glucose, or L-fucose) *via* azide–alkyne click chemistry. The hexavalent architecture (**TD-Gal$_6$** for β-galactosidase detection) ensures high water solubility and prevents undesired aggregation in aqueous environments. Upon enzymatic cleavage of the sugar epitopes by the corresponding glycosidase, the resulting amphiphilic molecules undergo hydrophobic aggregation, triggering a dramatic fluorescence enhancement through the AIE mechanism. The glycocluster probes demonstrated exceptional analytical performance with low detection limits for *A. oryzae* and *E. coli* β-galactosidase, respectively. Fluorescence emission occurs at 625 nm upon excitation at 420 nm, with high selectivity over other biomolecules including glutathione, esterase, alkaline phosphatase, lysozyme, and cellulase. The modular synthetic approach enables facile preparation of substrate-specific probes for β-D-galactosidase, β-D-glucosidase, and α-L-fucosidase. Cellular imaging studies validated the biological utility of these probes. **TD-Gal$_6$** successfully visualized endogenous β-galactosidase activity in SKOV-3 ovarian cancer cells and H_2O_2-induced senescent Wi38 fibroblasts, while showing negligible fluorescence in control cells lacking enzyme expression. Subcellular localization analysis revealed differential enzyme distribution between cell types, with high colocalization coefficients with lysosomal and mitochondrial trackers. The AIE-based probes enable prolonged cellular imaging with maximum fluorescence intensity achieved after 24 hours and signals maintained for up to 48 hours due to slow exocytosis of the aggregated fluorophores. This work establishes AIE-based glycoclusters as powerful tools that overcome synthetic limitations of traditional glycosidase probes while providing enhanced sensitivity, selectivity, and extended imaging capabilities for glycobiology research and diagnostic applications.

LAN-gal is a membrane-permeable, activatable fluorescent chemosensor developed to detect β-galactosidase an important biomarker for ovarian cancer and cellular senescence (Fig. 33).[160] The probe couples a D-galactose recognition motif to the high-quantum-yield reporter LAN-OH. In its intact form the galactose unit quenches fluorescence, but enzymatic cleavage by β-galactosidase releases the phenolic donor, amplifies intramolecular charge transfer (ICT) and produces a dramatic (>2000-fold) fluorescence turn-on. Kinetic and analytical characterization show **LAN-gal** has strong affinity and catalytic performance and excellent sensitivity. Probe is highly selective *versus* common interfering ions, proteins and enzymes, and allows reliable quantification in human biofluids. Cellular studies confirmed enzyme-specific activation: **LAN-gal** brightly visualizes endogenous β-galactosidase in ovarian cancer lines (SKOV-3, A2780), while normal ovarian cells (IOSE80) and other cancer lines (HeLa, HepG2) show minimal signal; pre-treatment with D-galactose blocks fluorescence, verifying β-galactosidase-mediated activation. The probe also detects elevated enzyme activity in senescent cells induced by H_2O_2 or MLN4924. *In vivo* validation in xenograft models showed rapid accumulation in A2780 tumors (within minutes) with stable signals for at least 5 hours, HepG2 xenografts remained non-fluorescent. Critically,

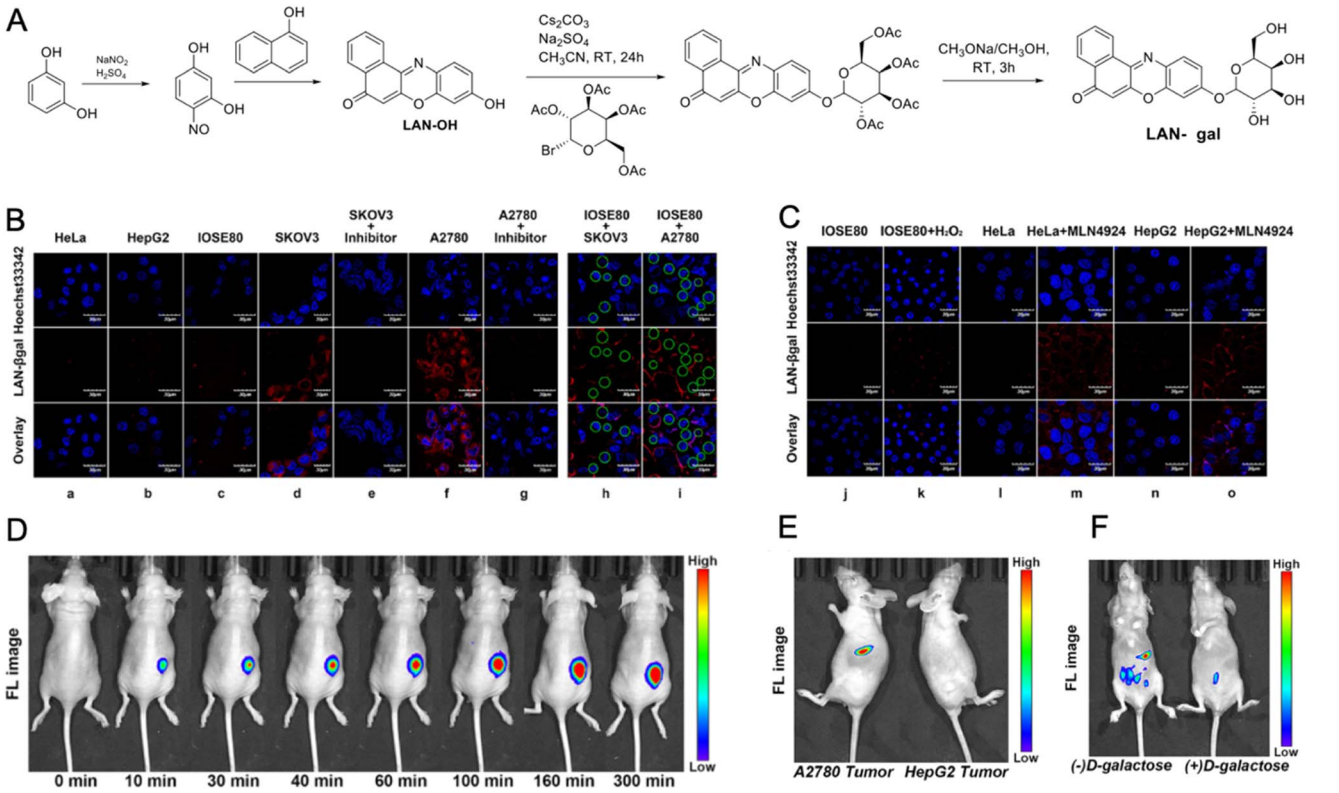

Fig. 33 Visualization of endogenous β-Gal *in vitro* and *in vivo*. (A) Synthetic route of **LAN-βgal** probe. (B) Fluorescence images of endogenous β-gal in living cells. (C) Comparison of fluorescence images of non-senescent cells (j, l, and n) and senescent cells (k, m, and o). (D) Fluorescence images of β-gal in the A2780 tumor-bearing mouse intratumorally injected with **LAN-βgal** captured at different times. (E) Fluorescence images of β-gal in bare BABL/c mice bearing the A2780 tumor (left) and HepG2 tumor (right) after being intratumorally injected with **LAN-βgal**. (F) Fluorescence images of β-gal in the peritoneal metastatic tumor model. Adapted with permission from ref. 160 Copyright 2023, American Chemical Society.

LAN-gal enabled fluorescence-guided surgery *via in situ* spraying, delivering an unprecedented tumor-to-normal tissue fluorescence ratio and permitting precise margin delineation and tumor excision while preserving healthy tissue. Overall, **LAN-gal** unites exceptional sensitivity and practical utility across cellular and animal models, making it a powerful translational tool for glycosidase research and real-time surgical guidance in ovarian cancer.

Phosphatases serve as essential counterbalances to kinases in cellular regulation, orchestrating fundamental biological processes including cell cycle progression, signal transduction cascades, metabolic control, and stress responses through the precise removal of phosphate groups from target proteins.[161] These enzymes act as molecular switches that can both attenuate and amplify signaling pathways, controlling the spatiotemporal dynamics of protein phosphorylation networks and determining critical cell fate decisions such as proliferation, differentiation, or apoptosis. Chemical probes for imaging phosphatase activity are therefore indispensable tools for biomedical research, as dysregulation of these enzymes underlies numerous pathological conditions including cancer, neurological disorders, and metabolic diseases, making real-time visualization of their activity crucial for understanding disease mechanisms and developing targeted therapeutic interventions.[162,163]

In 2025 Liang *et al.* reported the first near-infrared (NIR) fluorescent ligands specifically designed to image SHP2, a protein tyrosine phosphatase implicated in cancer progression, immune regulation, and therapeutic resistance (Fig. 34).[164] Unlike traditional enzyme activity-based probes, these small-molecule ligands-termed the **SHP-PP** series-bind directly to the SHP2 allosteric site, providing a target-specific, environment-sensitive imaging approach. The probes were constructed by conjugating pharmacophore fragments derived from potent SHP2 inhibitors such as SHP099, RMC-4550, and TNO155 with the environment-responsive NIR fluorophore Py-5, which offers a large Stokes shift, high photostability, and sensitivity to local polarity and viscosity. Structural optimization introduced flexible PEG linkers to fine-tune probe-target interactions, with SHP-P2 emerging as the lead candidate, showing strong SHP2 binding affinity, high selectivity over related phosphatases, and high stability under physiological conditions. The probes exhibited a fluorescence "turn-on" response upon binding SHP2, as the fluorophore's quantum yield increased in hydrophobic protein environments, yielding high signal-to-noise ratios without washing steps. In living cells, **SHP-PP2** selectively labeled SHP2-overexpressing cancer cells such as ACHN and MDA-MB-231, while pre-treatment with the inhibitor SHP099 abolished fluorescence, confirming binding specificity. Tissue imaging studies further demonstrated that

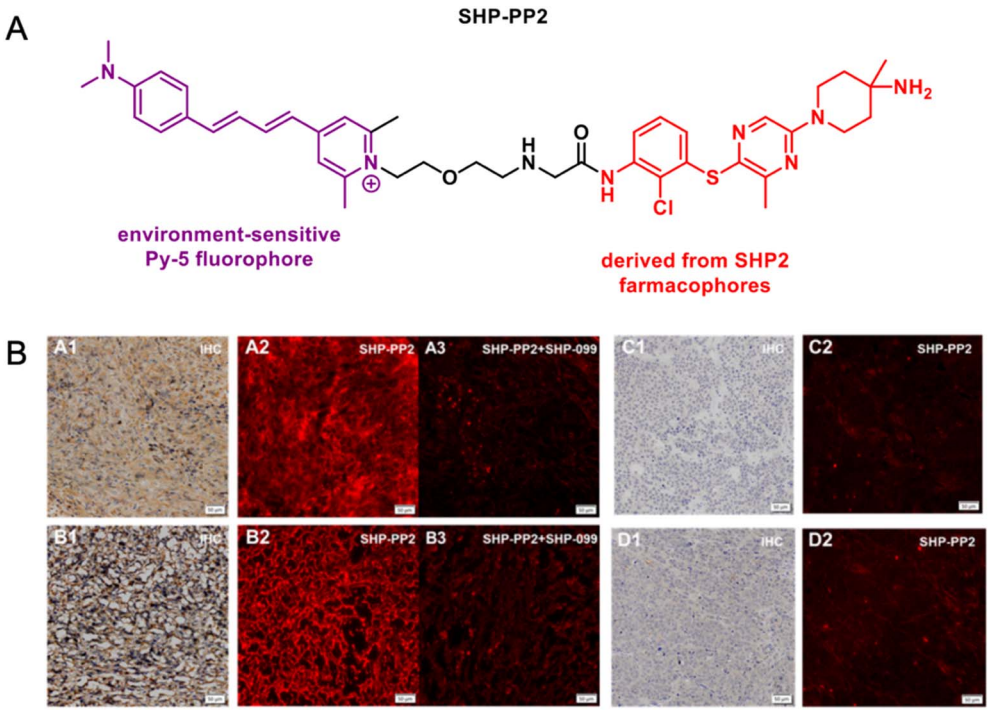

Fig. 34 Labeling of SHP2 in living cells. (A) The structure of **SHP-PP2** probe for to image SHP2. (B) IHC and fluorescence imaging of tumor tissue sections: (A1–3) ACHN tumor, (B1–3) MDA-MB-231 tumor, (C1 and 2) KM-3 tumor, (D1 and 2) Fadu tumor. Adapted with permission from ref. 164 Copyright 2025, American Chemical Society.

fluorescence intensity correlated with SHP2 expression across tumor samples, validated by immunohistochemistry and western blot analysis. Preliminary *in vivo* experiments showed tumor accumulation and biodistribution consistent with SHP2's known physiological roles, supporting translational feasibility. Compared to antibody-based and substrate-dependent assays, these probes enable rapid, real-time, and non-destructive imaging of SHP2 in live cells and tissues. Overall, the **SHP-PP** series establishes a pioneering platform for direct visualization of phosphatase targets, offering powerful new tools for cancer diagnostics, drug development, and precision therapeutic monitoring in SHP2-driven diseases.

Environment-sensitive fluorescent probes represent a sophisticated class of molecular imaging tools that exploit changes in the local microenvironment around fluorophores to report on protein interactions, with their fluorescence properties being dramatically altered upon binding to hydrophobic active sites or undergoing conformational changes. The environment-sensitive strategy has been extensively developed for kinases due to their well-characterized ATP-binding sites and the significant microenvironmental changes that occur upon substrate phosphorylation, making them ideal targets for this approach.[165] In contrast to the wealth of kinase-targeted environment-sensitive probes, there remains a notable gap in recent examples of such probes designed for proteases, representing an underexplored area with significant potential for future development. This scarcity of protease-targeting environment-sensitive probes presents a compelling research opportunity, as proteases offer unique microenvironmental changes upon substrate cleavage that could be exploited for selective detection and real-time activity monitoring.

6. Beyond fluorescence: metal-tagged probes for enzyme imaging

6.1. PET probes for kinases

Positron emission tomography represents one of the most sensitive and clinically translatable imaging modalities for non-invasive visualization of biochemical processes *in vivo*. In the context of enzyme-targeted imaging, PET probes offer a powerful alternative to traditional fluorescence-based approaches by enabling deep-tissue imaging with high resolution and quantitative accuracy. Central to this technology are radiometals, such as ^{64}Cu, ^{68}Ga, and ^{89}Zr, which serve as isotope tags for enzyme-responsive probes, providing real-time insights into enzyme activity within pathological environments. Unlike fluorescent reporters, which are often limited by tissue penetration, scattering, and autofluorescence, radiometal-based probes allow whole-body imaging of enzyme function, making them especially valuable in oncology, neurology, and infectious disease. These probes typically consist of a targeting scaffold, such as an enzyme substrate, inhibitor, or affinity ligand, conjugated to a metal chelator that stably binds a PET-active isotope. Upon enzymatic activation or binding, the radiolabeled probe accumulates in diseased tissues, where signal intensity correlates with enzyme activity or expression. Enzyme-targeted PET imaging has shown promise in detecting cancer-associated proteases, glycosidases, and oxidoreductases,

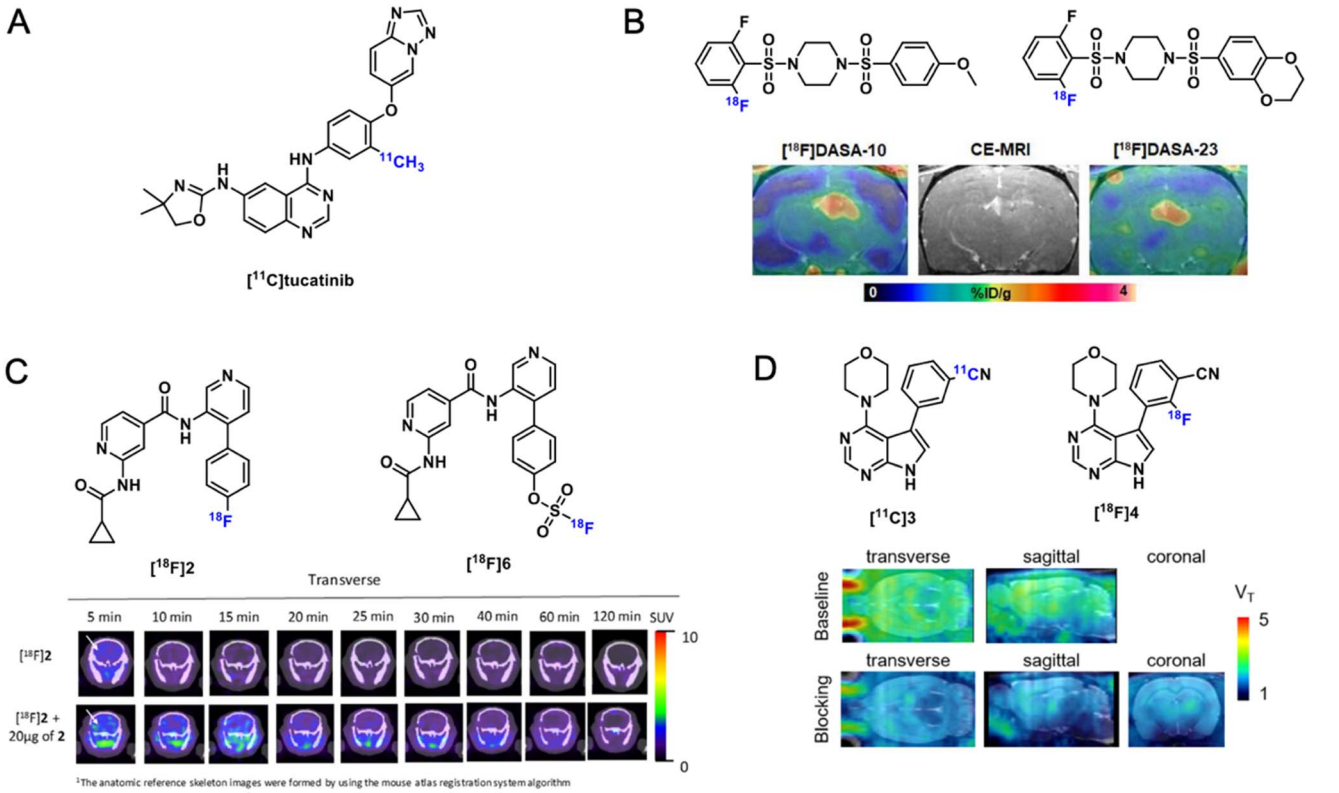

Fig. 35 PET probes for kinases. (A) The structure of **[^{11}C]tucatinib**. (B) Comparative testing of **[^{18}F]DASA-10** and **[^{18}F]DASA-23** in syngeneic C6 rat models of glioma. PET images are summed 10–30 min post intravenous administration of radiotracer. (C) Representative PET/X-ray images (transverse section) showing uptake of **[^{18}F]2** with 20 μg of 2 in brain (white arrow) of wild-type FVB/NJ mice at different time points post-injection. (D) PET images of **[^{18}F]4** in rats under baseline and blocking conditions. (B) Adapted with permission from ref. 170 Copyright 2023, Elsevier Inc. (C) Adapted with permission from ref. 171 Copyright 2024, The Authors. Published by Springer Nature. (D) Adapted with permission from ref. 172 Copyright 2024, The Authors. Published by American Chemical Society.

enabling not only diagnosis but also treatment monitoring and patient stratification. Importantly, the metal-based nature of these probes also facilitates integration with theranostic approaches (see next chapter), as the same molecular scaffold can be adapted for either therapeutic radionuclides or targeted drug delivery. Nevertheless, PET imaging has already been widely employed in preclinical studies to monitor therapeutic responses using enzyme-responsive readouts, offering a non-invasive means to assess treatment efficacy in real time.[166,167]

In the field of kinase-based diagnostics, positron emission tomography offers an alternative approach, providing highly sensitive, quantitative, and whole-body imaging of kinase expression and drug engagement *in vivo*.[168,169] PET tracers based on small-molecule kinase inhibitors can enable non-invasive assessment of target distribution, pharmacokinetics, and therapeutic response across various tumor types. One of such example was described by Müller *et al.* who attempted to develop the first small-molecule PET tracer selective for HER2 by synthesizing **[^{11}C]tucatinib**, a radiolabeled analog of the FDA-approved HER2 tyrosine kinase inhibitor tucatinib (IC_{50} = 6.9 nM for HER2) (Fig. 35A).[151] The tracer was prepared *via* a Stille coupling reaction between [^{11}C]methyl iodide and a trimethylstannyl precursor, yielding high radiochemical purity (>97%) but only moderate radiochemical conversion (54 ± 13%) and variable molar activity (15.1 ± 6.4 GBq μmol^{-1}). Despite the parent drug's known blood–brain barrier (BBB) penetration, **[^{11}C]tucatinib** showed minimal brain uptake (0.5% ID g^{-1} at 6 minutes post-injection) in HER2-positive SKOV-3 xenograft mice, likely due to altered lipophilicity ($\log D = 2.43$). Furthermore, the tracer exhibited high nonspecific accumulation in the liver (15.4% ID g^{-1}) and intestines, resulting in poor tumor-to-background contrast and limiting its suitability for HER2 imaging. The study highlights how even subtle structural changes, such as methyl group addition, can significantly impact pharmacokinetics by increasing hydrophobicity and reducing tumor specificity. These findings emphasize the need for structural optimization, such as introducing more polar functional groups or developing alternative HER2-targeted scaffolds, to improve PET imaging performance.

Applications of other PET probes for kinases have been more successful, a representative example being **[^{18}F]DASA-23**, which targets PKM2, an isoform of pyruvate kinase involved in cancer-specific glycolytic reprogramming.[173] This enzyme is highly upregulated in glioblastoma (GBM), making it a valuable biomarker for noninvasive imaging. PKM2 expression is minimal in healthy brain but markedly increased (4–5 times) in high-grade gliomas, providing high potential contrast for PET imaging relative to background brain tissue. **[^{18}F]DASA-23** is the

leading clinical candidate in this class and has already completed Phase I clinical trials at Stanford University (NCT03539731), where it demonstrated an excellent safety profile with no adverse reactions, acceptable radiation dose, efficient blood–brain barrier penetration, rapid clearance from healthy tissue, and high tumor-to-brain contrast. In both preclinical studies and patient cohorts, the probe consistently delineated GBM tissue from normal brain, with tumor-to-background ratios around 3.6, and achieved 4–9 fold higher uptake in glioblastoma compared to **[^{18}F]FDG**. Importantly, it identified metabolic non-responders within a week of treatment initiation, underscoring its value for early therapeutic response monitoring. With high radiochemical purity, stability in serum, and reproducible synthesis at clinically relevant molar activities, **[^{18}F]DASA-23** has set the benchmark for kinase PET probe development. Recent efforts have produced next-generation variants such as **[^{18}F]DASA-10**,[170] It was developed to address key limitations of **[^{18}F]DASA-23**, including high gallbladder radiation, non-specific brain white matter binding, and poor solubility (Fig. 35B). Chemically, **[18F]DASA-10** exhibited five-fold greater solubility in DMSO, solubility in ethanol, and improved PKM2 activity compared to **[^{18}F]DASA-23**, and was synthesized with high radiochemical purity. In cellular studies, **[^{18}F]DASA-10** showed significantly higher uptake and retention across multiple cell lines, with specificity confirmed *via* PKM2 siRNA knockdown and high binding affinity (K_D 15.7 nM). *In vivo*, it demonstrated reduced gallbladder uptake, efficient blood–brain barrier penetration, rapid clearance from healthy tissue, and favorable metabolic stability, resulting in markedly improved tumor-to-brain ratios and clear visualization of gliomas in rat models. These properties collectively reduce radiation exposure, enhance imaging sensitivity, and improve tumor contrast, making **[^{18}F]DASA-10** a strong candidate for clinical translation. While *in vivo* blocking studies are still needed, ongoing research is exploring its potential for monitoring metabolic treatment responses and advancing preclinical GBM imaging. Studies on both probes validate PKM2 as a molecular imaging target, highlight advantages over conventional metabolic tracers, and establish a workflow for future kinase probe translation, exemplifying how targeting metabolic kinases can yield robust imaging biomarkers for cancer detection, patient selection, and treatment monitoring.

Gundam *et al.* developed and evaluated two novel fluorine-18 labeled PET probes for non-invasive imaging of glycogen synthase kinase-3 (GSK-3) in the brain.[171] The work addresses the need for advanced imaging tools to study GSK-3, whose dysregulated activity has been implicated in Alzheimer's disease, Parkinson's disease, diabetes, and cancer. The researchers designed two isonicotinamide-based probes, **[18F]2** and **[18F]6**, to overcome the limitations of previous GSK-3 imaging agents with respect to brain permeability, stability, and binding affinity (Fig. 35C). **[^{18}F]2** was derived from a potent and selective GSK-3 inhibitor scaffold, whereas **[^{18}F]6** incorporated a fluoro-sulfate group enabling rapid isotopic exchange with ^{18}F-fluoride. Their synthesis employed methods such as Suzuki–Miyaura coupling, copper-mediated oxidative fluorination, and ^{18}F-SuFEx click chemistry. *In vitro* evaluation revealed that compound **2** exhibited superior blood–brain barrier permeability. Both probes bound GSK-3 with nanomolar affinity, with compound **2** showing slightly stronger activity than compound **6**. Compound **2** also displayed a lower radiochemical yield but greater molar activity. Serum stability testing further distinguished the two tracers: **[18F]2** remained fully stable in both mouse and human serum for at least 120 minutes, while **[^{18}F]6** degraded to about two-thirds of its initial concentration, likely due to covalent interactions between its SO_2F group and amines in serum proteins. Because of its superior profile, only **[^{18}F]2** advanced to *in vivo* studies in wild-type mice. PET imaging demonstrated good brain uptake at five minutes post-injection, followed by rapid clearance within 30 minutes. Unexpectedly, blocking experiments with co-administered cold compound **2** increased rather than decreased brain uptake, an effect attributed to peripheral binding in the liver, reduced hepatic metabolism, and potential saturation of cytochrome P450 enzymes, which collectively enhanced the bioavailability of the radiotracer. *Ex vivo* biodistribution confirmed elevated radioactivity in blood and increased uptake across multiple brain regions, including cerebellum, brain stem, thalamus, hippocampus, cortex, and caudate nucleus. These advances provide a strong foundation for developing clinically viable GSK-3 imaging agents that could improve understanding of neurological disease progression and support therapeutic development. Chen *et al.* evaluated novel PET probes for Imaging Leucine-Rich Repeat Kinase 2 (LRRK2), a key protein implicated in Parkinson's disease pathogenesis.[172] Two novel radioligands were synthesized on the basis of highly potent and selective inhibitor scaffolds. **[^{11}C]3** is the ^{11}C labeled version of PF-06447475, prepared *via* copper-mediated cyanation, while **[^{18}F]4** is a fluorine-18 labeled analog designed through multiparameter optimization and obtained using nucleophilic substitution (Fig. 35D). Both exhibited high radiochemical purity, strong binding affinity in the low nanomolar range for wild-type and mutant G2019S LRRK2, and favorable blood–brain barrier penetration with low efflux by P-glycoprotein. Docking studies suggested that their cyano substituents form key hydrogen bonds with residues in the binding pocket, accounting for their potency. *In vitro* autoradiography confirmed specific binding patterns consistent with known LRRK2 distribution, with highest uptake in hippocampus and striatum and lowest in brainstem and pons. Blocking with cold compound markedly reduced binding in LRRK2-rich regions, and cross-blocking with structurally unrelated inhibitors further validated specificity. Dynamic PET imaging in rats demonstrated rapid brain penetration and heterogeneous uptake matching LRRK2 expression, with tracer clearance proceeding mainly through hepatobiliary and urinary pathways. The compound showed greater metabolic stability in brain tissue than in plasma and no signs of defluorination. Validation in disease models underscored the clinical potential of **[^{18}F]4**. In G2019S transgenic mice, tracer uptake in the brain was significantly higher than in wild-type animals and correlated with a more than twofold increase in protein expression measured by western blot. In a neuroinflammation model induced by lipopolysaccharide, **[^{18}F]4** uptake was also elevated and corresponded to increased

LRRK2 expression. Whole-body distribution studies showed strong initial uptake in metabolic organs and rapid clearance, with no evidence of bone accumulation, consistent with metabolic stability. Among the two tracers, **[^{18}F]4** emerges as the more suitable candidate for clinical translation, offering higher synthetic yield, a longer half-life that facilitates imaging logistics, excellent stability, robust brain penetration, and sensitivity to pathological changes in LRRK2 expression. Together these findings establish the feasibility of clinically viable LRRK2 PET imaging, opening avenues for patient stratification in trials of LRRK2-targeted therapies and for non-invasive biomarkers to monitor treatment response. The work marks a significant step forward in the development of neuroimaging probes for Parkinson's disease.

6.2. PET probes for proteases

The protease field has also taken advantage of PET methodology for monitoring disease progression and therapeutic outcomes. A compelling example of rational design for an enzyme-responsive PET probe aimed at imaging therapy effectiveness was provided by the Craik and Evans laboratories, who developed a granzyme B-responsive PET substrate. In their 2021 study, the team introduced a class of imaging agents termed Restricted Interaction Peptides (RIPs), optimized for PET imaging of active proteases.[174] One such agent, **^{64}Cu-GRIP B**, was engineered to detect extracellular granzyme B, a serine protease secreted by cytotoxic T lymphocytes and NK cells during immune responses. The probe featured a granzyme B-cleavable linker (IEPDVSQV) flanked by a masking domain (QDPNDQYEPF) and a membrane-interacting domain (reporter-FVQWFSKFLGK) derived from the antimicrobial peptide temporin L. The masking domain, positioned at the C-terminus, prevented nonspecific membrane association, while the N-terminal amphipathic sequence remained inactive in the intact molecule. Upon cleavage by granzyme B, the masking domain diffused away, exposing the membrane-binding region, which then accumulated at the cell membrane, enabling radionuclide retention at sites of immune activity. In preclinical models, **^{64}Cu-GRIP B** successfully reported granzyme B activity *in vivo*. In a mouse model of CAR-T cell therapy, probe uptake strongly correlated with granzyme B secretion and cytotoxic activity. This enabled a non-invasive readout of immune cell function and therapeutic response, with PET imaging capturing both the spatial distribution and magnitude of granzyme activity. The study laid essential groundwork for the development of enzyme-responsive imaging agents in immuno-oncology. Building on these findings, the 2024 follow-up study expanded the utility of **[^{64}Cu]Cu-GRIP B** to infectious disease models and explored its translational potential.[175] The authors demonstrated that the probe could image granzyme B responses *in vivo* in murine models of both viral (H1N1 influenza A) and bacterial (*E. coli*, *P. aeruginosa*, *K. pneumoniae*, and *L. monocytogenes*) infections. PET/CT imaging showed significantly elevated probe uptake in infected tissues of wild-type mice, but not in granzyme B knockout mice, confirming the enzyme-specific signal. Importantly, **^{64}Cu-GRIP B** differentiated live bacterial infection from sterile inflammation-something conventional tracers like **^{18}FDG** often fail to achieve. This underscores its potential for accurate infection imaging. Moreover, the probe's ability to detect dynamic immune responses with high spatial and temporal resolution positions it as a powerful tool for both basic immunology and clinical decision-making. Together, these studies exemplify how protease-activated PET probes, particularly those responsive to granzyme B, can bridge the gap between immune function and molecular imaging. They not only offer real-time, non-invasive monitoring of immune activity, but also open new avenues for personalized medicine in cancer immunotherapy and infectious disease management.

6.3. Enzyme chemical probes for CyTOF applications

While radioactive metal isotopes have enabled powerful strategies for non-invasive imaging of enzyme activity *in vivo*, there is also growing interest in using non-radioactive, stable metal isotopes for enzyme-targeted probe design. These stable metals offer an attractive alternative for applications where long-term tracking, multiplexing, or *ex vivo* analysis is required, without the safety concerns and logistical limitations associated with radiotracers. Recent advances have demonstrated that stable metal-tagged probes can be effectively used to monitor enzymatic processes with high specificity and spatial resolution, opening new avenues for functional imaging and single-cell analysis in both basic research and translational settings. The ability to analyze biological systems at single-cell resolution has redefined our understanding of cellular heterogeneity, functional specialization, and disease progression. Over the past decades, cytometry-based technologies have evolved from classical fluorescence-based flow cytometry to more advanced high-dimensional systems. Among these, mass cytometry (CyTOF), that uses stable metal isotope as tags for biological and chemical probes, has emerged as a transformative platform that enables the simultaneous quantification of over 50 cellular markers, offering unprecedented resolution in systems-level biology.[176] Conventional flow cytometry relies on fluorophore-conjugated antibodies to detect target antigens. While powerful, this approach is limited by spectral overlap between fluorophores and detector resolution, which typically restricts the number of markers that can be measured simultaneously to fewer than 20. Even with the advent of spectral flow cytometry and complex compensation algorithms, the intrinsic overlap of emission spectra remains a challenge. This has prompted researchers to explore alternative technologies that decouple detection from light-based signals.[177,178]

Mass cytometry integrates flow cytometry with inductively coupled plasma time-of-flight mass spectrometry (ICP-TOF-MS) to enable high-dimensional single-cell analysis. First described in 2009 by Bandura and colleagues, CyTOF employs stable heavy metal isotopes, typically lanthanides, as tags conjugated to antibodies or molecular probes.[179] These isotopes offer minimal biological background and discrete mass signals, allowing simultaneous detection of over 40 parameters per cell with negligible signal overlap.[180] In a typical CyTOF workflow, cells

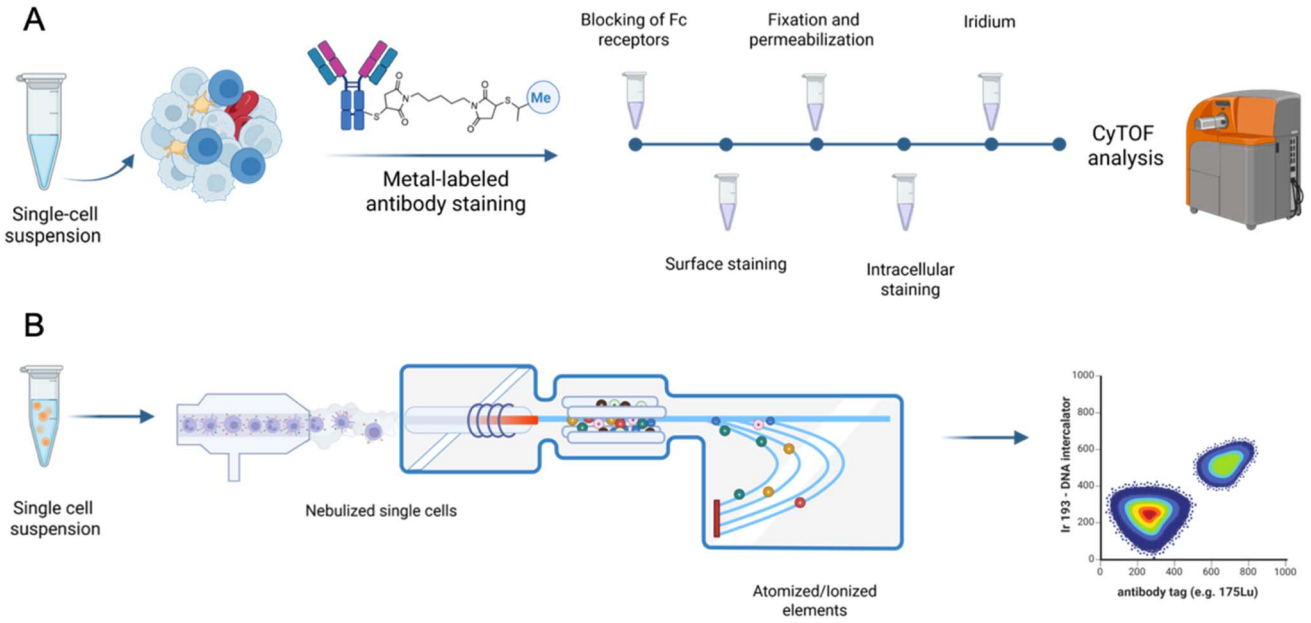

Fig. 36 The principles of mass cytometry. (A) Experimental workflow for CyTOF sample preparation. Suspended cells are first incubated with a viability reagent and blocked to prevent nonspecific Fc receptor binding. Next, cells are stained with metal-tagged antibodies against extracellular (surface) markers. After surface labeling, samples are fixed with paraformaldehyde and permeabilized to allow access to intracellular epitopes. Intracellular components are then labeled using a panel of metal-conjugated antibodies. Finally, cells are incubated with an iridium-based DNA intercalator to mark nuclei prior to acquisition on the CyTOF instrument. (B) Mass cytometry workflow. In the plasma, cell-bound, metal-conjugated antibodies and DNA intercalator complexes are rapidly atomized and ionized. The resulting cloud of metal ions is extracted into a time-of-flight mass spectrometer, where the ions are separated according to their mass-to-charge ratio. Signal intensities for each metal isotope are recorded on a per-cell basis, generating a high-dimensional dataset that captures surface and intracellular marker expression, as well as nuclear DNA content.

are stained with a panel of metal-labeled antibodies or probes, then aerosolized and introduced into an argon plasma, where they are vaporized, atomized, and ionized (Fig. 36). The resulting metal ions are analyzed by TOF mass spectrometry, generating a unique spectral fingerprint for each cell.[180] Unlike fluorescence-based cytometry, CyTOF does not require compensation for spectral overlap, enabling cleaner and more scalable multiplexing. Normalization techniques are essential to ensure data consistency across runs. A widely adopted method introduced by Finck *et al.* uses EQ Four Element Calibration Beads containing defined concentrations of metal isotopes to correct for signal drift.[181] Sample barcoding strategies, such as palladium- or CD45-based approaches, further enhance throughput by allowing multiple samples to be pooled and analyzed simultaneously while minimizing batch effects.[182] Data generated by CyTOF are high-dimensional and require computational processing, including normalization, debarcoding, dimensionality reduction (*e.g.*, t-SNE, UMAP), and unsupervised clustering (*e.g.*, FlowSOM, PhenoGraph) to uncover biologically relevant patterns.[183] While CyTOF is most commonly used with antibody panels for immune profiling, its capabilities have expanded through the development of metal-labeled chemical probes. These include activity-based probes and functional sensors to monitor protease activity, cell cycle progression, apoptosis, and metabolic states. Such tools add a dynamic, functional dimension to mass cytometry, enabling simultaneous assessment of cell identity and biochemical function at single-cell resolution.

Building upon the CyTOF, imaging mass cytometry was developed to add spatial resolution to high-dimensional cytometry. First introduced by Giesen *et al.*, IMC adapts the same antibody-metal labeling system but applies it to thin tissue sections instead of cell suspensions.[184] After staining with a multiplexed antibody panel, the tissue is ablated using a focused UV laser, releasing particles that are transported to the CyTOF detector for ionization and analysis. Unlike traditional immunofluorescence or immunohistochemistry, IMC allows the simultaneous detection of more than 40 markers at subcellular resolution. Spatial maps of protein expression are reconstructed from the sequential ablation data, preserving histological context while enabling deep molecular characterization.[185,186] The advantages of IMC are particularly evident in cancer research. In a landmark study, Moldoveanu *et al.* used IMC to map the immune landscape of melanoma tumors, where they profiled over 220 000 individual cells and characterized spatial relationships between tumor-infiltrating lymphocytes (TILs) and cancer cells. The proximity of $CD8^+CD45RO^+Ki67^+$ T cells to tumor regions predicted response to immune checkpoint blockade, highlighting the power of spatial proteomics in clinical oncology.[187] IMC has also been applied to study tissue remodeling, fibrosis, organ development, and drug biodistribution. Chang *et al.* demonstrated its use in assessing the biodistribution of cisplatin and revealed extensive platinum–collagen binding in both tumor and normal tissues.[185,186] Despite its strengths, mass cytometry has limitations, such as the destruction of cells during acquisition, limited sensitivity

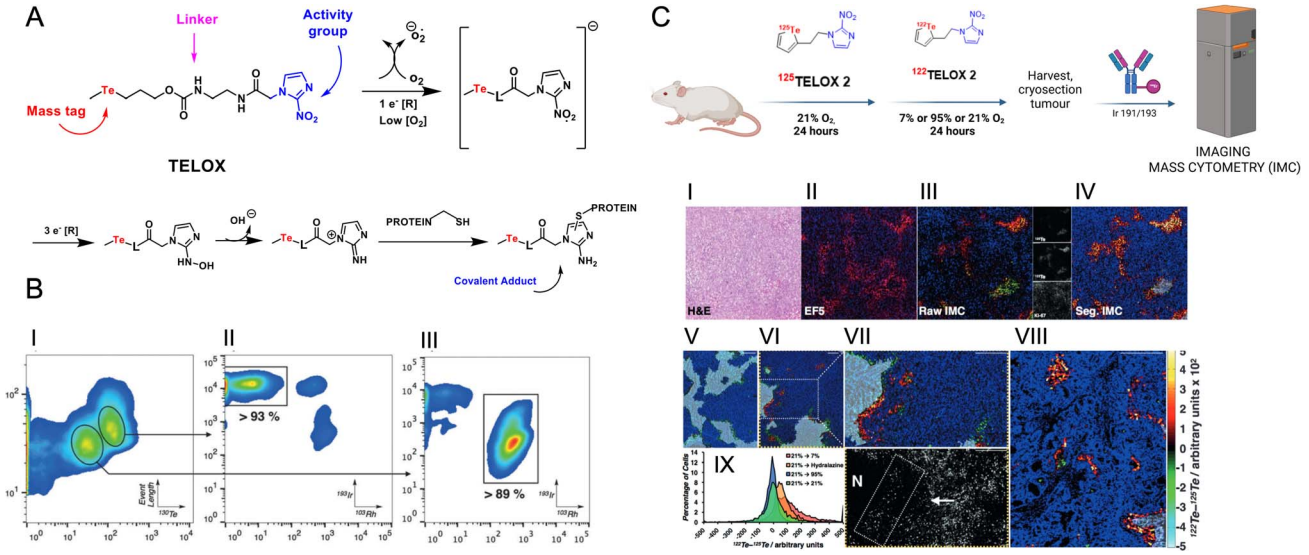

Fig. 37 Tellurium-based activity probes for mass cytometry. (A) First-generation **Telox**: enzyme-catalyzed reduction of the 2-nitroimidazole moiety generates an electrophilic nitrenium ion for covalent protein labeling. (B) Density map of event length *versus* ^{130}Te signal. Gated ^{193}Ir *vs.* ^{103}Rh plots showing >93% (upper-right) and >89% (lower-left) of events within the selected gates. Adapted with permission from ref. 22 Copyright 2014 WILEY-VCH Verlag GmbH & Co. KGaA, Weinheim. (C) **Telox** labeling on a 2nd-generation CyTOF. SLIP strategy for dynamic hypoxia mapping in PANC-1 xenografts: (I) H&E-stained tissue section. (II) Fluorescence microscopy image showing anti-EF5 antibody (pink) and DAPI nuclear staining (blue). Individual mass channels are displayed on the right. (IV) Processed image corresponding to (III); segmented cells are color-coded on a thermal scale (shown to the right of panel i) according to the ^{122}Te–^{125}Te ratio. (V) Processed image from an increased O_2-breathing (95%) model, and (VI) from a constant normoxia (21%) model. (VII) Magnified view of panel (VI): Ki-67$^+$ (^{168}Er) cells are displayed in grayscale. The proposed hypoxic turnover region and direction of cell displacement are indicated by the white box and arrow, respectively. (VII) Processed image from a 21% O_2-breathing OCIP-51 tumor model. (IX) Histograms of segmented cells from panels (IV–VI). In processed images, the blue channel represents ^{193}Ir (nuclear stain). Gray masks denote necrotic regions. Adapted with permission from ref. 189 Copyright 2016, WILEY-VCH Verlag GmbH & Co. KGaA, Weinheim.

for low-abundance proteins, slower acquisition rates compared to flow cytometry, and the need for specialized software to interpret high-dimensional data. Nonetheless, ongoing innovations continue to address these challenges. Recent advances include the expansion of the metal palette beyond lanthanides to include tellurium, palladium and platinum isotopes, improved ion transmission, barcoded DNA-tagged antibodies, and integration with single-cell transcriptomics (*e.g.*, CITE-seq).[180,188] As computational methods evolve, so too will the power and accessibility of mass cytometry and IMC. Given the above, mass cytometry and imaging mass cytometry represent a paradigm shift in cellular analysis, providing an integrated framework for phenotyping, functional profiling, and spatial mapping. Their ability to resolve complexity at the level of individual cells, both in suspension and within intact tissues, has made them indispensable tools in systems biology and translational medicine. Antibody-based reagents remain the main tools of phenotypic profiling in mass cytometry and imaging mass cytometry, but their ability to characterize functional states of cells is fundamentally limited. As interest grows in capturing dynamic biochemical processes, such as enzymatic activity, protein synthesis, or hypoxia, a parallel revolution has emerged in the form of chemical biology. The mass cytometry-compatible reagent have been recently reviewed by Arnett, and here we describe several examples that illustrate how mass cytometry can be harnessed for enzyme activity imaging.[41]

The earliest demonstration of activity-based chemical labeling compatible with mass cytometry came from Edgar *et al.* in 2014.[22] In this pioneering study, the authors introduced **Telox**, an organotellurium-containing probe for the detection of cellular hypoxia (Fig. 37). Built around a 2-nitroimidazole core, widely used in PET tracers and immunohistochemical hypoxia stains, **Telox** was equipped with a compact methyl-telluroether mass tag. Under hypoxic conditions, the 2-nitroimidazole moiety is enzymatically reduced to form a reactive nitrenium intermediate, which covalently binds to cellular thiols, anchoring tellurium in hypoxic cells. This electrophilic trapping strategy yielded excellent selectivity under low-oxygen conditions, confirmed *via* ICP-MS and CyTOF profiling of HCT116 cells. The probe demonstrated low toxicity and good stability, and its compatibility with MC opened new possibilities for functional profiling of tumor microenvironments. Building on this concept, Edgar *et al.* further reported a second-generation study in 2016, which introduced the use of isotopologous variants of **Telox**, ^{122}Te- and ^{125}Te-labeled analogs, applied in the so-called SLIP (sequential labeling with isotopologous probes) strategy.[189] In a pulse-pairing design, mice bearing PANC-1 xenografts were sequentially injected with isotopically distinct **Telox** variants. Tissue sections analyzed by IMC revealed spatial and temporal dynamics of hypoxia at single-cell resolution. The two probes, chemically identical but isotopically distinct, allowed quantitative imaging of changing oxygenation states,

even capturing diffusion-limited hypoxia near necrotic cores and vessels. This dual-isotope strategy demonstrated that temporal information could be encoded within small-molecule labels, a powerful step toward four-dimensional functional cytometry. Expanding the utility of organotellurium chemistry, Lumba *et al.* developed **GalTe** in 2017, a mass cytometry-compatible probe for detecting cellular senescence.[190] The probe consisted of a galactoside-protected quinone methide precursor tethered to a tellurophene tag. Enzymatic cleavage by senescence-associated β-galactosidase liberated a reactive intermediate that covalently modified intracellular thiols. This mechanism offered permanent, tellurium-based cell labeling, overcoming limitations of transient fluorogenic reporters. *In vitro* and *in vivo* validation revealed selective enrichment in senescent RPE and fibroblast populations. By coupling **GalTe** with IMC, the authors achieved high-resolution mapping of senescent cells within tissues, a valuable tool given the increasing relevance of senescence in cancer therapy, fibrosis, and aging. In 2019, Bassan *et al.* introduced TePhe, a tellurophene-based amino acid analog of phenylalanine that integrates directly into the translational machinery of cells.[191] Unlike traditional puromycin-based labeling, TePhe incorporation does not require starvation or chemical stress. Following its biosynthetic incorporation, TePhe can be visualized using IMC due to its tellurium signature. In murine tissues, TePhe identified zones of high translation, including proliferative niches in the gut and metabolically active tumor regions. By applying isotopologous versions of TePhe, the authors again demonstrated SLIP functionality, providing temporal resolution of protein synthesis. This study illustrated the power of using endogenous biochemical processes as entry points for chemical functional imaging. Together, these studies, performed in Nitz lab, demonstrate that tellurium-based probes provide a powerful and versatile platform for enzyme activity analysis by mass cytometry. Their design, incorporating tellurium *via* a stable carbon–element bond, eliminates the need for metal-chelating groups, preserving the physicochemical properties and biological compatibility of the probes. This strategy has enabled the development of selective, covalently binding reporters for diverse enzymatic processes such as hypoxia, senescence, and protein synthesis, with successful application in both CyTOF and IMC. Importantly, isotopologous tellurium labeling adds a temporal dimension to functional imaging, allowing dynamic biological processes to be tracked *in situ*. Importantly, this chemistry is uniquely suited to tellurium; other metals commonly used in mass cytometry, such as lanthanides, require chelation and cannot be directly introduced *via* stable covalent bonds. While this limits the use of other metals in similar probe designs, it also underscores the special role of tellurium as a rare but powerful element for covalent functional labeling in mass cytometry.

The first application of mass cytometry-compatible chemical probes for protease imaging was described by Poreba *et al.*[23] The authors developed "**TOF-probes**", named for their compatibility with time-of-flight detection, targeted four proteases of high relevance to oncology and cell death, namely cathepsin B, cathepsin L, legumain, and neutrophil elastase (Fig. 38). Each of these enzymes plays a distinct and important role in immune signaling, tissue remodeling, or tumor invasion, and all are known to be post-translationally regulated, emphasizing the need for activity-focused detection strategies. The **TOF-probes** were composed of three key modules: (i) a peptide recognition motif optimized through HyCoSuL screening to maximize substrate specificity for each protease; (ii) a covalent electrophilic warhead, either an acyloxymethyl ketone (AOMK) or a diphenylphosphonate ($P(O)(OPh)_2$), ensuring irreversible binding to the active site cysteine or serine residues; and (iii) a DOTA-based chelator that was complexed with a stable lanthanide isotope such as ^{159}Tb, ^{175}Lu, or ^{mix}Gd. This modular architecture ensured high biochemical selectivity, irreversible binding to the active site, and direct compatibility with CyTOF detection. Biochemical and cellular validation demonstrated that each probe retained its enzymatic specificity and activity even after metal conjugation. Importantly, authors showed that these **TOF-probes** could be applied to living PBMCs and cancer cell lines (*e.g.*, HCT-116, MDA-MB-231), enabling high-dimensional detection of functional protease signatures in parallel with phenotypic antibody panels. CyTOF analysis revealed distinct protease activity profiles across immune subsets and tumor subpopulations, offering insights not evident from transcriptomic or protein abundance data alone. Notably, IMC further extended this functional resolution into tissue context, mapping the spatial distribution of active proteases in immune-derived THP-1 cells. This study underscored the innovation and translational potential of integrating small-molecule, covalent ABPs with isotopic barcoding to capture enzymatic activity at single-cell resolution. It proposes a new approach for chemical tool development in the context of high-parameter cytometry. Another example of protease activtiy detection by mass cytometry, although in indirect manner, was proposed by Gärtner *et al.*[192] The authors used **MARS116-Bt** probe targeting active cathepsin G. This ABP features a phosphonate warhead and a biotin moiety, which allows indirect detection *via* metal-labeled anti-biotin antibodies. Applied to primary human PBMCs, **MARS116-Bt** revealed CatG activity in $CD66b^+$ neutrophils and $CD16^+$ NK cells, identifying functional subgroups within these populations.

Although mass cytometry has been demonstrated useful for enzyme activtiy profiling there remains a notable lack of metal-tagged probes for kinase imaging compatible with imaging mass cytometry. Hou *et al.* incorporated a stable lanthanide isotope into a chemical probe for the quantification of Bruton's tyrosine kinase (BTK).[193] Initially, the team attempted to directly conjugate a europium-chelating DOTA group to ibrutinib (a BTK inhibitor), resulting in **Ibt-DOTA-Eu**. However, this probe failed to efficiently enter live cells due to its size and polarity. To overcome this limitation, the authors developed a two-step strategy. First, an azide-modified ibrutinib ($Ibt\text{-}N_3$) was used for covalent labeling of BTK inside live cells, leveraging ibrutinib's cell permeability and target specificity. In the second step, a DBCO-DOTA-Eu reagent was introduced to react bioorthogonally with the azide-labeled BTK *via* strain-promoted azide–alkyne cycloaddition (SPAAC), thereby attaching the europium tag. This design ensured both high specificity for BTK

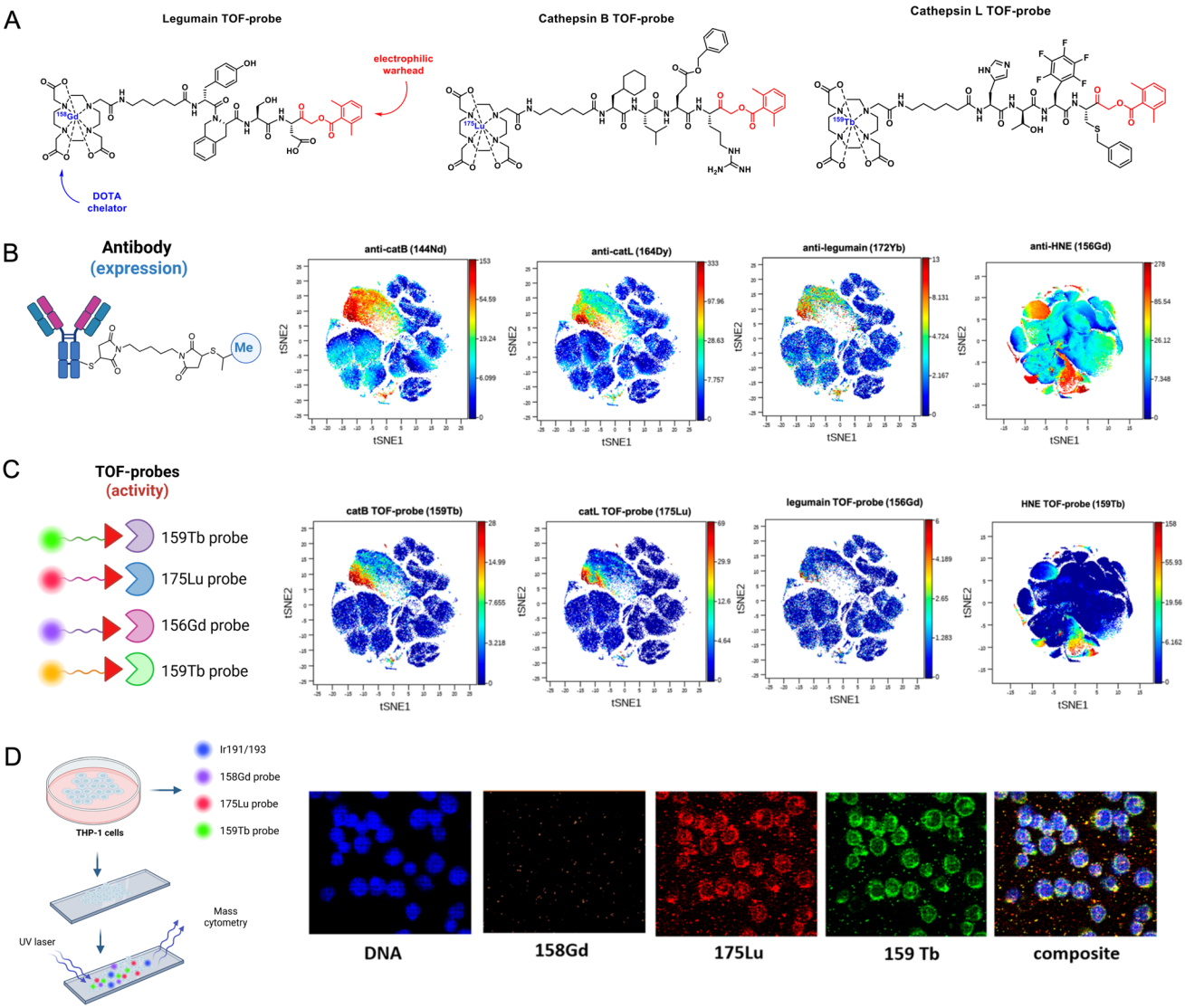

Fig. 38 Mass cytometry-compatible activity-based probes (TOF-probes) for proteases. (A) Chemical structures of the metal-tagged **TOF-probes** designed for legumain, cathepsin B, cathepsin L and neutrophil elastase. (B and C) viSNE analysis of protease expression and activity in human PBMCs. PBMC subsets were delineated based on canonical CD surface markers. To profile both total and active lysosomal proteases, cells were stained with metal-conjugated antibodies and **TOF-probes** specific for the active enzyme forms. While cathepsin L, cathepsin B, and legumain proteins localize predominantly to the CD16^{+} population, only a small fraction of these proteases is detected in their catalytically active state. (D) Spatial distribution of active proteases in THP-1 cells. **TOF-probe** analysis revealed active cathepsin B and cathepsin L within THP-1 cells; no active legumain signal was observed. Adapted with permission from ref. 23 Copyright 2020, American Chemical Society.

and compatibility with live-cell labeling conditions. The SPAAC reaction was optimized to achieve high efficiency and selectivity without disrupting cellular components. For biomedical applications, the europium-labeled BTK was quantified in live cells using ICP-MS, enabling absolute and highly sensitive measurements of kinase levels. Although other strategies for BTK quantification,[194] this method circumvents limitations of fluorescence-based detection, such as spectral overlap and background interference, offering more precise quantification for disease diagnosis and therapeutic monitoring. While Hou *et al.* demonstrated the integration of a stable lanthanide isotope into a kinase-targeting probe, such designs have yet to be fully applied to enzyme activity monitoring *via* mass cytometry or imaging mass cytometry.[193] These advanced techniques offer the potential for multiplexed, spatially resolved analysis of kinase activity in tissues, a highly promising direction. However, further work is needed to optimize probe design for broader *in vivo* application and integration with high-dimensional single-cell analysis platforms. A key challenge is improving cell permeability. This could be addressed by tuning lipophilicity or incorporating transport moieties such as cell-penetrating peptides thereby avoiding the two-step delivery approach described in current work. Kinase-selective probes for mass cytometry are under development in our group.

The integration of chemical probes into CyTOF and IMC workflows marks a transformative advance in single-cell

systems analysis. Looking ahead, several promising directions are emerging. One involves the development of next-generation ABPs with improved cell permeability, enhanced *in vivo* stability, and modular architectures that offer precise control over probe kinetics and signal amplification. Another key area lies in coupling functional probes with high-throughput barcoding strategies and data analysis powered by machine learning will unlock their full diagnostic and prognostic potential. From a clinical perspective, these tools could underpin the next generation of precision diagnostics, enabling simultaneous identification and functional characterization of diseased cells. For instance, mass cytometry panels incorporating activity-based probes for enzymes may help distinguish treatment-resistant cancer clones or reveal early immune dysregulation in autoimmune conditions. As the field moves toward integration with spatial transcriptomics and proteomics, mass cytometry-based chemical tools are poised to become foundational components of the systems biology toolkit.

6.4. Limitations of metal-tagged chemical probes for enzyme imaging

Many enzyme imaging probes employ metal complexes or radioisotopes (*e.g.* gadolinium for MRI, ^{68}Ga or ^{64}Cu for PET, or luminescent lanthanides for optical imaging). A common issue with such metal-chelate probes is their large size and polar charge, which often prevent them from crossing cell membranes. As a result, many metal-based probes are confined to extracellular or vascular spaces, limiting their use for intracellular enzyme targets.[195] For example, Gd(III)-chelate contrast agents cannot readily enter cells, which drastically reduces their utility for imaging processes inside living cells. This limitation has been quantified in MRI probe development: the vast majority of clinically used Gd probes remain outside cells, and efforts to image intracellular events (like enzyme activity in the cytosol) with these agents have failed due to lack of uptake. To overcome this, researchers have designed cell-penetrating versions of metal probes. One strategy is to conjugate the metal chelate to membrane-translocating carriers such as polyarginine peptides or amphipathic molecules. For instance, Endres *et al.* attached a Gd–DTPA complex to an eight-arginine peptide, achieving sufficient cellular uptake for MRI detection.[195] Similarly, "smart" lanthanide luminescent probes have been modified with lipophilic targeting moieties to help them penetrate cells (or localize to specific organelles). These chemical modifications do improve permeability, but they come with trade-offs: added molecular size can affect probe diffusion and clearance, and highly cationic peptides can cause toxicity or nonspecific uptake. Thus, the challenge of delivering metal-based probes into cells remains only partially solved. Ongoing research in nanocarriers, such as enzyme-responsive nanoparticles delivering metal reporters, and in bioorthogonal activation (where a probe is administered as a cell-permeable precursor that chelates the metal only inside the target cells) are promising ways to improve intracellular access. Including quantitative data – for example, reporting membrane permeability or cellular uptake fractions for new probes – will be important in assessing progress on this front. The key point is that metal-based enzyme probes must be engineered with delivery in mind, and permeability limitations need to be explicitly addressed when proposing such probes for live-cell imaging.

7. Theranostics: enzyme-responsive probes for imaging and treatment

7.1. Apoptosis-based theranostics

Theranostic chemical probes that respond to enzymatic activity are emerging as a versatile toolset at the interface of molecular imaging and targeted therapy.[196,197] By linking real-time visualization of disease-related enzymatic processes, orchestrated by proteases, kinases or other enzymes, with site-specific drug release, these systems offer new opportunities for precision medicine.[198] In this section, we highlight representative studies that demonstrate how chemical design, selective targeting, and enzyme-triggered activation can be integrated into probes capable of both diagnosing and treating disease in a coordinated manner. One of the key proteases targeted in theranostic compound development is caspase-3, a central executioner of apoptosis. Because caspase-3 activity directly reflects the induction of programmed cell death, a desired outcome of many anticancer therapies, its activation can be monitored in real time using fluorescent probes, providing a direct and functional readout of therapeutic efficacy.[199,200] In 2015, Li and co-workers reported a modular theranostic platform built to monitor drug release and therapeutic efficacy *via* a dual FRET mechanism.[201] Their construct, termed the **V-prodrug** was designed to be simultaneously responsive to acidic pH and to caspase-3 activity, and was composed of three integrated modules: (1) a pH-sensitive hydrazone linkage connecting doxorubicin (DOX) to a Dabcyl quencher, (2) a peptide substrate DEVD conjugated to a FAM fluorophore, and (3) an RGD peptide for selective targeting of integrin αvβ3-overexpressing tumor cells (Fig. 39). This design enables the sequential activation of the probe: the hydrazone bond is cleaved in the acidic environment of endosomes and lysosomes, releasing DOX and restoring red fluorescence; upon apoptosis induction, caspase-3 cleaves the DEVD sequence, resulting in a second fluorescence readout from FAM. Cellular studies in U-87 MG glioblastoma cells demonstrated robust uptake *via* integrin-mediated endocytosis, as confirmed by a significant reduction in internalization upon competition with free RGD peptide. Confocal microscopy revealed that DOX release preceded FAM activation by approximately two hours, reflecting the expected therapeutic timeline of apoptosis. This sequential activation pattern, in which drug release precedes the apoptotic response, reflects a controlled therapeutic timeline and supports the probe's ability to report on both pharmacokinetics and biological effect with spatial and temporal resolution. Importantly, the dual-readout design allowed real-time assessment of both drug release and downstream biological response within the same cellular system. While conceptually elegant, the authors

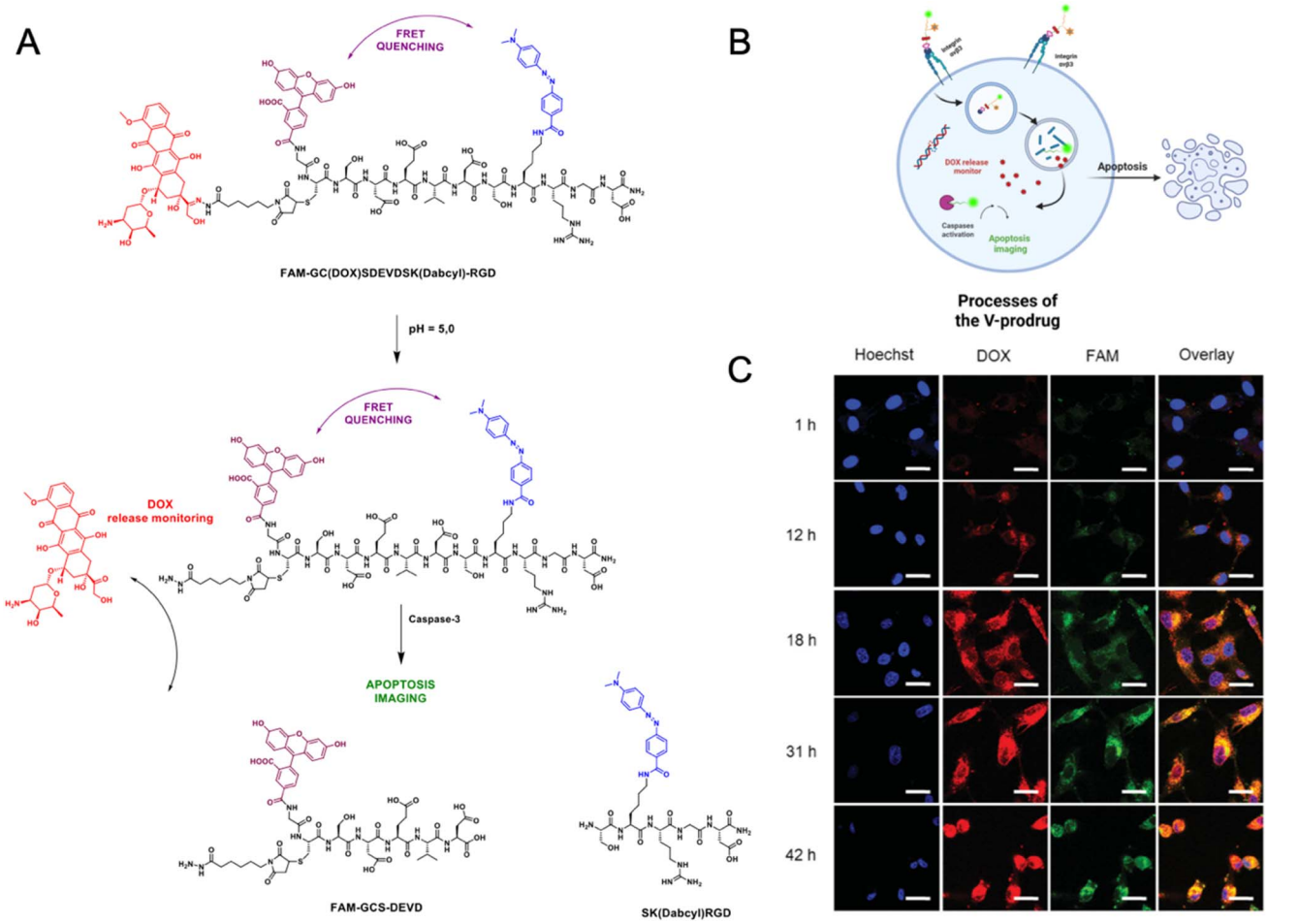

Fig. 39 Chemical structure of the V-prodrug and proposed mechanism of its activation for real-time monitoring of drug release and caspase-3-mediated apoptosis imaging. (A and B) Illustrated steps include: RGD receptor-mediated endocytosis of the **V-prodrug**; acidic pH-triggered cleavage of the hydrazone bond, resulting in doxorubicin (DOX) release and emergence of red fluorescence; DOX-induced apoptosis leading to caspase-3 activation; caspase-3-mediated cleavage of the DEVD peptide sequence; and apoptosis imaging *via* the increase in green fluorescence (FAM). (C) Time-dependent confocal microscopy images of U87 cells treated with the **V-prodrug** for 1, 12, 18, 31, and 42 hours. Cell nuclei are stained with Hoechst 33342 (blue); red fluorescence indicates released doxorubicin (DOX); green fluorescence corresponds to FAM, reporting caspase-3 activity. Adapted with permission from ref. 201 Copyright 2015, WILEY-VCH Verlag GmbH & Co. KGaA, Weinheim.

acknowledged limitations related to hydrazone hydrolysis under systemic conditions and the pharmacological behavior of the FRET components *in vivo*, highlighting the need for improved linker stability and imaging contrast. Extending the concept of caspase-3-responsive prodrug systems beyond signal reporting toward a self-reinforcing therapeutic effect, Chung *et al.* advanced a distinct strategy known as Self-Triggered Apoptosis Enzyme Prodrug Therapy (STAEPT).[202] Their system relied on a prodrug, **RGDEVD-DOX**, incorporating three key features: a tumor-targeting RGD peptide, a caspase-3-cleavable DEVD linker, and a DOX payload linked *via* an ester bond (Fig. 40). The unique aspect of STAEPT lies in its design to exploit apoptotic caspase-3 not only as a biomarker of efficacy but as a mediator of further drug activation. Upon uptake *via* RGD-integrin interaction, the ester bond is hydrolyzed intracellularly, liberating DOX. This initial insult triggers apoptosis and increases intracellular caspase-3 activity. Active caspase-3 is then released extracellularly due to compromised membrane integrity of dying tumor cells, where it cleaves remaining RGDEVD-DOX prodrugs in the tumor microenvironment. This creates a positive feedback loop that amplifies drug activation across both targeted and neighboring non-targeted cells. *In vitro*, the prodrug exhibited potent, caspase-dependent cytotoxicity in U-87 MG cells, with minimal toxicity observed for a scrambled-sequence control lacking the DEVD motif. *In vivo*, STAEPT treatment resulted in over 90% tumor growth inhibition in a U-87 MG xenograft model at doses significantly lower than free DOX, with markedly reduced systemic toxicity. Caspase-3 activity in tumor tissue was elevated over 150-fold, and histological analyses confirmed widespread apoptosis extending beyond the initial RGD-targeted population. This study established the principle that an enzyme product of therapeutic action could be recycled as a propagating agent, opening new avenues for addressing tumor heterogeneity and drug penetration. However, the authors also raised important

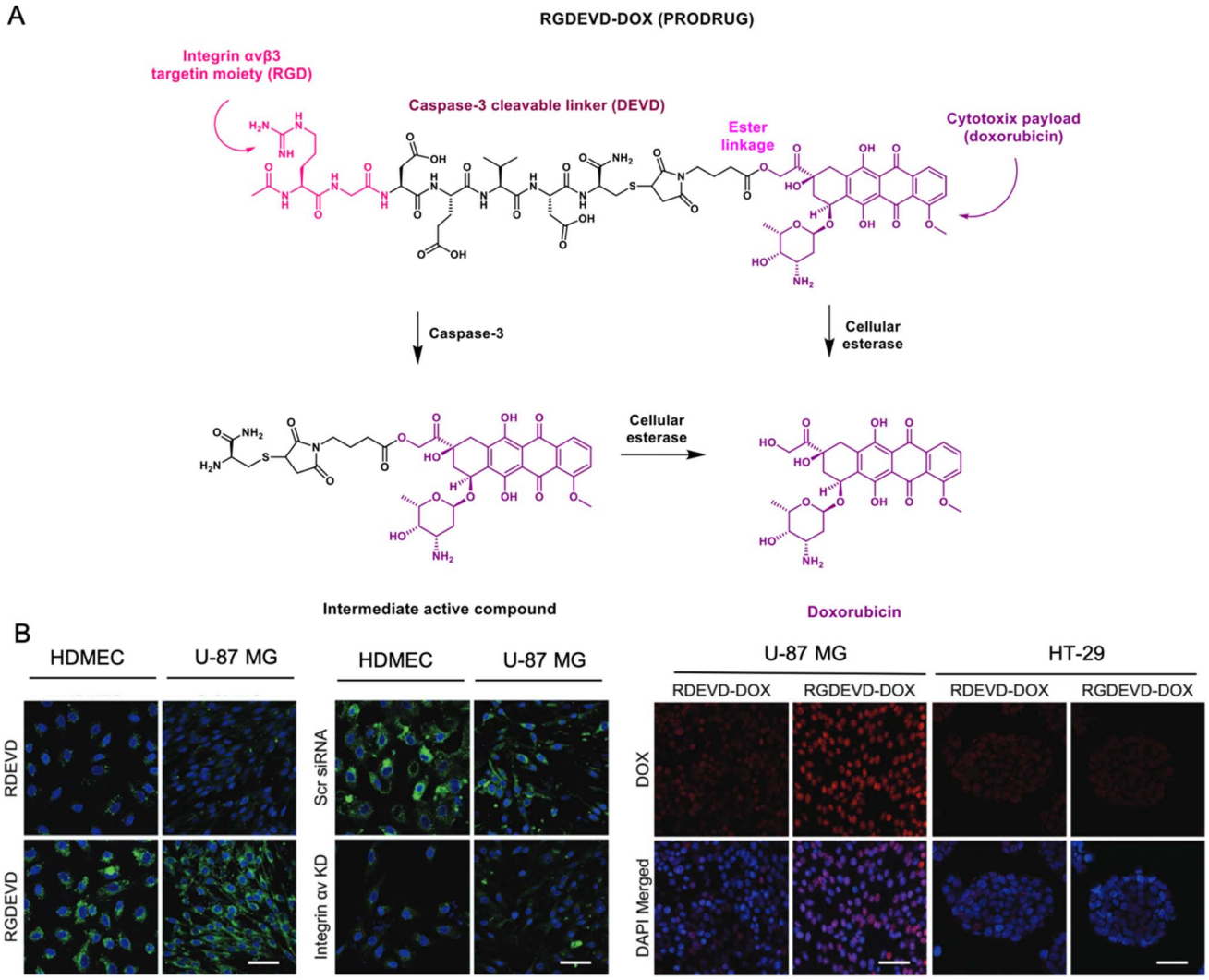

Fig. 40 Design and functional evaluation of the RGDEVD-DOX prodrug. (A) Chemical structure of **RGDEVD-DOX** and its enzymatically released active components. (B) Targeted uptake and cytotoxicity in integrin αvβ3-expressing cells: (i) confocal micrographs of HDMEC and U-87 MG cells incubated with FITC-labeled RDEVD or RGDEVD peptides (green, peptide; blue, nuclei). (ii) Confocal imaging in HDMEC and U-87 MG cells transfected with scrambled control or ITGAV siRNA and treated with **FITC-RGDEVD**, demonstrating integrin αv dependence. (iii) Representative confocal images of U-87 MG and HT-29 cells exposed to **RDEVD-DOX** or **RGDEVD-DOX** (red, doxorubicin fluorescence; blue, nuclei). Adapted with permission from ref. 202 Copyright 2018, The Authors. Published by WILEY-VCH Verlag GmbH & Co. KGaA, Weinheim.

questions regarding potential extracellular off-target proteolysis and the long-term stability of the DEVD linkage in circulation.

7.2. Theranostics activated by lysosomal hydrolases

Galactosidases, particularly β-galactosidase (β-gal), are lysosomal hydrolases that cleave terminal galactoside residues from glycoconjugates and play essential roles in cellular catabolism. Notably, β-gal is frequently overexpressed in a variety of tumors, making it an attractive enzymatic target for cancer-selective imaging and drug delivery strategies.[203,204] This has inspired the development of several β-gal-activated theranostic systems designed to exploit tumor-associated enzymatic activity for site-specific drug release and concurrent molecular readout. In an example of lysosomal enzyme-activated theranostics, Sharma *et al.* developed a β-galactosidase-responsive small-molecule prodrug that couples targeted chemotherapy with fluorescence-based activation monitoring.[197,205] The construct links doxorubicin to a galactopyranoside moiety *via* a self-immolative *p*-aminobenzyl alcohol (PABA) spacer. In its intact form, the prodrug is non-fluorescent and pharmacologically inert under physiological conditions. Upon receptor-mediated uptake *via* the asialoglycoprotein (ASGP) pathway and enzymatic cleavage by intracellular β-galactosidase, the glycosidic bond is hydrolyzed, triggering spontaneous PABA cleavage and doxorubicin release. This cascade simultaneously restores fluorescence emission and activates the cytotoxic payload within β-gal-rich tumor environments. *In vitro*, the probe exhibited selective uptake and toxicity in ASGP-expressing HepG2 and HT-29 cells, with minimal activity in ASGP-deficient HeLa cells. *In vivo*, prodrug-treated HT-29 xenograft-

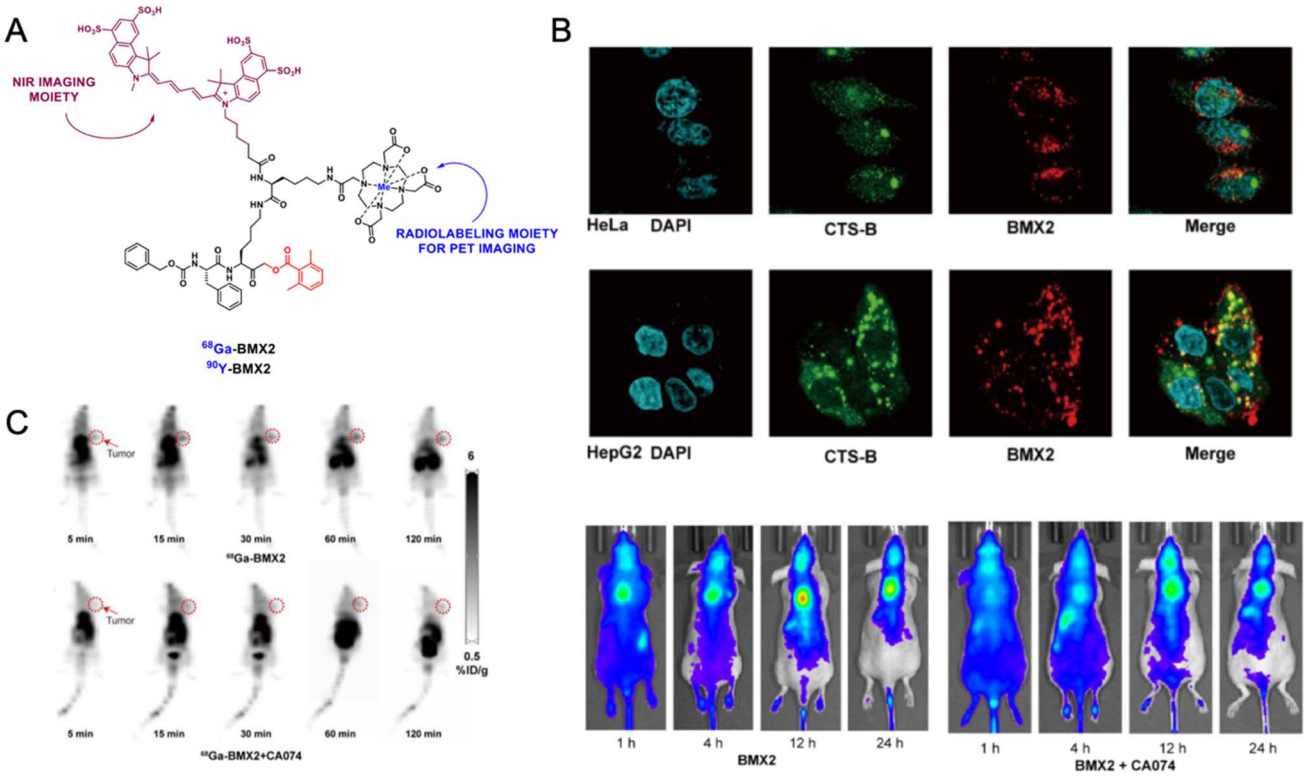

Fig. 41 Example of a lysosomal hydrolase-activated theranostic probe BMX2. (A) Chemical structures of [^{68}Ga]-**BMX2** and [^{90}Y]-**BMX2**. (B) Confocal microscopy of HeLa and HepG2 cells treated with BMX2: DAPI (blue), cathepsin B immunostaining (CTS-B, green), BMX2 fluorescence (red), and merged images. Below, *in vivo* fluorescence imaging and quantification of HeLa xenografts at 1, 4, 12, and 24 h after injection of BMX2 alone or mixed with the cathepsin B inhibitor CA074. (C) PET imaging and quantification of HeLa xenografts following administration of [^{68}Ga]-**BMX2**: (i) dynamic scans at 5, 15, 30, 60, and 120 min post-injection; (ii) 60 min post-injection in mice pretreated with CA074. Adapted with permission from ref. 208 Copyright 2023, The Authors. Published by American Chemical Society.

bearing mice showed significantly enhanced tumor growth inhibition compared to free doxorubicin, alongside localized fluorescence activation within tumors. This elegant design underscores how enzyme-sensitive masking groups and receptor-mediated uptake can be synergistically harnessed to construct activatable theranostic agents that integrate site-specific drug release with molecular-level readouts.

Among other lysosomal hydrolases, cathepsin B, a cysteine protease, is of particular interest due to its role in promoting extracellular matrix degradation, tumor invasion, and metastasis.[206] This biological relevance has inspired numerous cathepsin B responsive drug delivery systems. One such example is the theranostic agent reported by Jin *et al.* designed for targeted delivery of SN38 to folate receptor (FR)-positive tumor cells.[207] Their construct, FA-GFLG-SN38, integrates a folic acid moiety for FR-mediated endocytosis, a cathepsin B-cleavable GFLG peptide linker, and the potent cytotoxic agent SN38. To enable imaging of intracellular drug activation, the authors developed a fluorescent analogue, **FA-GFLG-SN38-Rho**, bearing a rhodamine B dye. The conjugate retained both enzymatic responsiveness and therapeutic activity. Upon uptake into FR-expressing SK-Hep-1, HeLa, and SiHa cells, cathepsin B cleavage within lysosomes released SN38 and restored rhodamine fluorescence predominantly localized to the nucleus. In contrast, FR-negative A549 and normal 16-HBE cells showed minimal fluorescence and reduced cytotoxicity. The prodrug demonstrated excellent plasma stability, with negligible degradation in mouse and human serum, and IC_{50} values of ~2–3 μM in FR-positive cells, compared to ~20 μM in FR-negative controls. These results highlight the potential of this chemically defined system to unify receptor targeting, enzymatic specificity, and real-time imaging in a single small-molecule construct, avoiding the complexity of nanocarriers or cascade amplification strategies.

In another study, Zhou *et al.* reported a multifunctional activity-based probe designed to selectively target cathepsin B.[208] Their chemically compact construct, termed **BMX2**, integrates three functional modules: (1) an acyloxymethyl ketone warhead that irreversibly binds active cathepsin B, (2) a Cy5 fluorophore for near-infrared fluorescence imaging, and (3) a DOTA chelator enabling radiolabeling with either gallium-68 for PET imaging or yttrium-90 for targeted radiotherapy (Fig. 41). Extensive *in vitro* characterization demonstrated the probe's high specificity and potent covalent binding to cathepsin B over related cysteine proteases. In HeLa tumor-bearing mice, both fluorescence and PET imaging confirmed rapid tumor accumulation of **^{68}Ga-BMX**, with prolonged intratumoral retention exceeding 24 hours. This enabled precise

visualization of protease activity within the tumor microenvironment. Biodistribution studies showed minimal uptake in healthy tissues and fast renal clearance, highlighting the probe's favorable safety and pharmacokinetic profile. Importantly, therapeutic administration of **^{90}Y-BMX2** led to significant inhibition of tumor growth compared to controls, while histological analyses revealed minimal off-target tissue damage. These findings validate the dual diagnostic and therapeutic capability of BMX and position it as a promising candidate for protease-targeted radiopharmaceutical therapy. Unlike conventional radiotracers that rely on passive accumulation or receptor binding, BMX is selectively activated by enzymatic cleavage at the tumor site, enabling spatially confined signal amplification and localized radiotherapeutic effect. Its irreversible covalent mechanism and extracellular activation further distinguish it from internalizing prodrugs, opening new possibilities for addressing protease activity in complex or poorly vascularized tumor regions.

7.3. Theranostics for extracellular activation

Another important class of proteases widely expressed in various cancer cells and the tumor microenvironment are matrix metalloproteinases (MMPs), with MMP-2, MMP-9, and MMP-14 being the most prominent targets for therapeutic intervention.[209] Although initially considered attractive molecular targets, MMP inhibitors failed in clinical trials due to issues with selectivity and systemic toxicity.[210,211] As a result, research over the years has shifted toward harnessing MMP activity within theranostic strategies rather than direct inhibition. One promising therapeutic modality that leverages MMP activity is photodynamic therapy (PDT), which has gained considerable attention due to its minimally invasive nature, low systemic toxicity, and reduced potential for drug resistance compared to conventional chemotherapy. However, to fully realize its potential, enzyme-responsive PDT must be carefully tuned to achieve improved selectivity within tumor tissues. In response to these challenges, Tam *et al.* developed a sophisticated double-locked photodynamic molecular beacon (PMB), designed to function as an enzymatically gated AND logic system responsive to two tumor-associated proteases: MMP-2 and cathepsin B (Fig. 42).[212] The probe (**PMB1**) integrates a distyryl boron dipyrromethene (DSBDP)-based photosensitizer and a Black Hole Quencher 3 (BHQ-3) moiety, linked *via* two short peptide sequences: PLGVR (cleavable by extracellular MMP-2) and GFLG (recognized by intracellular cathepsin B). These linkers are embedded within a cyclic peptide architecture derived from a tailor-made linear precursor bearing terminal cysteines and a central azide group, enabling efficient one-pot conjugation and macrocyclization. In the native form, the proximity of the photosensitizer and quencher enables strong FRET, effectively suppressing both fluorescence emission and reactive oxygen species (ROS) generation. Selective activation is achieved through a sequential two-step enzymatic mechanism: MMP-2 first cleaves the PLGVR segment in the extracellular matrix, followed by endocytosis and cathepsin B-mediated hydrolysis of the GFLG linker within lysosomes. Only upon cleavage of both linkers is the DSBDP core fully unmasked, restoring fluorescence and photosensitizing capability upon

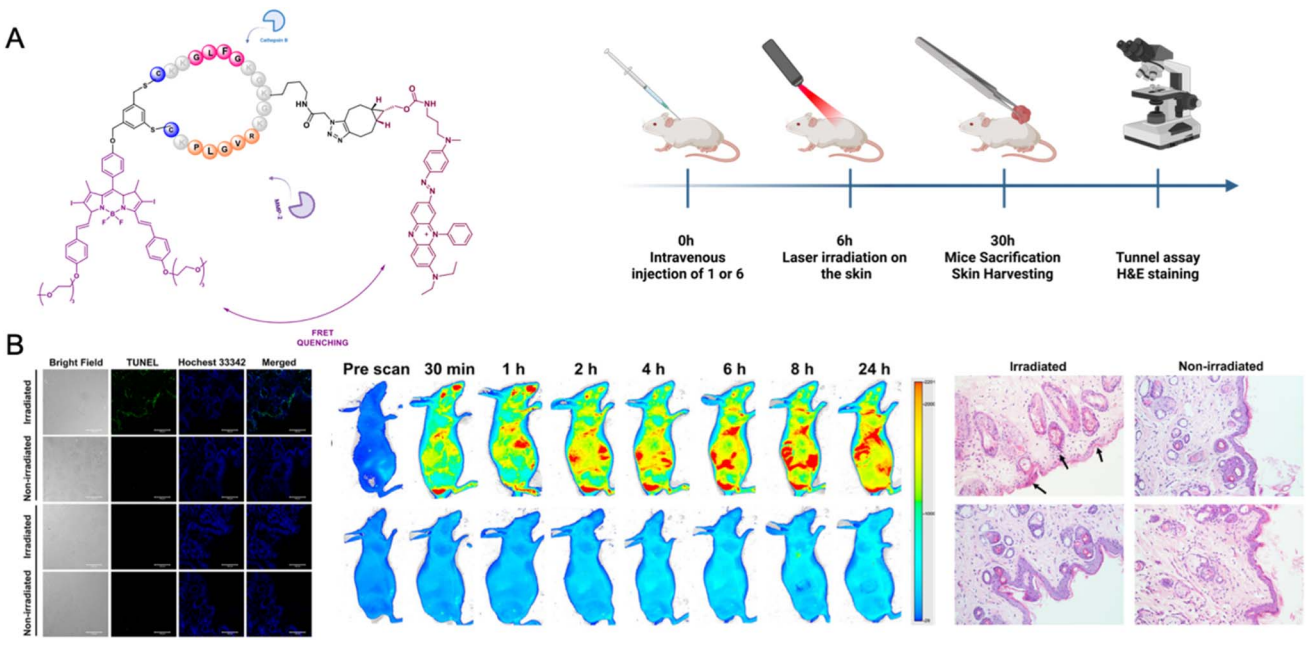

Fig. 42 Photodynamic activation and *in vivo* evaluation of PMB1. (A) Molecular structure of the double-locked **PMB1** and its dual-enzyme activation mechanism, alongside the timeline for *in vivo* photodynamic treatment with compounds **1** and **6** on murine skin. (B) TUNEL staining of mouse skin sections 24 h after treatment; nuclei counterstained with Hoechst 33342. Photographs of nude mice before and 24 h after laser irradiation (680 nm, 0.3 W cm^{-2}, 10 min) administered 6 h post-injection. H&E-stained skin sections 24 h post-treatment (200× original magnification). Adapted with permission from ref. 212 Copyright 2023, The Authors. Published by American Chemical Society.

light irradiation. This dual-protease logic gate strategy offers several advantages over conventional "always-on" PDT agents. *In vitro*, the intact **PMB1** showed negligible cytotoxicity and fluorescence in the absence of enzymatic activation and light, but induced potent cell death in MMP-2- and cathepsin B-positive tumor cells upon dual activation. *In vivo* studies using A549 tumor-bearing mice demonstrated selective tumor accumulation, minimal skin phototoxicity, and significant tumor growth suppression following light exposure. Importantly, histological analysis confirmed minimal damage to healthy tissues, underscoring the spatial precision of the therapy. By combining dual-enzyme responsiveness, cyclic peptide stabilization, and FRET-based quenching into a compact molecular scaffold, this study sets a new benchmark for activatable phototheranostics. The AND-gated activation logic enhances tumor specificity while avoiding premature activation in circulation or healthy tissue. Future directions may involve adapting this platform to alternative enzyme pairs, introducing tunable linkers, or extending the strategy to other photoresponsive modalities. Overall, this work exemplifies how precise protease recognition can be harnessed not only for imaging, but for controlled therapeutic action in complex tumor microenvironments.

Another cancer-associated protease often used as a biomarker for prodrug activation or as an imaging anchor is fibroblast activation protein (FAP). Its selective expression in tumor-associated fibroblasts has driven the development of increasingly advanced probes, particularly those built on the clinically validated FAPI (FAP inhibitor) scaffold, for both imaging and therapeutic applications.[213–215] While earlier generations such as FAPI-based demonstrated promising pharmacokinetics and tumor uptake, their design relied primarily on irreversible inhibition and did not fully exploit the enzymatic specificity of FAP.[215] This limitation has spurred efforts to create hybrid tracers that combine structural binding elements with substrate-based features, thereby enhancing both affinity and functional responsiveness. In a 2023 study, Lai *et al.* advanced this concept by introducing **^{68}Ga-DOTA-GPFAPI-04**, a radiotracer optimized for glioblastoma imaging through a dual-mode strategy that merges substrate mimicry with high-affinity inhibition.[216] The probe integrates a quinoline-based FAP inhibitor with a Gly-Pro dipeptide, FAP's canonical substrate, and a DOTA chelator for radiometal labeling. This hybrid architecture significantly improved both target binding and tumor retention. In orthotopic glioblastoma models, the Gly-Pro-modified tracer outperformed FAPI-04, yielding more than a threefold increase in tumor uptake and sustained retention exceeding 24 hours. The tumor-to-muscle ratio surpassed 9, confirming high contrast and specificity. What distinguishes this work is not only its performance metrics but the conceptual innovation: the authors exploit enzymatic preferences of FAP to stabilize probe–enzyme interactions without compromising binding strength. This subtle shift toward substrate-informed binding opens possibilities for designing activatable, cleavable, or even therapeutic derivatives. Particularly in glioblastoma where dense stroma, infiltrative growth, and poor drug penetration remain major hurdles such an approach may improve both delivery and diagnostic resolution. By uniting irreversible inhibition with enzymatic mimicry in a chemically compact scaffold, Lai *et al.* offer a new blueprint for FAP-targeted imaging agents that are biologically coherent, synthetically accessible, and translationally promising.

Building on the strategy of targeting fibroblast activation protein for cancer theranostics, Feng *et al.* developed a next-generation tracer that enhances tumor retention not through enzymatic activation, but by improving systemic pharmacokinetics (Fig. 43A).[217] Their design, DOTA-FAPI-maleimide, retains the FAPI-04 scaffold, a quinoline-based FAP inhibitor, but introduces a maleimide group capable of forming covalent bonds with circulating serum albumin. This simple chemical modification enables *in situ* albumin binding, significantly extending blood circulation time and increasing tumor exposure. Radiolabeled with gallium-68 or lutetium-177, the probe demonstrated excellent stability, high labeling efficiency (>99%), and favorable tumor targeting. PET/CT imaging in xenograft models showed prolonged tumor accumulation and minimal off-target distribution. Remarkably, ^{177}Lu-DOTA-FAPI-maleimide maintained strong tumor retention for up to 144 hours post-injection, achieving sustained therapeutic exposure with low systemic toxicity. *In vitro* studies confirmed high binding affinity (K_D ~0.3 nM) and improved receptor density engagement compared to earlier FAPI analogs. Although this system does not depend on protease-mediated cleavage for activation, it remains highly relevant to the field of protease-targeted theranostics. It underscores how modifying pharmacokinetics-by extending circulation and retention of protease-targeting ligands can significantly amplify therapeutic impact. This broadens the definition of enzyme-based theranostics beyond catalytically activated systems, showing that proteases can also be exploited as stable, disease-specific docking points in chemically engineered delivery platforms.

In a 2025 Meng *et al.* introduced FSND3, a novel FAP-targeted radiotracer designed to optimize both imaging performance and clinical adaptability (Fig. 43B).[218] The molecule integrates a FAPI-based targeting core with a DOTA chelator and a tri-Asp peptide linker, engineered to fine-tune pharmacokinetics and reduce off-target interactions. Beyond passive modulation of circulation, the aspartate-rich spacer appears to contribute to enhanced FAP-binding stability, potentially *via* secondary interactions with the active site. Preclinical PET imaging with **^{68}Ga-FSND3** and **^{18}F-AlF-FSND3** demonstrated high tumor uptake, rapid clearance from non-target tissues, and improved tumor-to-background contrast compared to earlier FAPI analogs. Particularly in orthotopic pancreatic and lung cancer models, the tracer enabled high-resolution delineation of lesions, even at delayed timepoints, highlighting its utility for detecting small or deep-seated tumors. In human pilot studies, both isotopologs outperformed ^{18}F-FDG in selected clinical scenarios, reinforcing their diagnostic potential. Although primarily explored for PET imaging, the DOTA-based architecture of FSND3 positions it as a chemically versatile theranostic platform. Its favorable retention, high FAP selectivity, and compatibility with β- or α-emitting radionuclides (*e.g.*, ^{177}Lu, ^{225}Ac) make it well-suited for future adaptation into

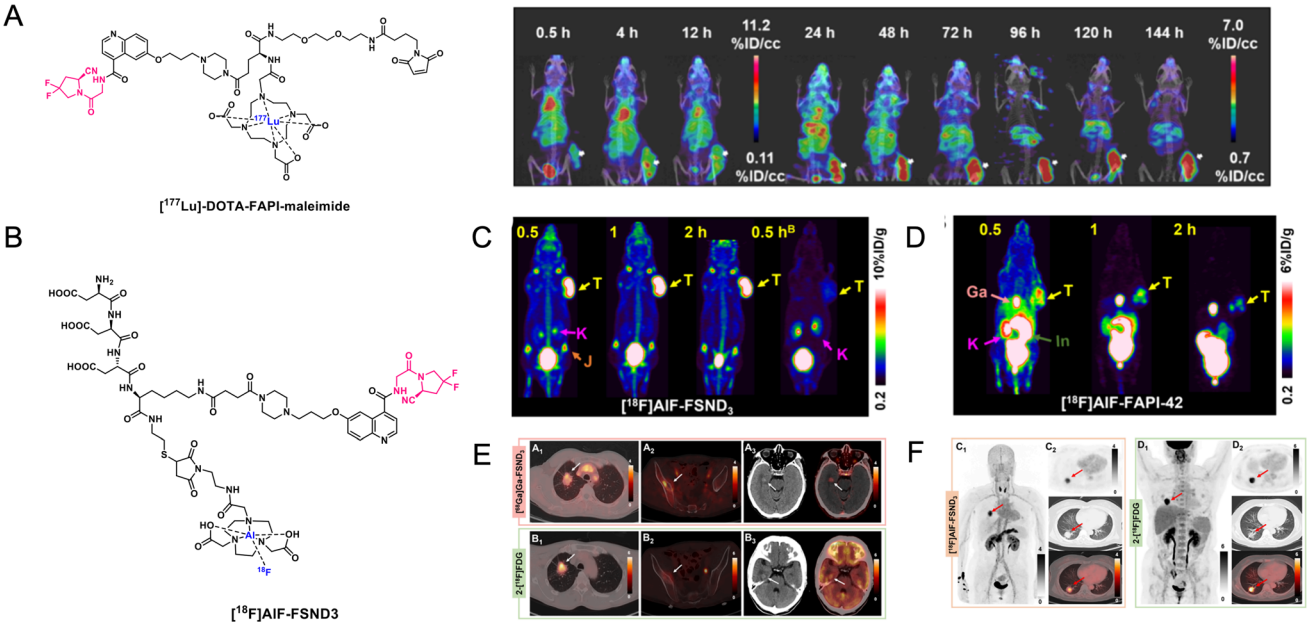

Fig. 43 The structure and applications of FAP PET theranostic probes. (A) Chemical structure of the [^{177}Lu]Lu-DOTA-FAPI-maleimide probe. Representative SPECT/CT fusion images depicting the biodistribution of [^{177}Lu]Lu-DOTA-FAPI-maleimide in tumor mice bearing HT-1080-FAP. Adapted with permission from ref. 217 Copyright © 2024 American Chemical Society. (B) Chemical structure of the [^{18}F]-AlF-FSND3. (C and D) PET imaging of [^{18}F]AlF-FSND3 (C) and [^{18}F]AlF-FAPI-42 (D) in HT-1080-FAP tumor-bearing mice. (E and F) Comparative PET imaging of lung adenocarcinoma with [^{68}Ga]Ga-FSND3 and 2-[^{18}F]FDG. In a 67-year-old male, both radiotracers localize to the primary pulmonary lesion and skeletal metastasis, while [^{68}Ga]Ga-FSND3 affords superior contrast for the cerebral metastasis (E). In a 55-year-old female, [^{18}F]AlF-FSND3 and 2-[^{18}F]FDG similarly delineate the right lung tumor (F). Adapted with permission from ref. 218 Copyright 2025, American Chemical Society.

radiotherapeutic formulations. In this context, FSND3 exemplifies a next-generation scaffold that bridges molecular imaging and targeted radiotherapy through rational linker design and pharmacokinetic engineering.

7.4. Theranostics for immunotherapies

In addition to broadly expressed cancer-associated proteases such as cathepsin B, FAP, and MMPs, other proteases with more specialized roles, such as granzyme B, which is activated during immune responses against tumors, can also be harnessed for biomedical applications. These immune-associated proteases offer unique opportunities for theranostic strategies aimed at monitoring or enhancing cancer immunotherapy. In one of such approach, Xie *et al.* developed an innovative theranostic probe designed to visualize immune cell activity in CAR-T cell therapy and checkpoint blockade by tracking the enzymatic activity of granzyme B.[219] Granzyme B is a serine protease secreted by cytotoxic T lymphocytes and natural killer (NK) cells, playing a crucial role in immune-mediated cell death by cleaving intracellular substrates to trigger apoptosis in target cells.[220,221] Their probe, named **G-SNAT-Cy5**, employed Target-Enabled *in situ* Ligand Aggregation (TESLA) technology, enabling selective enzymatic activation and subsequent nanoaggregation (Fig. 44). Structurally, the G-SNAT probe integrated a granzyme B substrate peptide (IEFD), a cyanopyrimidine moiety, a cysteine residue, and a Cy5 fluorophore. Upon cleavage of the IEFD substrate by granzyme B and subsequent disulfide reduction, the probe underwent intramolecular cyclization followed by local aggregation, producing a spatially confined fluorescent signal at the site of immune activity. Unlike conventional granzyme B reporters, **G-SNAT-Cy5** provides spatially confined signal amplification without requiring genetic manipulation or external substrates. This feature makes it particularly well suited for clinical translation and for use in heterogeneous tumor environments. In lymphoma-bearing mouse models, the probe enabled early and accurate assessment of therapeutic efficacy in both CAR-T and anti-PD-L1 immunotherapy, with imaging results correlating strongly with treatment response. The successful demonstration of this platform underscores the potential of protease-activated nanoaggregation as a strategy for real-time, noninvasive immune monitoring in precision oncology.

7.5. Protease-cleavable linkers as an approach to theranostic strategy

Protease-cleavable linkers are a key element of chemically defined theranostic systems, enabling spatially controlled drug release in response to tumor-associated enzymatic activity.[222,223] When combined with high-affinity targeting ligands, such as receptor-binding peptides, this strategy offers a powerful means to enhance both therapeutic selectivity and diagnostic precision. Among the most important targets in this context is integrin αvβ6, a tumor-specific cell surface receptor with minimal expression in healthy adult tissues.[224] In 2023 Davis *et al.* developed a peptide-drug conjugate (PDC) that combines αvβ6-targeted delivery, protease-mediated activation, and PET

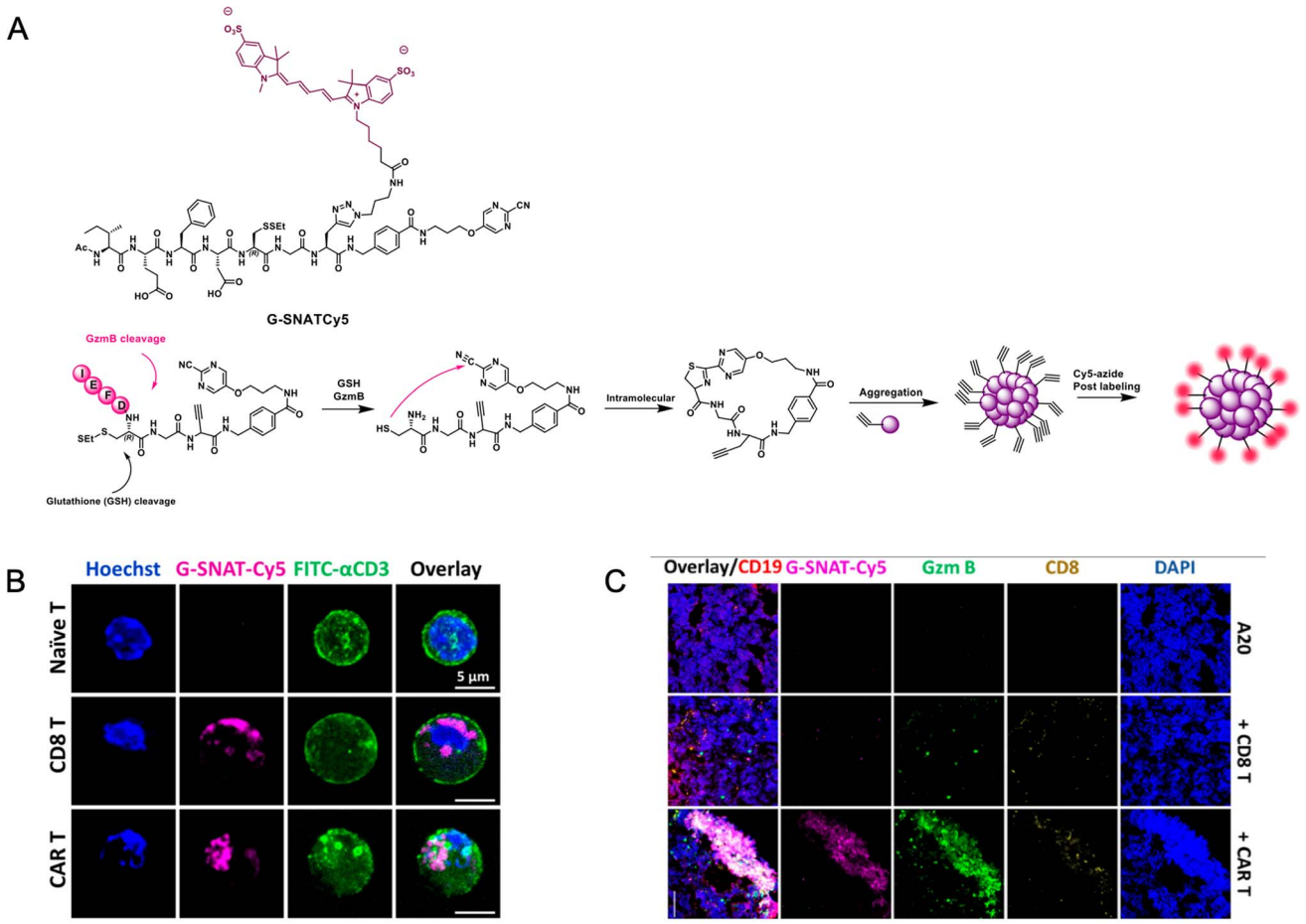

Fig. 44 The structure and application of granzyme B theranostic probes. (A) Illustration of the G-SNAT-Cy5 probe and post-click labeling of granzyme B activated G-SNAT (B) Microscopic imaging of T cells incubated with **G-SNAT-Cy5** and then stained with Hoechst (blue) and FITC conjugated CD3 antibody (green). Magenta represents retained **G-SNAT-Cy5**. (C) Multimodal optical imaging with **G-SNAT-Cy5** and D-luciferin predicts lymphoid tumor response to CAR T-cell therapy. Immunofluorescence staining analysis of the tumors. Adapted with permission from ref. 219 Copyright 2022, The Authors. Published by American Chemical Society.

imaging within a single small-molecule construct.[225] The system incorporates a high-affinity integrin-binding peptide (αvβ6-BP) linked to monomethyl auristatin E (MMAE) *via* a cathepsin-sensitive Val-Cit-PABC linker and is functionalized with a DOTA chelator for copper-64 radiolabeling. This design enables both selective cytotoxicity in αvβ6-expressing tumors and real-time imaging of drug distribution. *In vitro* assays confirmed integrin-dependent binding and internalization, with no significant off-target toxicity in αvβ6-negative lines. The conjugate exhibited high plasma stability and clear protease responsiveness. *In vivo*, PET/CT imaging showed strong and selective tumor accumulation in melanoma and pancreatic cancer xenografts, with favorable pharmacokinetics dominated by renal clearance. Therapeutically, the unlabeled conjugate significantly prolonged survival in αvβ6-positive tumor bearing mice. Beyond its current formulation, this platform offers a compelling chemical foundation for further refinement. The use of protease-cleavable linkers can be extended to alternative enzymatic triggers, while the integrin-binding motif itself may be chemically tuned for enhanced selectivity or altered pharmacokinetics. Notably, substitution of natural amino acids in the peptide domain with D-amino acids, β-amino acids, or constrained residues could improve serum stability and reduce recognition by off-target proteases. Furthermore, introducing orthogonal protease substrates specific to tumor type or disease stage may enable switchable payload release across heterogeneous microenvironments. The construct's compatibility with radiometal chelators also opens the possibility of pairing therapeutic and diagnostic isotopes within a single scaffold. As such, this work represents more than a single theranostic agent it outlines a chemically adaptable and clinically promising platform for next-generation enzyme-responsive PDCs.

Recent advances in enzyme-responsive theranostic probes demonstrate the feasibility of chemically defined small-molecule systems that unite diagnostic precision with spatially controlled therapeutic activation.[226] These constructs capitalize on the local activity of tumor-associated proteases, lysosomal hydrolases, and immune effectors to enable conditional drug release and real-time imaging without relying on nanoparticles. The most promising designs, such as protease-

cleavable peptide-drug conjugates with radiometal chelators or self-amplifying caspase-sensitive prodrugs, successfully integrate targeting, activation, and therapeutic efficacy in a clinically scalable format. However, the field remains constrained by challenges in linker stability, *in vivo* enzymatic selectivity, and regulatory concerns related to switchable systems. Scientifically, future progress will depend less on expanding probe diversity and more on developing modular, pharmacokinetically optimized platforms that respond to combinatorial enzyme signals. In particular, theranostics enabling dynamic feedback between drug action and molecular imaging, especially in immunotherapy or neurodegeneration, are poised to redefine how we track and treat disease. To translate this potential into clinical practice, the focus must shift toward predictive *in vivo* validation, metabolic profiling, and cross-indication applicability of chemically tunable scaffolds.

8. AI in the design of enzyme-targeted chemical probes

Recent advances in artificial intelligence (AI) and machine learning (ML) may have a considerable impact on the field of chemical biology, by offering transformative capabilities in the design of small-molecule probes for enzymatic targets. Central to these developments is the ability of AI to model enzyme structures with high accuracy, even in the absence of experimental crystallographic data. Tools like AlphaFold and RoseTTAFold provide predictive 3D models that reveal the architecture of enzyme active sites, conformational states, and potential ligand-binding pockets, greatly accelerating structure-based design.[227,228] These structural insights form the foundation for several classes of AI-enabled probe design approaches. In structure-based design, AI-derived enzyme models are used to guide docking campaigns of large compound libraries, either experimentally derived or virtually generated.

Platforms such as RosettaVS integrate receptor flexibility into docking algorithms, allowing more accurate pose prediction and affinity scoring. In one of such studies, Zhou *et al.* used RosettaVS to screen billions of compounds against the E3 ligase KLHDC2 and the sodium channel Nav1.7, ultimately identifying hit compounds with low micromolar potency.[229] While these targets were not enzymes *per se*, the approach is directly transferable to proteases and kinases, especially when validated enzyme structures or AlphaFold predictions are available. AI also plays a central role in ligand generation through *de novo* design. Generative models, including variational autoencoders, generative adversarial networks (GANs), and diffusion models, can propose novel molecular scaffolds optimized for binding, reactivity, or other user-defined properties. Chemistry42, a deep learning platform developed by Insilico Medicine, exemplifies this approach. In a study by Ren *et al.*, the platform was applied to cyclin-dependent kinase 20 (CDK20), a dark kinase lacking experimental structure.[230] Using AlphaFold predictions as structural input, Chemistry42 generated over 8900 virtual compounds, of which seven were synthesized and tested. One yielded a hit with a dissociation constant of 9.2 μM. Subsequent AI-driven optimization led to a nanomolar-range inhibitor (IC_{50} ≈ 33 nM) with selective activity in CDK20-overexpressing hepatocellular carcinoma cells. This study demonstrates the full pipeline from target selection to chemical probe generation using AI technologies. Proteases, especially those involved in cancer and infectious diseases, have also benefited from AI-assisted probe design. During the COVID-19 pandemic, rapid inhibitor development against SARS-CoV-2 main protease (M^{pro}) provided an ideal test case. Joshi *et al.* used a deep-learning pipeline to start from known scaffolds and systematically introduce linkers and electrophilic warheads.[231] This led to the discovery of several chloroacetamide-based covalent inhibitors, with K_i values around 5 μM. The predictions were validated through native mass spectrometry, FRET-based activity assays, and X-ray crystallography, confirming that predicted binding poses matched the experimentally determined structures. A related study by Elend *et al.*[232] combined neural network-based molecular generation with molecular dynamics filtering to identify two promising M^{pro} binders from a virtual library of 140 000 compounds. AI has also shown utility in designing both the warhead and the reporter moieties of probes. For instance, Xiang *et al.* developed a cathepsin-responsive, pH-activatable silicon-rhodamine (SiR) probe by training an ML model on xanthene fluorophore derivatives.[233] The final construct, **SiR-CTS-pH**, was highly specific for acidic, cathepsin-rich tumor compartments and demonstrated superior signal-to-background ratios in murine models of liver cancer. The probe's dual-activation mechanism, protease cleavage and acidic environment, was explicitly tuned *via* AI-guided optimization of the fluorophore's pK_a and linker design. This work underscores how AI can fine-tune both enzyme selectivity and imaging properties in a rational manner. Beyond direct structure-based design, AI approaches also include ligand–target interaction prediction using quantitative structure–activity relationship (QSAR) models. These methods use molecular descriptors, fingerprints, or deep neural networks to predict binding affinities and enzyme inhibition based solely on compound features. Kumar *et al.* developed a machine learning-based QSAR tool for monoamine oxidase B (MAO-B),[234] achieving high correlation between predicted and experimental activity (R^2 ~0.98). While this model was not experimentally validated in their study, it illustrates how large-scale virtual screening of probe candidates can be filtered for high-likelihood binders before synthesis.

The ability to generalize these AI tools across enzyme classes is one of their greatest strengths. Proteases such as cathepsins and matrix metalloproteinases (MMPs), kinases like CDK20, oxidoreductases, glycosidases, and hydrolases are all amenable to AI-guided probe design. For kinases, large datasets from KINOMEscan or other screening platforms enable training of models to predict selectivity and potency across the kinome. These models can be paired with generative frameworks to design ATP-competitive inhibitors or fluorescent tracers. For less well-characterized enzyme classes such as glycosidases or dehydrogenases, AI can assist in substrate optimization by predicting turnover rates, enzyme specificity, or preferred binding interactions, especially when integrated with structural

modeling. Validation remains a crucial step in establishing the biological relevance of AI-designed probes. *In vitro* assays, such as IC_{50} or K_i determination, confirm target engagement and potency. Native mass spectrometry and gel-based assays can detect covalent labeling, particularly for activity-based probes. Cell-based assays, including fluorescence microscopy, allow functional assessment of activatable probes in biologically relevant environments. For instance, Ren *et al.*'s CDK20 inhibitor showed selective growth inhibition in CDK20-expressing cancer cells, while Xiang *et al.*'s **SiR-CTS-pH** probe produced bright fluorescence only in cathepsin-active, acidic compartments,[230,233] *In vivo* imaging studies, using either optical or PET modalities, further validate biodistribution, selectivity, and probe activation. While some examples, such as ^{18}F-JW199 for NCEH1 imaging, were not designed using AI, they highlight the type of preclinical endpoints AI-generated probes must eventually meet. Taken together, these developments illustrate the growing maturity of AI tools in chemical biology. They enable end-to-end probe discovery pipelines, from structural modeling and ligand generation to experimental validation. As generative models become more sophisticated and structural predictions more accurate, it is foreseeable that personalized, disease-specific probes could be designed in a matter of weeks. This opens new possibilities not only for fundamental enzymology but also for diagnostics, imaging, and targeted therapy.

Despite the promising advances described above, current AI-driven probe design approaches have several limitations that must be acknowledged. Many AI models rely on training data derived from experimentally determined structures or known ligand–target interactions, which can introduce bias and limit generalizability. Notably, structure prediction tools like AlphaFold yield static models and may not capture dynamic enzyme conformations or induced-fit changes. For example, AlphaFold often predicts a single ground-state structure; in the case of hexokinase, its prediction aligned with the ligand-free open conformation, failing to reflect the closed form that occurs upon sugar binding. Such omissions highlight that AI models are only as good as the data and assumptions they are built on. Enzymes with few known homologs or those requiring cofactors and partners can still be challenging for AI. Likewise, AI-based quantitative structure–activity relationship (QSAR) models can achieve impressive correlation on test data (*e.g.* $R^2 \sim 0.98$ in a monoamine oxidase B inhibitor model) but may overfit or mispredict outside the chemical space of the training set, especially if experimental data are limited or biased.[234] In general, AI predictions should be treated as hypotheses: high-confidence rankings or designs that still require experimental validation due to these inherent uncertainties. Another critical limitation is the synthesizability of AI-designed molecules. Generative models, such as VAEs, GANs, diffusion models, can propose novel structures optimized *in silico* for binding or fluorescence, but many of these virtual compounds may be impractical to make with real-world chemistry. Early AI-driven designs sometimes yielded molecules that, while conceptually interesting, had no clear synthetic route or contained unusual functionalities. This points to a gap between virtual design and wet-lab reality: insufficient verification of whether candidate probes can actually be synthesized and scaled. Additionally, purely *in silico* libraries often explore an immense chemical space unconstrained by synthetic rules, leading to compounds with ideal predicted properties but low synthetic accessibility. This challenge is exemplified by cases where AI-suggested inhibitors had excellent docked poses or QSAR scores but turned out to require multi-step syntheses with poor yield or unavailable starting materials (a fact sometimes revealed only after medicinal chemists attempt the synthesis). Such outcomes can slow down probe development significantly.

Researchers are actively developing solutions to bridge this gap and make AI proposals more realistic. One approach is to integrate synthesizability filters or constraints into the design process. For instance, in 2024 de Oliveira *et al.* introduced an AI platform called NeuralGenThesis (NGT) that limits generation to a defined ultralarge virtual library of readily synthesizable compounds.[235] By training on a database of trillions of commercially available building-block combinations, their generative model inherently guarantees any predicted hit can be made *via* known chemistry. In a proof-of-concept, NGT was able to discover nanomolar inhibitors from a 3-trillion compound space while ensuring each candidate was within reach of current synthetic methods. In parallel, Guo and Schwaller demonstrated that one can explicitly optimize for synthesizability during *de novo* molecule generation by coupling a generative model with an AI-driven retrosynthesis engine.[236] Their system uses a neural network to propose compounds for a given target, then immediately checks each structure with a retrosynthetic model; only molecules with a viable synthetic route (as determined by the AI chemist) are kept and refined. Impressively, this approach allowed the design of drug-like molecules satisfying multiple property criteria and having confirmed synthetic pathways in a single computational loop. These examples illustrate potential solutions: either constrain AI designs to synthesizable chemical space or employ post-design synthetic pathway prediction to filter out intractable structures. Going forward, many groups are also incorporating heuristic metrics of synthetic accessibility (SA scores) and fragment-based assembly techniques to ensure that generated probes are not only potent on the computer but also attainable in the lab. This convergence of generative design with automated retrosynthesis and reaction prediction is expected to markedly improve the real-life hit rate of AI-designed chemical probes.

9. Conclusions

The field of enzyme-targeted chemical probes has undergone a rapid evolution from fundamental biochemical tools to clinically relevant imaging agents and therapeutic modulators. Proteases and kinases, as two of the most widely studied enzyme families, illustrate how deep biochemical understanding and technological innovation can converge to create impactful diagnostic and therapeutic solutions. Kinase-directed probes, often derived from clinically approved inhibitor scaffolds, have benefited from a well-defined pharmacological space and serve as both imaging agents and pharmacodynamic

biomarkers in oncology and inflammatory diseases. In parallel, protease probes, frequently developed through substrate specificity profiling and enriched with unnatural amino acids, have demonstrated exceptional selectivity and modularity. Their successful application in both preclinical and clinical imaging highlights the power of rational probe design to detect disease states and monitor therapeutic response. Importantly, the versatility of enzyme-responsive probes now extends beyond conventional fluorescence-based detection. The integration of metal isotopes for PET and mass cytometry has enabled high-resolution and multiplexed analysis of enzyme activity across tissues, while paving the way for theranostic approaches that combine diagnostic readouts with therapeutic functions. These innovations not only expand the functional capabilities of chemical probes but also offer new routes for personalized medicine and non-invasive treatment monitoring. Artificial intelligence is poised to further accelerate this progress. Beyond its growing role in target modeling and ligand generation, AI holds promise for improving the design of probes with optimized biological properties, such as metabolic stability, *in vivo* retention, off-target profiles, and clearance routes. By enabling more accurate prediction of pharmacokinetics and tissue distribution, AI-assisted workflows can help close the gap between probe discovery and clinical translation. Looking ahead, continued integration of synthetic chemistry, computational modeling, biological validation, and clinical insight will be essential for translating next-generation enzyme probes into precision tools for diagnostics and therapy. The success of several probe systems in early-phase clinical trials underscores the translational momentum of this field and reaffirms the role of chemical biology as a cornerstone of innovation in biomedical research.

Author contributions

J. N., M. Z., and M. P. wrote the manuscript.

Conflicts of interest

The authors declare no conflicts of interests.

Data availability

No primary research results, software or code have been included and no new data were generated or analyzed as part of this review.

Acknowledgements

This work was supported by the National Science Centre in Poland, under grants OPUS 2022/47/B/NZ5/02405 and OPUS-LAP 2020/39/I/NZ5/03104 awarded to M. P.

References

1 A. G. McDonald and K. F. Tipton, *FEBS J.*, 2023, **290**, 2214–2231.
2 C. Lopez-Otin and J. S. Bond, *J. Biol. Chem.*, 2008, **283**, 30433–30437.
3 J. S. Bond, *J. Biol. Chem.*, 2019, **294**, 1643–1651.
4 D. Fabbro, S. W. Cowan-Jacob and H. Moebitz, *Br. J. Pharmacol.*, 2015, **172**, 2675–2700.
5 J. Rauch, N. Volinsky, D. Romano and W. Kolch, *Cell Commun. Signaling*, 2011, **9**, 23.
6 J. G. Robertson, *Curr. Opin. Struct. Biol.*, 2007, **17**, 674–679.
7 K. S. Bhullar, N. O. Lagaron, E. M. McGowan, I. Parmar, A. Jha, B. P. Hubbard and H. P. V. Rupasinghe, *Mol. Cancer*, 2018, **17**, 48.
8 M. Garland, J. J. Yim and M. Bogyo, *Cell Chem. Biol.*, 2016, **23**, 122–136.
9 J. Vandooren, N. Geurts, E. Martens, P. E. Van den Steen and G. Opdenakker, *Nat. Methods*, 2013, **10**, 211–220.
10 M. Zmudzinski, O. Malon, M. Poreba and M. Drag, *Curr. Opin. Chem. Biol.*, 2023, **74**, 102299.
11 S. Gallagher and D. Chakavarti, *J. Visualized Exp.*, 2008, **16**, e759.
12 B. F. Cravatt, A. T. Wright and J. W. Kozarich, *Annu. Rev. Biochem.*, 2008, **77**, 383–414.
13 A. E. Speers and B. F. Cravatt, *Curr. Protoc. Chem. Biol.*, 2009, **1**, 29–41.
14 L. E. Sanman and M. Bogyo, *Annu. Rev. Biochem.*, 2014, **83**, 249–273.
15 H. Fang, B. Peng, S. Y. Ong, Q. Wu, L. Li and S. Q. Yao, *Chem. Sci.*, 2021, **12**, 8288–8310.
16 U. Mahmood, C. H. Tung, A. Bogdanov Jr and R. Weissleder, *Radiology*, 1999, **213**, 866–870.
17 X. Wu, R. Wang, N. Kwon, H. Ma and J. Yoon, *Chem. Soc. Rev.*, 2022, **51**, 450–463.
18 J. Zhao, T. Ma, B. Chang and J. Fang, *Molecules*, 2022, **27**, 5922.
19 B. P. Rempel, E. W. Price and C. P. Phenix, *Mol. Imaging*, 2017, **16**, 1536012117717852.
20 D. V. Hingorani, B. Yoo, A. S. Bernstein and M. D. Pagel, *Chemistry*, 2014, **20**, 9840–9850.
21 P. Yue, T. Nagendraraj, G. Wang, Z. Jin and G. Angelovski, *Chem. Sci.*, 2024, **15**, 20122–20154.
22 L. J. Edgar, R. N. Vellanki, A. Halupa, D. Hedley, B. G. Wouters and M. Nitz, *Angew Chem. Int. Ed. Engl.*, 2014, **53**, 11473–11477.
23 M. Poreba, K. M. Groborz, W. Rut, M. Pore, S. J. Snipas, M. Vizovisek, B. Turk, P. Kuhn, M. Drag and G. S. Salvesen, *J. Am. Chem. Soc.*, 2020, **142**, 16704–16715.
24 M. Rodriguez-Rios, A. Megia-Fernandez, D. J. Norman and M. Bradley, *Chem. Soc. Rev.*, 2022, **51**, 2081–2120.
25 C. Zambaldo, K. K. Sadhu, G. Karthikeyan, S. Barluenga, J.-P. Daguer and N. Wissinger, *Chem. Sci.*, 2013, **4**, 2088–2093.
26 M. Poreba, K. Groborz, M. Navarro, S. J. Snipas, M. Drag and G. S. Salvesen, *Cell Death Differ.*, 2019, **26**, 229–244.
27 T. M. Yaron-Barir, B. A. Joughin, E. M. Huntsman, A. Kerelsky, D. M. Cizin, B. M. Cohen, A. Regev, J. Song, N. Vasan, T. Y. Lin, J. M. Orozco, C. Schoenherr, C. Sagum, M. T. Bedford, R. M. Wynn, S. C. Tso, D. T. Chuang, L. Li, S. S. Li, P. Creixell, K. Krismer,

M. Takegami, H. Lee, B. Zhang, J. Lu, I. Cossentino, S. D. Landry, M. Uduman, J. Blenis, O. Elemento, M. C. Frame, P. V. Hornbeck, L. C. Cantley, B. E. Turk, M. B. Yaffe and J. L. Johnson, *Nature*, 2024, **629**, 1174–1181.
28 C. Yang, Q. Wang and W. Ding, *RSC Adv.*, 2019, **9**, 25285–25302.
29 G. Ren, G. Blum, M. Verdoes, H. Liu, S. Syed, L. E. Edgington, O. Gheysens, Z. Miao, H. Jiang, S. S. Gambhir, M. Bogyo and Z. Cheng, *PLoS One*, 2011, **6**, e28029.
30 H. Stark, *Expert Opin. Drug Discovery*, 2020, **15**, 1365–1367.
31 L. O. Ofori, N. P. Withana, T. R. Prestwood, M. Verdoes, J. J. Brady, M. M. Winslow, J. Sorger and M. Bogyo, *ACS Chem. Biol.*, 2015, **10**, 1977–1988.
32 A. Mochida, F. Ogata, T. Nagaya, P. L. Choyke and H. Kobayashi, *Bioorg. Med. Chem.*, 2018, **26**, 925–930.
33 F. Pesapane, K. Downey, A. Rotili, E. Cassano and D. M. Koh, *Insights Imaging*, 2020, **11**, 79.
34 A. P. Amini, J. D. Kirkpatrick, C. S. Wang, A. M. Jaeger, S. Su, S. Naranjo, Q. Zhong, C. M. Cabana, T. Jacks and S. N. Bhatia, *Nat. Commun.*, 2022, **13**, 5745.
35 H. Li, D. Kim, Q. Yao, H. Ge, J. Chung, J. Fan, J. Wang, X. Peng and J. Yoon, *Angew Chem. Int. Ed. Engl.*, 2021, **60**, 17268–17289.
36 N. D. Rawlings, A. J. Barrett, P. D. Thomas, X. Huang, A. Bateman and R. D. Finn, *Nucleic Acids Res.*, 2018, **46**, D624–D632.
37 P. Kasperkiewicz, M. Poreba, K. Groborz and M. Drag, *FEBS J.*, 2017, **284**, 1518–1539.
38 M. Verdoes, K. Oresic Bender, E. Segal, W. A. van der Linden, S. Syed, N. P. Withana, L. E. Sanman and M. Bogyo, *J. Am. Chem. Soc.*, 2013, **135**, 14726–14730.
39 G. Blum, S. R. Mullins, K. Keren, M. Fonovic, C. Jedeszko, M. J. Rice, B. F. Sloane and M. Bogyo, *Nat. Chem. Biol.*, 2005, **1**, 203–209.
40 G. Blum, G. von Degenfeld, M. J. Merchant, H. M. Blau and M. Bogyo, *Nat. Chem. Biol.*, 2007, **3**, 668–677.
41 L. P. Arnett, R. Rana, W. W. Chung, X. Li, M. Abtahi, D. Majonis, J. Bassan, M. Nitz and M. A. Winnik, *Chem. Rev.*, 2023, **123**, 1166–1205.
42 F. F. Faucher, K. J. Liu, E. D. Cosco, J. C. Widen, J. Sorger, M. Guerra and M. Bogyo, *ACS Cent. Sci.*, 2023, **9**, 1059–1069.
43 J. Liu, F. Wu, M. Wang, M. Tao, Z. Liu and Z. Hai, *Anal. Chem.*, 2023, **95**, 9404–9408.
44 Y. Yang, J. Zhang, Z. Li, F. Li, K. Wang, B. Zhang, G. Lyu and M. Yang, *Anal. Chem.*, 2025, **97**, 19349–19359.
45 Y. Feng, C. Xie, T. B. Ren, S. Xu, S. Huang, S. L. Liu, L. Yuan, S. Y. Huan and X. B. Zhang, *Angew Chem. Int. Ed. Engl.*, 2025, **64**, e202512588.
46 J. P. Kahler, J. Coene, M. Skorenski, D. Korovesis and S. H. L. Verhelst, *ACS Chem. Biol.*, 2025, **20**, 2356–2362.
47 T. Gao, C. Xiang, X. Ding and M. Xie, *Heliyon*, 2024, **10**, e38174.
48 Y. Hu, J. Liu, M. Xu and K. Pu, *J. Am. Chem. Soc.*, 2025, **147**, 7148–7157.
49 H. Li, Q. Yao, W. Sun, K. Shao, Y. Lu, J. Chung, D. Kim, J. Fan, S. Long, J. Du, Y. Li, J. Wang, J. Yoon and X. Peng, *J. Am. Chem. Soc.*, 2020, **142**, 6381–6389.
50 J. C. Widen, M. Tholen, J. J. Yim, A. Antaris, K. M. Casey, S. Rogalla, A. Klaassen, J. Sorger and M. Bogyo, *Nat. Biomed. Eng.*, 2021, **5**, 264–277.
51 S. Chen, U. Goncin, J. Zhu, S. P. Su, T. A. Czyzyk, C. O. Miller, R. K. Sadabad and M. Bogyo, *bioRxiv*, 2025, preprint, DOI: **10.1101/2025.05.27.656501**.
52 M. Kazim, A. Ganguly, S. M. Malespini, L. Thang, N. L. Patel, C. Kim, J. D. Kalen, S. Difilippantonio and E. Yoo, *bioRxiv*, 2025, preprint, DOI: **10.1101/2025.03.13.643086**.
53 R. Wei, L. Lei, L. L. Wu, L. Zhang and H. Y. Hu, *ChemBioChem*, 2025, **26**, e202400990.
54 Y. Chen, J. Du, X. Meng, L. L. Wu, Q. Zhang, X. Han, L. Zhang, Q. Wang and H. Y. Hu, *Talanta*, 2024, **278**, 126475.
55 F. V. Suurs, S. Q. Qiu, J. J. Yim, C. P. Schroder, H. Timmer-Bosscha, E. S. Bensen, J. T. Santini Jr, E. G. E. de Vries, M. Bogyo and G. M. van Dam, *EJNMMI Res.*, 2020, **10**, 111.
56 G. T. Kennedy, D. E. Holt, F. S. Azari, E. Bernstein, B. Nadeem, A. Chang, N. T. Sullivan, A. Segil, C. Desphande, E. Bensen, J. T. Santini, J. C. Kucharczuk, E. J. Delikatny, M. Bogyo, A. J. M. Egan, C. W. Bradley, E. Eruslanov, J. D. Lickliter, G. Wright and S. Singhal, *Clin. Cancer Res.*, 2022, **28**, 3729–3741.
57 G. T. Kennedy, F. S. Azari, B. Nadeem, A. Chang, A. Segil, E. Bernstein, C. Desphande, J. C. Kucharczuk, E. J. Delikatny and S. Singhal, *Mol. Imaging*, 2022, **2022**, 5447290.
58 P. Bou-Samra, A. Chang, E. Guo, F. Azari, G. Kennedy, J. T. Santini Jr, E. S. Bensen, D. Jarrar and S. Singhal, *Transl. Lung Cancer Res.*, 2023, **12**, 2370–2380.
59 P. Bou-Samra, G. T. Kennedy, A. Chang, E. Guo, F. S. Azari, A. Din, J. T. Santini Jr, E. S. Bensen and S. Singhal, *Ann. Thorac. Surg.*, 2025, **119**, 625–633.
60 S. Y. Li, L. H. Liu, H. Cheng, B. Li, W. X. Qiu and X. Z. Zhang, *Chem. Commun.*, 2015, **51**, 14520–14523.
61 H. Gerwien, S. Hermann, X. Zhang, E. Korpos, J. Song, K. Kopka, A. Faust, C. Wenning, C. C. Gross, L. Honold, N. Melzer, G. Opdenakker, H. Wiendl, M. Schafers and L. Sorokin, *Sci. Transl. Med.*, 2016, **8**, 364ra152.
62 R. Vanhoutte, M. Barniol-Xicota, W. Chiu, L. Vangeel, D. Jochmans, S. De Jonghe, H. Zidane, H. M. Barr, N. London, J. Neyts and S. H. L. Verhelst, *Chem. Sci.*, 2023, **14**, 1666–1672.
63 O. Marshall, R. McGrory, S. Songsri, A. R. Thomson and A. Sutherland, *Chem. Sci.*, 2025, **16**, 3490–3497.
64 J. Almaliti, M. Alhindy, M. C. Yoon, V. Hook, T. F. Molinski, A. J. O'Donoghue and W. H. Gerwick, *ACS Omega*, 2024, **9**, 3997–4003.
65 G. Geylan, M. Kabeshov, S. Genheden, C. Kannas, T. Kogej, L. De Maria, F. David and O. Engkvist, *Chem. Sci.*, 2025, **16**, 17927–17938.
66 A. B. Berger, K. B. Sexton and M. Bogyo, *Cell Res.*, 2006, **16**, 961–963.

67 G. P. McStay, G. S. Salvesen and D. R. Green, *Cell Death Differ.*, 2008, **15**, 322–331.
68 B. I. Ratnikov, P. Cieplak, K. Gramatikoff, J. Pierce, A. Eroshkin, Y. Igarashi, M. Kazanov, Q. Sun, A. Godzik, A. Osterman, B. Stec, A. Strongin and J. W. Smith, *Proc. Natl. Acad. Sci. U. S. A.*, 2014, **111**, E4148–E4155.
69 M. Poreba and M. Drag, *Curr. Med. Chem.*, 2010, **17**, 3968–3995.
70 M. Drag, M. Bogyo, J. A. Ellman and G. S. Salvesen, *J. Biol. Chem.*, 2010, **285**, 3310–3318.
71 M. Poreba, G. S. Salvesen and M. Drag, *Nat. Protoc.*, 2017, **12**, 2189–2214.
72 E. Zervoudi, A. Papakyriakou, D. Georgiadou, I. Evnouchidou, A. Gajda, M. Poreba, G. S. Salvesen, M. Drag, A. Hattori, L. Swevers, D. Vourloumis and E. Stratikos, *Biochem. J.*, 2011, **435**, 411–420.
73 K. K. Sivaraman, C. A. Oellig, K. Huynh, S. C. Atkinson, M. Poreba, M. A. Perugini, K. R. Trenholme, D. L. Gardiner, G. Salvesen, M. Drag, J. P. Dalton, J. C. Whisstock and S. McGowan, *J. Mol. Biol.*, 2012, **422**, 495–507.
74 M. Poreba, S. McGowan, T. S. Skinner-Adams, K. R. Trenholme, D. L. Gardiner, J. C. Whisstock, J. To, G. S. Salvesen, J. P. Dalton and M. Drag, *PLoS One*, 2012, **7**, e31938.
75 M. Poreba, A. Gajda, J. Picha, J. Jiracek, A. Marschner, C. D. Klein, G. S. Salvesen and M. Drag, *Biochimie*, 2012, **94**, 704–710.
76 F. Veillard, B. Potempa, M. Poreba, M. Drag and J. Potempa, *Biol. Chem.*, 2012, **393**, 1471–1476.
77 E. Weglarz-Tomczak, M. Poreba, A. Byzia, L. Berlicki, B. Nocek, R. Mulligan, A. Joachimiak, M. Drag and A. Mucha, *Biochimie*, 2013, **95**, 419–428.
78 R. K. Carroll, F. Veillard, D. T. Gagne, J. M. Lindenmuth, M. Poreba, M. Drag, J. Potempa and L. N. Shaw, *Biol. Chem.*, 2013, **394**, 791–803.
79 M. Poreba, M. Mihelic, P. Krai, J. Rajkovic, A. Krezel, M. Pawelczak, M. Klemba, D. Turk, B. Turk, R. Latajka and M. Drag, *Amino Acids*, 2014, **46**, 931–943.
80 L. E. de Vries, M. I. Sanchez, K. Groborz, L. Kuppens, M. Poreba, C. Lehmann, N. Nevins, C. Withers-Martinez, D. J. Hirst, F. Yuan, S. Arastu-Kapur, M. Horn, M. Mares, M. Bogyo, M. Drag and E. Deu, *FEBS J.*, 2019, **286**, 3998–4023.
81 M. Gersch, M. Stahl, M. Poreba, M. Dahmen, A. Dziedzic, M. Drag and S. A. Sieber, *ACS Chem. Biol.*, 2016, **11**, 389–399.
82 Y. Choe, F. Leonetti, D. C. Greenbaum, F. Lecaille, M. Bogyo, D. Bromme, J. A. Ellman and C. S. Craik, *J. Biol. Chem.*, 2006, **281**, 12824–12832.
83 N. A. Thornberry, T. A. Rano, E. P. Peterson, D. M. Rasper, T. Timkey, M. Garcia-Calvo, V. M. Houtzager, P. A. Nordstrom, S. Roy, J. P. Vaillancourt, K. T. Chapman and D. W. Nicholson, *J. Biol. Chem.*, 1997, **272**, 17907–17911.
84 M. Poreba, W. Rut, M. Vizovisek, K. Groborz, P. Kasperkiewicz, D. Finlay, K. Vuori, D. Turk, B. Turk, G. S. Salvesen and M. Drag, *Chem. Sci.*, 2018, **9**, 2113–2129.
85 M. Poreba, K. Groborz, M. Vizovisek, M. Maruggi, D. Turk, B. Turk, G. Powis, M. Drag and G. S. Salvesen, *Chem. Sci.*, 2019, **10**, 8461–8477.
86 P. Kasperkiewicz, M. Poreba, S. J. Snipas, H. Parker, C. C. Winterbourn, G. S. Salvesen and M. Drag, *Proc. Natl. Acad. Sci. U. S. A.*, 2014, **111**, 2518–2523.
87 P. Kasperkiewicz, Y. Altman, M. D'Angelo, G. S. Salvesen and M. Drag, *J. Am. Chem. Soc.*, 2017, **139**, 10115–10125.
88 W. Rut, K. Groborz, L. Zhang, X. Sun, M. Zmudzinski, B. Pawlik, X. Wang, D. Jochmans, J. Neyts, W. Mlynarski, R. Hilgenfeld and M. Drag, *Nat. Chem. Biol.*, 2021, **17**, 222–228.
89 W. Rut, M. Poreba, P. Kasperkiewicz, S. J. Snipas and M. Drag, *J. Med. Chem.*, 2018, **61**, 5222–5234.
90 N. Horbach, M. Kalinka, N. Cwilichowska-Puslecka, A. Al Mamun, A. Mikolajczyk-Martinez, B. Turk, S. J. Snipas, P. Kasperkiewicz, K. M. Groborz and M. Poreba, *Cell Chem. Biol.*, 2025, **32**, 603.
91 T. Janiszewski, S. Kolt, I. Ciaston, M. Vizovisek, M. Poreba, B. Turk, M. Drag, J. Koziel and P. Kasperkiewicz, *Cell Chem. Biol.*, 2023, **30**, 159.
92 U. Fischer and K. Schulze-Osthoff, *Cell Death Differ.*, 2005, **12**, 942–961.
93 J. C. Reed, *Nat. Rev. Drug Discovery*, 2002, **1**, 111–121.
94 K. M. Groborz, M. Kalinka, J. Grzymska, S. Kolt, S. J. Snipas and M. Poreba, *Chem. Sci.*, 2023, **14**, 2289–2302.
95 N. Van Opdenbosch and M. Lamkanfi, *Immunity*, 2019, **50**, 1352–1364.
96 K. Groborz, M. Truong, I. Stowe, B. Lee, R. Jones, E. Plise, E. Levy, P. Kou, W. Lee, J. Zhang, J. Nguyen, M. Kalinka, M. Drag, N. Kayagaki, K. Newton, M. Poreba and V. Dixit, *bioRxiv*, 2025, preprint, DOI: **10.1101/2025.02.11.637513**.
97 A. Korba-Mikolajczyk, K. D. Sluzalska and P. Kasperkiewicz, *Cell Death Dis.*, 2025, **16**, 535.
98 C. T. Pham, *Nat. Rev. Immunol.*, 2006, **6**, 541–550.
99 E. S. Radisky, *J. Biol. Chem.*, 2024, **300**, 107347.
100 W. Rut, K. Groborz, L. Zhang, S. Modrzycka, M. Poreba, R. Hilgenfeld and M. Drag, *Antiviral Res.*, 2020, **175**, 104731.
101 H. Shi, R. T. Kwok, J. Liu, B. Xing, B. Z. Tang and B. Liu, *J. Am. Chem. Soc.*, 2012, **134**, 17972–17981.
102 H. Cen, F. Mao, I. Aronchik, R. J. Fuentes and G. L. Firestone, *FASEB J.*, 2008, **22**, 2243–2252.
103 M. Minoshima, T. Matsumoto and K. Kikuchi, *Anal. Chem.*, 2014, **86**, 7925–7930.
104 M. Dai, Y. J. Yang, S. Sarkar and K. H. Ahn, *Chem. Soc. Rev.*, 2023, **52**, 6344–6358.
105 Y. Wang, Y. Bian, X. Chen and D. Su, *Chem.–Asian J.*, 2022, **17**, e202200018.
106 J. S. Sidhu, G. Kaur, A. R. Chavan, M. K. Chahal and R. Taliyan, *Analyst*, 2024, **149**, 5739–5761.
107 B. Wang, Z. Chen, X. Cen, Y. Liang, L. Tan, E. Liang, L. Zheng, Y. Zheng, Z. Zhan and K. Cheng, *Chem. Sci.*, 2022, **13**, 2324–2330.
108 R. Sun, X. Wu, Y. Mao, H. Wang, C. Bian, P. Lv, Z. Zhao, X. Li, W. Fu, J. Lu and Z. Cao, *Luminescence*, 2022, **37**, 1335–1342.

109 X. Shi, Y. Deng, X. Liu, G. Gao, R. Wang and G. Liang, *Biosens. Bioelectron.*, 2022, **208**, 114212.
110 Z. Zhang, R. Sun, C. Bian, H. Wang, Z. Zhao, P. Lv, J. Lu, H. Zhang, H. Zeng, Y. Chen and Z. Cao, *Chin. Chem. Lett.*, 2025, **36**, 109784.
111 J. Huang, P. Cheng, C. Xu, S. S. Liew, S. He, Y. Zhang and K. Pu, *Angew Chem. Int. Ed. Engl.*, 2022, **61**, e202203235.
112 R. Tannous, C. Zhang and D. Shabat, *Bioconjug. Chem.*, 2025, **36**, 1113–1120.
113 S. Xia, E. Liang, L. Xu, L. Tan, X. Guo and K. Cheng, *Anal. Chem.*, 2024, **96**, 19641–19650.
114 P. Saraon, S. Pathmanathan, J. Snider, A. Lyakisheva, V. Wong and I. Stagljar, *Oncogene*, 2021, **40**, 4079–4093.
115 A. Fassl, Y. Geng and P. Sicinski, *Science*, 2022, **375**, eabc1495.
116 S. M. Usama, B. Zhao and K. Burgess, *Chem. Soc. Rev.*, 2021, **50**, 9794–9816.
117 R. Ciriminna, G. Angellotti, G. L. Petri and M. Pagliaro, *Heliyon*, 2024, **10**, e33658.
118 J. T. Hou, K. P. Ko, H. Shi, W. X. Ren, P. Verwilst, S. Koo, J. Y. Lee, S. G. Chi and J. S. Kim, *ACS Sens.*, 2017, **2**, 1512–1516.
119 S. Guo, J. Fan, B. Wang, M. Xiao, Y. Li, J. Du and X. Peng, *ACS Appl. Mater. Interfaces*, 2018, **10**, 1499–1507.
120 S. I. Reja, M. Minoshima, Y. Hori and K. Kikuchi, *Chem. Sci.*, 2020, **12**, 3437–3447.
121 J. Huang and K. Pu, *Chem. Sci.*, 2020, **12**, 3379–3392.
122 Z. Zhang, K. G. Neiva, M. W. Lingen, L. M. Ellis and J. E. Nor, *Cell Death Differ.*, 2010, **17**, 499–512.
123 S. H. Lee, D. Jeong, Y. S. Han and M. J. Baek, *Ann. Surg. Treat. Res.*, 2015, **89**, 1–8.
124 Y. Jiao, J. Yin, H. He, X. Peng, Q. Gao and C. Duan, *J. Am. Chem. Soc.*, 2018, **140**, 5882–5885.
125 H. Masuda, D. Zhang, C. Bartholomeusz, H. Doihara, G. N. Hortobagyi and N. T. Ueno, *Breast Cancer Res. Treat.*, 2012, **136**, 331–345.
126 N. Iqbal and N. Iqbal, *Mol. Biol. Int.*, 2014, **2014**, 852748.
127 S. M. Swain, M. Shastry and E. Hamilton, *Nat. Rev. Drug Discovery*, 2023, **22**, 101–126.
128 S. Liu, W. Song, X. Gao, Y. Su, E. Gao and Q. Gao, *Anal. Chem.*, 2019, **91**, 1507–1515.
129 C. Li, Q. Lin, F. Hu, R. Bao, H. Cai and Y. Gu, *Biosens. Bioelectron.*, 2022, **214**, 114503.
130 D. Xie, Y. Li, J. Shi, Y. P. Zhu, Y. Wang, C. J. Butch and Z. Wang, *J. Nanobiotechnol.*, 2023, **21**, 342.
131 H. Deng, Q. Lei, W. Shang, Y. Li, L. Bi, N. Yang, Z. Yu and W. Li, *Eur. J. Med. Chem.*, 2022, **230**, 114100.
132 H. Deng, Q. Lei, C. Wang, Z. Wang, H. Chen, G. Wang, N. Yang, D. Huang, Q. Yu, M. Yao, X. Xiao, G. Zhu, C. Cheng, Y. Li, F. Li, P. Tian and W. Li, *Nat. Commun.*, 2022, **13**, 6944.
133 H. Deng, Q. Lei, N. Yang, S. Dai, H. Peng, K. Yang, Z. Xiao, D. Wang, Z. Yu, N. Li and W. Li, *Anal. Chem.*, 2022, **94**, 10118–10126.
134 Q. Lei, X. Zhou, Y. Li, S. Zhao, N. Yang, Z. Xiao, C. Song, Q. Yu and H. Deng, *J. Am. Chem. Soc.*, 2025, **147**, 4552–4570.
135 X. Zhou, Q. Lei, Z. Xiao, C. Song and H. Deng, *Anal. Chem.*, 2024, **96**, 3525–3534.
136 R. Sicard, J. Dhuguru, W. Liu, N. Patel, R. Landgraf and J. N. Wilson, *Bioorg. Med. Chem. Lett.*, 2012, **22**, 5532–5535.
137 H. Lee, W. Liu, A. S. Brown, R. Landgraf and J. N. Wilson, *Anal. Chem.*, 2016, **88**, 11310–11313.
138 H. Lee, R. Landgraf and J. N. Wilson, *Bioorg. Med. Chem.*, 2017, **25**, 6016–6023.
139 C. L. Fleming, P. A. Sandoz, T. Inghardt, B. Onfelt, M. Grotli and J. Andreasson, *Angew Chem. Int. Ed. Engl.*, 2019, **58**, 15000–15004.
140 C. L. Fleming, C. Benitez-Martin, E. Bernson, Y. Xu, L. Kristenson, T. Inghardt, T. Lundback, F. B. Thoren, M. Grotli and J. Andreasson, *Chem. Sci.*, 2024, **15**, 6897–6905.
141 D. Korovesis, C. Merillat, R. Derua and S. H. L. Verhelst, *Commun. Chem.*, 2025, **8**, 34.
142 U. M. Glocker, F. Braun, H. C. Eberl and M. Bantscheff, *Mol. Cell. Proteomics*, 2025, **24**, 100963.
143 R. Serafim, L. Haarer, J. Pedreira and M. Gehringer, *Curr. Res. Chem. Biol.*, 2023, **3**, 100040.
144 Z. Zhao and P. E. Bourne, *Med. Res. Rev.*, 2025, **45**, 629–653.
145 Y. Sun, M. Ding, X. Zeng, Y. Xiao, H. Wu, H. Zhou, B. Ding, C. Qu, W. Hou, A. Er-Bu, Y. Zhang, Z. Cheng and X. Hong, *Chem. Sci.*, 2017, **8**, 3489–3493.
146 A. Ji, H. Lou, J. Li, Y. Hao, X. Wei, Y. Wu, W. Zhao, H. Chen and Z. Cheng, *Chem. Sci.*, 2024, **15**, 3339–3348.
147 A. Aljoundi, I. Bjij, A. El Rashedy and M. E. S. Soliman, *Protein J.*, 2020, **39**, 97–105.
148 A. Abdeldayem, Y. S. Raouf, S. N. Constantinescu, R. Moriggl and P. T. Gunning, *Chem. Soc. Rev.*, 2020, **49**, 2617–2687.
149 Faridoon, R. Ng, G. Zhang and J. J. Li, *Med. Chem. Res.*, 2023, **32**, 1039–1062.
150 J. M. Bradshaw, J. M. McFarland, V. O. Paavilainen, A. Bisconte, D. Tam, V. T. Phan, S. Romanov, D. Finkle, J. Shu, V. Patel, T. Ton, X. Li, D. G. Loughhead, P. A. Nunn, D. E. Karr, M. E. Gerritsen, J. O. Funk, T. D. Owens, E. Verner, K. A. Brameld, R. J. Hill, D. M. Goldstein and J. Taunton, *Nat. Chem. Biol.*, 2015, **11**, 525–531.
151 M. Müller, V. Shalgunov, L. Hvass, J. T. Jorgensen, V. Kramer, M. Staudt, U. M. Battisti, A. Kjaer and M. M. Herth, *Bioorg. Med. Chem. Lett.*, 2023, **80**, 129088.
152 J. Zhang, N. P. McAndrew, X. Wang, Y. Du, B. DiCarlo, M. Wang, K. Chen, W. Yu and X. Hu, *Breast Cancer Res.*, 2023, **25**, 81.
153 Y. Yu, K. Huang, Y. Lin, J. Zhang and C. Song, *Cancer Med.*, 2023, **12**, 15090–15100.
154 K. Oguchi, H. Araki, S. Tsuji, M. Nakamura, A. Miura, K. Funabashi, A. Osada, S. Tanaka, T. Suzuki, S. S. Kobayashi and S. Mizuarai, *Cancer Sci.*, 2023, **114**, 654–664.
155 S. Lee, J. Kim, J. Jo, J. W. Chang, J. Sim and H. Yun, *Eur. J. Med. Chem.*, 2021, **216**, 113318.
156 B. Biswas, Y. H. Huang, D. J. Craik and C. K. Wang, *Chem. Sci.*, 2024, **15**, 13130–13147.

157 L. Wu, Z. Armstrong, S. P. Schroder, C. de Boer, M. Artola, J. M. Aerts, H. S. Overkleeft and G. J. Davies, *Curr. Opin. Chem. Biol.*, 2019, **53**, 25–36.
158 K. Fujita, M. Kamiya, T. Yoshioka, A. Ogasawara, R. Hino, R. Kojima, H. Ueo and Y. Urano, *ACS Cent. Sci.*, 2020, **6**, 2217–2227.
159 L. Dong, M. Y. Zhang, H. H. Han, Y. Zang, G. R. Chen, J. Li, X. P. He and S. Vidal, *Chem. Sci.*, 2021, **13**, 247–256.
160 L. Xu, H. Chu, D. Gao, Q. Wu, Y. Sun, Z. Wang, P. Ma and D. Song, *Anal. Chem.*, 2023, **95**, 2949–2957.
161 S. M. Stanford and N. Bottini, *Nat. Rev. Drug Discovery*, 2023, **22**, 273–294.
162 R. J. He, Z. H. Yu, R. Y. Zhang and Z. Y. Zhang, *Acta Pharmacol. Sin.*, 2014, **35**, 1227–1246.
163 J. Pan, L. Zhou, C. Zhang, Q. Xu and Y. Sun, *Signal Transduction Targeted Ther.*, 2022, **7**, 177.
164 D. Liang, C. Yu, Y. Lan, C. Guo, Y. Zhang, S. Chen, L. Du, A. Liu, D. Sun, M. Li and W. Zhao, *Anal. Chem.*, 2025, **97**, 12143–12154.
165 J. Hu, L. Jiang, L. Li and W. H. Chen, *Eur. J. Med. Chem.*, 2025, **300**, 118158.
166 P. Cheng and K. Pu, *Chem. Soc. Rev.*, 2024, **53**, 10171–10188.
167 M. Yuan, Y. Wu, C. Zhao, Z. Chen, L. Su, H. Yang and J. Song, *Theranostics*, 2022, **12**, 1459–1485.
168 V. Bernard-Gauthier, J. J. Bailey, S. Berke and R. Schirrmacher, *Molecules*, 2015, **20**, 22000–22027.
169 M. K. Narayanam, J. E. Tsang, S. Xu, D. A. Nathanson and J. M. Murphy, *Chem. Sci.*, 2023, **14**, 13825–13831.
170 M. T. Kendirli, R. Malek, M. B. Silveira, C. Acosta, S. Zhang, C. Azevedo, S. C. Nagy, F. Habte, M. L. James, L. D. Recht and C. Beinat, *Nucl. Med. Biol.*, 2023, **124–125**, 108382.
171 S. R. Gundam, A. Bansal, M. Kethamreddy, S. Ghatamaneni, V. J. Lowe, M. E. Murray and M. K. Pandey, *Sci. Rep.*, 2024, **14**, 15960.
172 Z. Chen, J. Chen, W. Mori, Y. Yi, J. Rong, Y. Li, E. R. C. Leon, T. Shao, Z. Song, T. Yamasaki, H. Ishii, Y. Zhang, T. Kokufuta, K. Hu, L. Xie, L. Josephson, R. Van, Y. Shao, S. Factor, M. R. Zhang and S. H. Liang, *J. Med. Chem.*, 2024, **67**, 2559–2569.
173 C. Beinat, C. B. Patel, T. Haywood, S. Murty, L. Naya, J. B. Castillo, S. T. Reyes, M. Phillips, P. Buccino, B. Shen, J. H. Park, M. E. I. Koran, I. S. Alam, M. L. James, D. Holley, K. Halbert, H. Gandhi, J. Q. He, M. Granucci, E. Johnson, D. D. Liu, N. Uchida, R. Sinha, P. Chu, D. E. Born, G. I. Warnock, I. Weissman, M. Hayden-Gephart, M. Khalighi, T. F. Massoud, A. Iagaru, G. Davidzon, R. Thomas, S. Nagpal, L. D. Recht and S. S. Gambhir, *Clin. Cancer Res.*, 2021, **27**, 6467–6478.
174 N. Zhao, C. Bardine, A. L. Lourenco, Y. H. Wang, Y. Huang, S. J. Cleary, D. M. Wilson, D. Y. Oh, L. Fong, M. R. Looney, M. J. Evans and C. S. Craik, *ACS Cent. Sci.*, 2021, **7**, 1638–1649.
175 A. Pandey, S. Chopra, S. J. Cleary, M. Lopez-Alvarez, F. M. Quimby, A. A. A. Alanizi, S. Sakhamuri, N. Zhang, M. R. Looney, C. S. Craik, D. M. Wilson and M. J. Evans, *ACS Infect. Dis.*, 2024, **10**, 2108–2117.
176 A. Iyer, A. A. J. Hamers and A. B. Pillai, *Front. Immunol.*, 2022, **13**, 815828.
177 M. Roederer, *Cytometry A*, 2015, **87**, 689–691.
178 S. P. Perfetto, P. K. Chattopadhyay and M. Roederer, *Nat. Rev. Immunol.*, 2004, **4**, 648–655.
179 D. R. Bandura, V. I. Baranov, O. I. Ornatsky, A. Antonov, R. Kinach, X. Lou, S. Pavlov, S. Vorobiev, J. E. Dick and S. D. Tanner, *Anal. Chem.*, 2009, **81**, 6813–6822.
180 M. H. Spitzer and G. P. Nolan, *Cell*, 2016, **165**, 780–791.
181 R. Finck, E. F. Simonds, A. Jager, S. Krishnaswamy, K. Sachs, W. Fantl, D. Pe'er, G. P. Nolan and S. C. Bendall, *Cytometry A*, 2013, **83**, 483–494.
182 L. Lai, R. Ong, J. Li and S. Albani, *Cytometry A*, 2015, **87**, 369–374.
183 L. R. Olsen, M. D. Leipold, C. B. Pedersen and H. T. Maecker, *Cytometry A*, 2019, **95**, 156–172.
184 C. Giesen, H. A. Wang, D. Schapiro, N. Zivanovic, A. Jacobs, B. Hattendorf, P. J. Schuffler, D. Grolimund, J. M. Buhmann, S. Brandt, Z. Varga, P. J. Wild, D. Gunther and B. Bodenmiller, *Nat. Methods*, 2014, **11**, 417–422.
185 Q. Chang, O. I. Ornatsky, I. Siddiqui, A. Loboda, V. I. Baranov and D. W. Hedley, *Cytometry A*, 2017, **91**, 160–169.
186 Q. Chang, O. I. Ornatsky, I. Siddiqui, R. Straus, V. I. Baranov and D. W. Hedley, *Sci. Rep.*, 2016, **6**, 36641.
187 D. Moldoveanu, L. Ramsay, M. Lajoie, L. Anderson-Trocme, M. Lingrand, D. Berry, L. J. M. Perus, Y. Wei, C. Moraes, R. Alkallas, S. Rajkumar, D. Zuo, M. Dankner, E. H. Xu, N. R. Bertos, H. S. Najafabadi, S. Gravel, S. Costantino, M. J. Richer, A. W. Lund, S. V. Del Rincon, A. Spatz, W. H. Miller Jr, R. Jamal, R. Lapointe, A. M. Mes-Masson, S. Turcotte, K. Petrecca, S. Dumitra, A. N. Meguerditchian, K. Richardson, F. Tremblay, B. Wang, M. Chergui, M. C. Guiot, K. Watters, J. Stagg, D. F. Quail, C. Mihalcioiu, S. Meterissian and I. R. Watson, *Sci. Immunol.*, 2022, **7**, eabi5072.
188 E. Y. Su, K. Fread, S. Goggin, E. R. Zunder and P. Cahan, *Sci. Data*, 2024, **11**, 559.
189 L. J. Edgar, R. N. Vellanki, T. D. McKee, D. Hedley, B. G. Wouters and M. Nitz, *Angew Chem. Int. Ed. Engl.*, 2016, **55**, 13159–13163.
190 M. A. Lumba, L. M. Willis, S. Santra, R. Rana, L. Schito, S. Rey, B. G. Wouters and M. Nitz, *Org. Biomol. Chem.*, 2017, **15**, 6388–6392.
191 J. Bassan, L. M. Willis, R. N. Vellanki, A. Nguyen, L. J. Edgar, B. G. Wouters and M. Nitz, *Proc. Natl. Acad. Sci. U. S. A.*, 2019, **116**, 8155–8160.
192 F. Gärtner, U. Knippschild and T. Burster, *ACS Omega*, 2020, **5**, 28233–28238.
193 R. Hou, Y. Gu, Y. Zhao, X. Zhao, L. Yang, X. Yan and Q. Wang, *At. Spectrosc.*, 2024, **45**, 74–82.
194 J. Chen, X. Wang, F. He and Z. Pan, *Bioconjug. Chem.*, 2018, **29**, 1640–1645.
195 P. J. Endres, K. W. Macrenaris, S. Vogt, M. J. Allen and T. J. Meade, *Mol. Imaging*, 2006, **5**, 485–497.

196 J. Mu, J. Lin, P. Huang and X. Chen, *Chem. Soc. Rev.*, 2018, **47**, 5554–5573.
197 A. Sharma, P. Verwilst, M. Li, D. Ma, N. Singh, J. Yoo, Y. Kim, Y. Yang, J. H. Zhu, H. Huang, X. L. Hu, X. P. He, L. Zeng, T. D. James, X. Peng, J. L. Sessler and J. S. Kim, *Chem. Rev.*, 2024, **124**, 2699–2804.
198 H. H. Chen, H. Yuan, L. Josephson and D. E. Sosnovik, *Theranostics*, 2012, **2**, 148–155.
199 L. Qiu, W. Wang, K. Li, Y. Peng, G. Lv, Q. Liu, F. Gao, Y. Seimbille, M. Xie and J. Lin, *Theranostics*, 2019, **9**, 6962–6975.
200 K. Wang, F. Zhang, Y. Wei, W. Wei, L. Jiang, Z. Liu and S. Liu, *Anal. Chem.*, 2021, **93**, 7870–7878.
201 S.-Y. Li, L.-H. Liu, L. Rong, W.-X. Qiu, H.-Z. Jia, B. Li, F. Li and X.-Z. Zhang, *Adv. Funct. Mater.*, 2015, **25**, 7317–7326.
202 S. W. Chung, J. U. Choi, Y. S. Cho, H. R. Kim, T. H. Won, P. Dimitrion, O. C. Jeon, S. W. Kim, I. S. Kim, S. Y. Kim and Y. Byun, *Adv. Sci.*, 2018, **5**, 1800368.
203 L. Li, F. Jia, Y. Li and Y. Peng, *RSC Adv.*, 2024, **14**, 3010–3023.
204 D. Asanuma, M. Sakabe, M. Kamiya, K. Yamamoto, J. Hiratake, M. Ogawa, N. Kosaka, P. L. Choyke, T. Nagano, H. Kobayashi and Y. Urano, *Nat. Commun.*, 2015, **6**, 6463.
205 A. Sharma, E. J. Kim, H. Shi, J. Y. Lee, B. G. Chung and J. S. Kim, *Biomaterials*, 2018, **155**, 145–151.
206 O. Mijanovic, A. Brankovic, A. N. Panin, S. Savchuk, P. Timashev, I. Ulasov and M. S. Lesniak, *Cancer Lett.*, 2019, **449**, 207–214.
207 X. Jin, J. Zhang, X. Jin, L. Liu and X. Tian, *ACS Med. Chem. Lett.*, 2020, **11**, 1514–1520.
208 L. Zhou, F. He, X. Xiang, C. Dong, T. Xiang, X. Li, H. Li, L. Bu, Y. Wang and X. Ma, *Mol. Pharm.*, 2023, **20**, 3539–3548.
209 S. Niland, A. X. Riscanevo and J. A. Eble, *Int. J. Mol. Sci.*, 2021, **23**, 146.
210 B. Turk, *Nat. Rev. Drug Discovery*, 2006, **5**, 785–799.
211 M. Drag and G. S. Salvesen, *Nat. Rev. Drug Discovery*, 2010, **9**, 690–701.
212 L. K. B. Tam, J. C. H. Chu, L. He, C. Yang, K. C. Han, P. C. K. Cheung, D. K. P. Ng and P. C. Lo, *J. Am. Chem. Soc.*, 2023, **145**, 7361–7375.
213 A. A. Fitzgerald and L. M. Weiner, *Cancer Metastasis Rev.*, 2020, **39**, 783–803.
214 Y. Mori, K. Dendl, J. Cardinale, C. Kratochwil, F. L. Giesel and U. Haberkorn, *Radiology*, 2023, **306**, e220749.
215 Y. Mori, E. Novruzov, D. Schmitt, J. Cardinale, T. Watabe, P. L. Choyke, A. Alavi, U. Haberkorn and F. L. Giesel, *npj Imaging*, 2024, **2**, 48.
216 C. Lai, R. Cao, R. Li, C. He, X. Wang, H. Shi, C. Qu, K. Qian, S. Song, W. H. Chen and Z. Cheng, *Mol. Pharm.*, 2023, **20**, 4120–4128.
217 L. Feng, W. Hu, X. Zeng, Z. Wei, Y. Long, M. Li, S. Sun, Z. Guo, X. Lan, X. Zhang, R. Zhuang and D. Jiang, *Mol. Pharm.*, 2024, **21**, 4386–4394.
218 L. Meng, R. Lin, J. Zhang, H. Li, D. Xia, Z. Zhao, R. Zhuang, L. Huang, X. Zhang, J. Fang, W. Miao and Z. Guo, *J. Med. Chem.*, 2025, **68**, 6576–6587.
219 J. Xie, F. El Rami, K. Zhou, F. Simonetta, Z. Chen, X. Zheng, M. Chen, P. B. Balakrishnan, S. Y. Dai, S. Murty, I. S. Alam, J. Baker, R. S. Negrin, S. S. Gambhir and J. Rao, *ACS Cent. Sci.*, 2022, **8**, 590–602.
220 W. A. Boivin, D. M. Cooper, P. R. Hiebert and D. J. Granville, *Lab. Invest.*, 2009, **89**, 1195–1220.
221 D. Chowdhury and J. Lieberman, *Annu. Rev. Immunol.*, 2008, **26**, 389–420.
222 M. Poreba, *FEBS J.*, 2020, **287**, 1936–1969.
223 K. Y. Choi, M. Swierczewska, S. Lee and X. Chen, *Theranostics*, 2012, **2**, 156–178.
224 X. Pang, X. He, Z. Qiu, H. Zhang, R. Xie, Z. Liu, Y. Gu, N. Zhao, Q. Xiang and Y. Cui, *Signal Transduct. Targeted Ther.*, 2023, **8**, 1.
225 R. A. Davis, T. Ganguly, R. Harris, S. H. Hausner, L. Kovacs and J. L. Sutcliffe, *J. Med. Chem.*, 2023, **66**, 9842–9852.
226 S. B. Lu, L. Wei, W. He, Z. Y. Bi, Y. Qian, J. Wang, H. Lei and K. Li, *ChemistryOpen*, 2022, **11**, e202200137.
227 J. Abramson, J. Adler, J. Dunger, R. Evans, T. Green, A. Pritzel, O. Ronneberger, L. Willmore, A. J. Ballard, J. Bambrick, S. W. Bodenstein, D. A. Evans, C. C. Hung, M. O'Neill, D. Reiman, K. Tunyasuvunakool, Z. Wu, A. Zemgulyte, E. Arvaniti, C. Beattie, O. Bertolli, A. Bridgland, A. Cherepanov, M. Congreve, A. I. Cowen-Rivers, A. Cowie, M. Figurnov, F. B. Fuchs, H. Gladman, R. Jain, Y. A. Khan, C. M. R. Low, K. Perlin, A. Potapenko, P. Savy, S. Singh, A. Stecula, A. Thillaisundaram, C. Tong, S. Yakneen, E. D. Zhong, M. Zielinski, A. Zidek, V. Bapst, P. Kohli, M. Jaderberg, D. Hassabis and J. M. Jumper, *Nature*, 2024, **630**, 493–500.
228 M. Baek, F. DiMaio, I. Anishchenko, J. Dauparas, S. Ovchinnikov, G. R. Lee, J. Wang, Q. Cong, L. N. Kinch, R. D. Schaeffer, C. Millan, H. Park, C. Adams, C. R. Glassman, A. DeGiovanni, J. H. Pereira, A. V. Rodrigues, A. A. van Dijk, A. C. Ebrecht, D. J. Opperman, T. Sagmeister, C. Buhlheller, T. Pavkov-Keller, M. K. Rathinaswamy, U. Dalwadi, C. K. Yip, J. E. Burke, K. C. Garcia, N. V. Grishin, P. D. Adams, R. J. Read and D. Baker, *Science*, 2021, **373**, 871–876.
229 G. Zhou, D. V. Rusnac, H. Park, D. Canzani, H. M. Nguyen, L. Stewart, M. F. Bush, P. T. Nguyen, H. Wulff, V. Yarov-Yarovoy, N. Zheng and F. DiMaio, *Nat. Commun.*, 2024, **15**, 7761.
230 F. Ren, X. Ding, M. Zheng, M. Korzinkin, X. Cai, W. Zhu, A. Mantsyzov, A. Aliper, V. Aladinskiy, Z. Cao, S. Kong, X. Long, B. H. Man Liu, Y. Liu, V. Naumov, A. Shneyderman, I. V. Ozerov, J. Wang, F. W. Pun, D. A. Polykovskiy, C. Sun, M. Levitt, A. Aspuru-Guzik and A. Zhavoronkov, *Chem. Sci.*, 2023, **14**, 1443–1452.
231 R. P. Joshi, K. J. Schultz, J. W. Wilson, A. Kruel, R. A. Varikoti, C. J. Kombala, D. W. Kneller, S. Galanie, G. Phillips, Q. Zhang, L. Coates, J. Parvathareddy, S. Surendranathan, Y. Kong, A. Clyde, A. Ramanathan, C. B. Jonsson, K. R. Brandvold, M. Zhou, M. S. Head,

A. Kovalevsky and N. Kumar, *J. Chem. Inf. Model.*, 2023, **63**, 1438–1453.
232 L. Elend, L. Jacobsen, T. Cofala, J. Prellberg, T. Teusch, O. Kramer and I. A. Solov'yov, *Molecules*, 2022, **27**, 4020.
233 F. F. Xiang, H. Zhang, Y. L. Wu, Y. J. Chen, Y. Z. Liu, S. Y. Chen, Y. Z. Guo, X. Q. Yu and K. Li, *Adv. Mater.*, 2024, **36**, e2404828.
234 S. Kumar, R. Bhowmik, J. M. Oh, M. A. Abdelgawad, M. M. Ghoneim, R. H. Al-Serwi, H. Kim and B. Mathew, *Sci. Rep.*, 2024, **14**, 4868.
235 S. H. P. de Oliveira, A. Pedawi, V. Kenyon and H. van den Bedem, *J. Med. Chem.*, 2024, **67**, 19417–19427.
236 J. Guo and P. Schwaller, *Chem. Sci.*, 2025, **16**, 6943–6956.